UNIVERSITY OF CALIFORNIA, SAN DIEGO

Applications of Satellite Altimetry to Global Studies of Mid-Ocean Ridges and Continental Margins

A dissertation submitted in partial satisfaction of the requirements for the degree of Doctor of Philosophy in Earth Sciences

by

Christopher S. Small

Committee in charge:

Professor David T. Sandwell, Chair
Professor Peter Lonsdale
Professor Robert L. Parker
Professor Jason Phipps Morgan
Professor Martin J. S. Rudwick

1993

The dissertation of Christopher S. Small is approved, and it is acceptable in quality and form for publication on microfilm:

Jason Phipps Morgan

Robert C. Reeder

M J S Rudnick

Peter Lansdale

David T. Sandwell

Chair

University of California, San Diego

1993

To my family

Table of Contents

List of Figures and Tables

Chapter 2

Chapter 3

Chapter 4

Chapter 5

Chapter 6

Acknowledgements

David Sandwell convinced me that a career in academic science would be more fun than a high paying job in the oil industry. David's contagious enthusiasm for marine geophysics steered me away from a lifetime of seismic data processing and interpretation. It was this same enthusiasm and his extremely pleasant demeanor which led me to Scripps to continue my education in science. David's *Laissez Faire* style of supervision encouraged me to work independently and assume the responsibilities of a real scientist early on in the game. At the same time, his generous funding provided full financial support for my thesis research and allowed me to attend the tribal gatherings at which geophysicists display some of their most interesting behaviour. These gatherings are an education in themselves. Most importantly, David's friendship made graduate school a much more pleasant experience than it would have been otherwise.

Peter Lonsdale forced me to face the geological reality that the workings of the Earth are far too complex to be dissected soley with the blunt instruments provided by geophysical modeling. His support, encouragement and above all, criticisms were most appreciated. His insights and advice regarding the workings of the seagoing research business were priceless.

Bob Parker was probably the best science teacher I ever had; he was certainly the most interesting. The insights he provided into some rather subtle concepts changed the way I will think for the rest of my life. His generous advice and seemingly infinite patience were invaluable.

I thank Jason Phipps Morgan, John Chen, Dan McKenzie and Herb Wang for opening my eyes to the power of skillful application of physics to earth science. Clark Wilson and Clarence Clay taught me the basics of data analysis upon which all science, and especially geophysics, relies.

Bill Boicourt, Larry Sanford and the physical oceanography gang at the University of Maryland showed me the fun side of serious science and convinced me to pursue a career in seagoing research. They will never know how close they came to making a *real* oceanographer out of me.

Throughout my graduate career there have been a number of people who have tried their best to make sure that I didn't work too hard or take things too seriously. Their contribution to my psychological well being cannot be overstated. While there are too many to mention by name, one deserves particular acknowledgement. Catherine Johnson's support, encouragement, reassurance, patience, advice and above all, friendship are deeply appreciated. If not for Catherine I would probably have abandoned science in favor of a career in business or crime. Thom Pick also deserves mention for putting up with my idiosyncracies both as an office-mate and apartment-mate. I am indebted to Thom not only for his friendship but also for expanding my musical and cultural horizons and introducing me to a large percentage of the world's German population.

I am indebted to many members of the staff at Scripps for providing a pleasant buffer between the scientists who make the institution work and the administrators who don't. Anne, Jaynel, Karen, Carol, Elaine, Rickey and Brenda were more than patient with my administrative fiascos. Betty, Yvonne and the rest of the graduate office staff insulated me from much of the foolishness of the U.C. system. Stu Smith and the members of the Geological Data Center helped me with my occasional forays into the world of underway data both at sea and on the beach.

I acknowledge the people of San Diego and the U.C.S.D. administration for providing me with strong incentive to finish as quickly as I did. I also thank the residents of La Jolla for their most entertaining behaviour.

Copious thanks also to: Exxon, The Grateful Dead, Trader Joe's, AM/PM Mini Mart, Fuji, Moet & Chandon, Nine Inch Nails, Frank Sinatra, Toaster Lady, Book Man, Numerical Recipes, Unocal International, The Anchor Brewery, Dr. Hunter S. Thompson,

Chuy's, Buck's, Sun Microsystems, The Swap Meet, Music Trader, Foggy's Notion, Kodak, Ludwig van Beethoven, Carina's, Francis Ford Coppola, Joseph Fourier, Nissan, Henri Cartier-Bresson, James McNair, Hunter's Books, The Edinburgh Castle, The Doors, Kahuna's, The Posse (east), Miles Davis, Savage Republic and Charles Bukowski.

Above all, I thank my family. It was their unselfish dedication to my education that got me where I am now. I owe them more than I could ever express in writing.

Chapter 2, in full is a reprint of the material as it appears in *The Journal of Geophysical Research,* V.97, 1992. The dissertation author is the primary investigator and author of this paper.

Chapter 3, in full is a reprint of the material as it appears in *Geophysical Journal International* V.116, 1994. The dissertation author is the primary investigator and author of this paper.

Chapter 4, in full is a reprint of the material as it appears in *Geology*, V22, 1994. The dissertation author is the primary investigator and author of this paper.

Chapter 5, in full is a reprint of the material as it appears in *Geophysics,* V.7, 1992. The dissertation author is the primary investigator and author of this paper.

VITA

March 31, 1963	Born, Charleston, West Virginia.
1985	B.S. in Geology and Geophysics, University of Wisconsin, Madison.
1985 - 1987	Research Assistant, Physical Oceanography, University of Maryland, Horn Point Laboratories.
1987 - 1988	Teaching Assistant, Dept. of Geological Sciences, University of Texas at Austin.
1988 - 1989	Research Assistant, Institute for Geophysics, University of Texas at Austin.
1989	M.A. in Geophysics, University of Texas at Austin.
1989, 1990	Research Geophysicist, Exxon Production Research Houston, Texas.
1989 - 1993	Research Assistant, Scripps Institution of Oceanography, University of California San Diego, La Jolla, California.
1993	Ph.D. Earth Sciences, University of California, San Diego.

Publications

Refereed Journals

Small, C., A quantitative analysis of global mid-ocean ridge axial topography. *Geophysical Journal International*, In Press.

Small, C. and D.T. Sandwell, Comparison of satellite and shipboard gravity measurements in the Gulf of Mexico, *Geophysics* , 57, p.885-893, 1992.

Small, C. and D.T. Sandwell, An analysis of ridge axis gravity roughness and spreading rate, *J. Geophys. Res.*, 97, p.3235-3246, 1992.

Small, C., and D. T. Sandwell, An abrupt change in ridge axis gravity with spreading rate, *J. Geophys. Res.*, 94, 17383-17392, 1989.

Abstracts

Small, C. An E.O.F analysis of underway bathymetry profiles on the global mid-ocean ridge system. *EOS*, 73, p. 550, 1992.

Small, C. and D.T. Sandwell, Comparison of Geosat gravity profiles with high resolution shipboard gravity data in the Gulf of Mexico, *EOS*, 72, 1991.

Small, C. and D.T. Sandwell, Spreading rate dependence of gravity anomalies from Geosat, *EOS*, 71, p. 1570, 1990.

Buffler, R.T., G. Marton, D. Muller, L. Gahagan, D.S. Sawyer and C. Small, Crustal types and northwest trending structural features: Constraints on reconstructing the Gulf of Mexico basin, *Geological Society of America*, 1990.

Small, C. and D.T. Sandwell, Global gravity field roughness versus paleo-spreading rate from Geosat/ERM, *EOS*, 71, 1990.

Klepeis, K.A., L.A. Lawver, D.T. Sandwell, C. Small, C. Berg, The morphology and tectonic structure of the Shackleton fracture zone, *EOS*, 70, 1989.

Small, C., D.T. Sandwell and Y. Chen, Transition of ridge axis gravity/topography with spreading rate: The effect of a weak lower crust?, *EOS*, 70, 1989.

Small, C., J.Y. Royer and D.T. Sandwell, Discontinuous geoid roughness along the Southeast Indian ridge, *EOS*, 70, 1989.

Small, C. and D.T. Sandwell, An abrupt change in ridge axis gravity with spreading rate, *EOS*, 69, 1988.

Other

McLeod, J. and C. Small, Visualizing seafloor structures with satellite gravity measurements, in: *Proceedings of Visualization '92*, IEEE Computer Society Press, p. 424-427, 1992.

Lonsdale, P and C. Small, Ridges and rises: A global view, *Oceanus*, 34, Winter 1991/1992

Small, C., Accuracy of satellite-derived marine gravity data, Geoscience Research Report, Exxon Production Research Co., 1989.

Fields of Study

Major Field: Geophysics

Studies in Potential Theory
Professors George Backus, Robert Parker, David Sandwell (IGPP/SIO)

Studies in Satellite Remote Sensing
Professor David T. Sandwell (SIO, University of California San Diego)

Studies in Inverse Theory
Professor Robert L. Parker (IGPP, University of California San Diego)

Studies in Marine Geology
Professor Peter Lonsdale (S.I.O., University of California San Diego)
Professor Carl Bowser (University of Wisconsin, Madison)

Studies in Geophysical Data Analysis
Professor Robert L. Parker (IGPP, University of California San Diego)
Professors Paul Stoffa and Clark Wilson (University of Texas at Austin)
Professor C.S. Clay (University of Wisconsin, Madison)

Studies in Seismology
Professors J.F. Gilbert, J.B. Minster, L.M. Dorman (IGPP/SIO)
Professor P. Stoffa (University of Texas at Austin)
Professor C.S. Clay (University of Wisconsin, Madison)

Studies in Solid Earth Geophysics
Professors T.G. Masters, D.T. Sandwell (IGPP/SIO)
Professor C. Wilson (University of Texas at Austin)
Professor H. Wang (University of Wisconsin, Madison)

Studies in Seismic Data Interpretation and Basin Analysis
Professors R.T. Buffler, L.F. Brown (University of Texas at Austin)
Professor E.L. Winterer (SIO, University of California San Diego)

ABSTRACT OF THE DISSERTATION

Applications of Satellite Altimetry to Global Studies of Mid-Ocean Ridges and Continental Margins

Christopher S. Small

Doctor of Philosophy in Earth Sciences
University of California, San Diego, 1993
Professor David T. Sandwell, Chair

The increased resolution and coverage of satellite altimeter missions in recent years has had a significant impact on marine geophysics. Early altimeter data was used primarily for geodetic studies. Dense spatial coverage and increased spatial resolution have now made altimeter data a standard component of many marine geophysical surveys. The works contained in this dissertation use these advances to address questions which had been previously considered using only underway gravity and bathymetry measurements.

The first three chapters address the question of spreading rate dependence of mid-ocean ridge structure. Two of these chapters use altimetry measurements to investigate intermediate spreading rate transitions in ridge axis structure. The third of these chapters uses a collection of underway bathymetry profiles to verify the findings of previous studies which used only altimeter data. We find that the spreading rate dependence which characterizes slow spreading ridge structure is not present at higher spreading rates and that the transition from rate dependence to rate independence coincides with the transition from axial valley structure to axial ridge structure. On the main mid-ocean ridge system this change occurs on relatively unexplored parts of the Southeast Indian Ridge

and Pacific Antarctic Rise. Recently declassified altimeter data show these transitions in unprecedented detail.

The final two chapters consider the feasibility of using satellite altimeter data for studies of continental margin structure. In a comparison of shipboard and satellite gravity measurements in the Gulf of Mexico we find that individual satellite gravity profiles accurately (~6 mGal RMS) resolve features as short as 25 km wavelength when low degree spherical harmonic models are used to constrain the long wavelength components ($l < 180$) of the field. In the final chapter we apply a new method for computing terrain corrections to satellite gravity data in the Gulf of Mexico in order to constrain deep basin structure. Terrain corrected gravity data remove the effects of the extreme topography in the gulf and provide constraints on the extent of oceanic crust in the poorly explored southern gulf.

Chapter 1

Introduction

Background

One of the earliest observations of global seafloor morphology was the difference between fast and slow spreading mid-ocean ridge axes. Early exploration of the midocean ridge system by Menard (1967), Heezen (1967) and others revealed consistent differences in axial structure and flanking topography. As more of the ridge system was surveyed it also became apparent that fast and slow spreading ridges are segmented differently. The traditional view of the ridge system states that slow spreading ridges are characterized by a 1-2 km deep axial valley bounded by rift valley mountains and rugged flanking topography while fast spreading ridges are characterized by a continuous axial ridge, less than 1 km in height and bounded by smoother flanking topography. Slow spreading ridges were also considered to be composed of discrete segments 50-100 km in length and offset by numerous transform faults while fast spreading ridges were considered more continuous and only occasionally offset by transform faults. This view of the ridge system evolved incrementally as each new expedition contributed additional underway profiles to the collection of data upon which it was based.

The intensive, multidisciplinary study of individual ridge segments and the advent of multi-narrow beam sonar have modified our view of the ridge axis. Projects such as FAMOUS (Heirtzler and Le Pichon, 1974) and RISE (RISE Team, 1980) made substantial contributions to our understanding of ridge axis processes. Dense spatial coverage, submersibles, deep towed instrument packages and the combination of several types of geological, geophysical and geochemical observations of the same area allowed geoscientists to better understand the relationships of observable quantities such as morphology, petrology, seismic structure, heat flow, gravity and magnetics. Although these studies provide a wealth of information about the formation of oceanic crust at the ridge axis, they do not necessarily offer a representative description of the highly variable ridge system as a whole. The widespread availability of multi-narrow beam echo sounders has, however provided an efficient means of locating the ridge axis and mapping its most fundamental observable quantities of morphology and segmentation. Numerous multibeam surveys of the northern Mid Atlantic Ridge and northern East Pacific Rise have modified the traditional view of the ridge system. It is now known that both fast and slow spreading ridges are considerably more segmented than was previously believed. In particular, the distinction of smaller scale migrating offsets from the larger scale, more stable transform offsets has been

recognized. It has also been shown that axial depth and relief often vary in a consistent manner with distance from different types of offset on both fast and slow spreading ridges.

Although systematic multibeam surveys provide a more complete view of the ridge axis, the majority of the ridge system has been surveyed only with single wide beam echosounders. As mentioned above, the vast majority of our knowledge of ridge axis morphology is based on multibeam surveys of the northern Mid Atlantic Ridge and the northern East Pacific Rise. In fact, almost the entire East Pacific Rise axis has now been mapped with multibeam sonar (Francheteau et al, 1987; Hey et al, 1985; Lonsdale, 1989; Macdonald et al, 1984). While these ridges provide convenient access to fast and slow spreading end members of the system, they comprise only a small percentage of the global midocean ridge system. Current knowledge of the ridges in the Southern Oceans is still based heavily on expeditions conducted prior to the mid 1970's (Smith, 1993). Because very few multibeam surveys have been conducted on the ridges in the Southern Oceans most of the available data consist of isolated underway profiles which cross the ridge at random locations and orientations. It is this collection of data upon which our initial view of the midocean ridge system was gradually constructed. Although the simplified view of the ridge system has undergone extensive modification the initial observations of axial morphology are still generally upheld.

The introduction of marine gravity field mapping with satellite altimeters has changed our view of the world's ocean basins (Haxby, 1987). Altimeter data have been used to map seamount distributions (Craig and Sandwell, 1988), to constrain plate reconstructions (Mayes et al, 1989) and to model fracture zone structure and evolution (Crough, 1979; Sandwell and Schubert, 1982). Previously unknown features have been discovered as a result of satellite altimeter missions (Haxby & Weissel, 1987). It was not until the Geosat Exact Repeat Mission (ERM) that satellite altimeters achieved the accuracy and coverage necessary to resolve small scale (< 50 km) features in the marine gravity field (Sandwell and McAdoo, 1990). These data offered the first detailed look at many parts world's ocean basins and made possible global studies of much finer scale features than could be resolved previously with satellite altimeters. In one such study Small and Sandwell (1989) observed that, in addition to the previously known decrease in axial valley expression with increasing spreading rate, an intermediate rate transition in both axial anomaly character and spreading rate dependence occurs within a relatively narrow range of spreading rates (60-80 mm/yr) on the primary mid-ocean ridge system. It was speculated that this transition may reflect a change in the mechanism by which seafloor is formed at the ridge axis.

Despite the massive effort expended on mid-ocean ridge studies there is still not a consensus on the mechanism controlling crustal structure and axial morphology on the midocean ridge system. This seems to be the result of uncertainty surrounding the factors which control the process of crustal accretion and lithospheric formation at the ridge axis. If oceanic crustal structure

and ridge axis morphology are influenced by spreading rate, segmentation, mantle upwelling, tectonic history and local mantle conditions then it would be desirable to quantify the relative importance of each of these factors. Spreading rate is undisputably the dominant first order control on most of the ridge system although it is certainly not the only factor influencing this process. The existence of anomalous ridges such as the Reykjanes Ridge and the Australian - Antarctic Discordant Zone prove that the influence of spreading rate may be overridden by larger scale controls such as mantle flow and thermal structure. Observations from regional sidescan and multibeam surveys indicate that segmentation also exerts a profound influence on ridge morphology although these controls are inherently more difficult to quantify than spreading rate. Although small local variations in spreading rate have been observed (Fox et al, 1991), simple models of global plate motions provide reasonably accurate estimates of spreading rates over most of the ridge system (DeMets et al, 1990; Minster and Jordan, 1978).

Unlike spreading rate, the segmentation of a ridge is known only after it has been completely surveyed. Although the large scale segmentation is reasonably well known on a global basis, smaller scale segmentation is known only on ridge segments that have been mapped with sidescan or multibeam surveys. For this reason it is possible to quantify the dependence of ridge axis morphology on large scale segmentation although unmapped small scale segmentation may exert a larger influence on local morphology. An additional difficulty arises in that it is generally not known whether segmentation is controlled by the regional tectonic history of a ridge segment or whether the regional tectonic history is controlled by the segmentation. How either of these factors are related the dynamics of mantle upwelling and melt segregation also remains unknown. Spreading rate may be considered a more absolute control in the sense that both the regional tectonic history and the pattern of passive upwelling at the ridge crest are affected by large scale divergent plate motions. Although all of these factors influence axial morphology, only spreading rate is known accurately over the entire midocean ridge system at present.

The basic observation that axial valleys are characteristic of slow spreading centers while axial ridges are characteristic of fast spreading centers has stimulated a multitude of models for midocean ridge dynamics (eg. Sleep, 1969; Tapponier and Francheteau, 1978). Although early models usually attempted to explain only one end member of the system, recent models have focused more on a single mechanism to explain both fast and slow spreading ridges (eg. Phipps Morgan et al, 1987).

A necessarily common feature of most ridge axis models is a dependence on numerous, weakly constrained parameters. Even in the event that the tectonic history, segmentation and spreading rate are known, an understanding of their interdependence still presupposes a detailed knowledge of mantle thermal and flow fields, crustal hydrothermal circulation and rheology as well as melt generation, composition and migration patterns. Because of these complications most ridge

models are limited to two dimensional flow simulations in which the spreading rate is the primary independent variable.

Currently, there are at least two midocean ridge models which are able to produce an axial valley at slow spreading rates and an axial ridge at fast spreading rates. The model of Phipps Morgan et al (1987) treats the oceanic lithosphere as a continuously deforming medium in which thickness variations give rise to internal bending moments which produce axial topography that varies with spreading rate. While this model can produce axial valleys which shrink with increasing spreading rate, it's ability to produce a transition has not yet been investigated. The model proposed by Chen and Morgan (1990) is based on the concept of a "decoupling chamber" of weak lower crust which allows the brittle crust at the rise axis to respond independently to the motions of the asthenosphere below. When the width of the decoupling chamber exceeds a zone of extensive deformation at the rise axis the deformed crust is free to respond isostatically forming an axial rise rather than an axial valley. Although this model can explain the rate dependence/independence discussed below, it is rather sensitive to a number of poorly constrained lithospheric parameters. In this respect, the modeling of mid-ocean ridge dynamics has advanced beyond the availability of observational constraints. The common objective of the works in this dissertation is to provide quantitative constraints on the large scale patterns observed on the global mid-ocean ridge system.

The mid-ocean ridge studies included in this thesis attempt to place constraints on the spreading rate dependence of ridge axis structure and morphology using both satellite gravity and underway bathymetry data. The primary emphasis is on the nature of the transition in axial morphology and rate dependence which occurs at intermediate spreading rates. Understanding of this phenomenon is critical to our understanding of the mechanism(s) by which oceanic crust is formed at all spreading centers. Furthermore, the similarity to the spreading rate dependence of ridge flank bathymetric roughness strongly implies a genetic link between the ridge axis morphology and ridge flank abyssal hill morphology. An improved understanding of this relationship may allow paleo-spreading rates and other ridge axis parameters to be inferred from abyssal hill morphology just as past plate reorganizations are now inferred from structure on the rise flanks. Although these global studies necessarily lack the detail of intensive local surveys, it is hoped that these results will offer insight complementary to the findings of local surveys.

An additional application of global satellite altimeter data is the study of continental margin structure and evolution. Two different aspects of this application are discussed in the final two chapters. In many areas, satellite gravity data provide the most detailed look at continental margin structure yet available. The studies included here are both located in the Gulf of Mexico. In many ways the Gulf of Mexico is an ideal testing ground as it is one of the most heavily probed pieces of real estate on the planet. The complexity of both the structure and the origin of the gulf poses

many questions which may profit from investigations using satellite data. Even the low resolution coverage provided by the widely spaced Geosat ERM and ERS-1 profiles is an improvement over previously available underway data in the southern gulf. This situation will improve with the eventual availability of closely spaced ERS-1 profiles and possibly Geosat GM profiles. Although a great deal of work has been done on continental margin structure and evolution (Klitgord et al, 1988), almost no use has been made of satellite altimeter data. In this sense, the studies included here will serve as preliminary investigations of the feasibity of future studies.

Organization of the Thesis

This thesis is composed of five distinct studies; three related to the systematics of global mid-ocean ridge structure and two concerned with the application of altimeter derived gravity to continental margin structure. Each of these studies is summarized below.

In the second chapter we extend our initial study of ridge axis gravity anomalies using Geosat Exact Repeat Mission (ERM) profile data (Small and Sandwell, 1989). Although the initial study was the first global investigation of ridge axis gravity anomaly characteristics, it was hindered by an incomplete knowledge of the exact location and segmentation of the ridge axis in many areas. Because this study made use of the polarity of the axial anomaly, small errors in the location of the ridge axis could result in a change in polarity of the axial anomaly. For this reason we limited ourselves to 44 representative profiles on the global ridge system. While this provided significantly better coverage than was previously available on some of the ridges in the southern oceans, it did neglect a large amount of potentially useful altimeter data. By using roughness estimates of the axial anomaly we are able to investigate the amplitude variation in greater detail and demonstrate more convincingly the nature of the transition from slow to fast spreading ridge structure at intermediate spreading rates. The declassification of Geosat Geodetic Mission (GM) data in the areas south of 60°S also revealed a graphic example of a relatively abrupt transition in axial anomaly character along a previously unexplored segment of the Pacific Antarctic Rise. This paper provides the first detailed look at this transition.

In the third chapter a global analysis of 156 underway bathymetric profiles is used to verify the assumption that the characteristics of the axial gravity anomaly are a consequence of ridge axis morphology. Relief of axial morphology is shown to vary with spreading rate and location in a manner equivalent to the gravity anomalies seen in the satellite data. In addition to corroborating the conclusions of the gravity studies, additional constraints are placed on variations in axial depth and bathymetric roughness on the mid-ocean ridge system. It is shown that axial valley deepening is coincident with flanking uplift as has often been assumed (but never proven) in models of ridge axis dynamics. It is also shown that bathymetric roughness varies discontinuously with spreading rate in a manner similar to axial morphology and gravity rather than continuously as has been proposed by Malinverno (1991) for ridge flank roughness.

The fourth chapter makes use of recently declassified Geosat GM data in the areas south of 30°S to look in greater detail at the previously discussed ridge axis transitions in the southern oceans. In this preliminary study the accuracy and resolution of the recently available two dimensional (2D) gravity grid is established and a more detailed quantification of axial anomaly

amplitude variations is compared with previous studies. Detailed maps of several of these transitions are discussed with relation to nearby hot spots.

We move from the mid-ocean ridge to the continental margin in the fifth and sixth chapters of the thesis. The fifth chapter is an investigation of the ability of individual altimeter profiles to resolve free air gravity anomalies on continental margins using a one dimensional (1D) Hilbert transform. When this study was conducted (1991) Geosat ERM altimeter profiles provided the most detailed view of the gravity field available in many areas. Although intermediate resolution, 2D coverage is currently available in the areas south of 30°S, wide track spacing still necessitates a significant loss of resolution in gridded data north of 30°S. In a comparison with some of the highest quality marine gravity data currently available we find that individual altimeter profiles can accurately (< 6 mGal RMS) recover anomalies as short as 25 km wavelength and that incorporation of longer wavelength spherical harmonic models only offers significant improvement for spherical harmonic degrees less than 180.

The final chapter investigates an additional application of satellite gravity data to continental margin studies. In this chapter we present results of a preliminary study of the deep structure of the Gulf of Mexico using terrain corrected satellite gravity data. By using a new method for calculating terrain corrections (Parker, 1993) we are able to account for the gravity anomalies resulting from extreme topographic variations in the Gulf of Mexico and constrain the large scale structure in the poorly understood southern gulf. These results may help to delineate the distribution of oceanic crust in the gulf and to constrain models for it's early formation.

References

Chen, Y., and W. J. Morgan, Rift valley/no rift valley transition at mid-ocean ridges, *J. Geophys. Res.*, 95, 17571-17583, 1990a.

Chen, Y., and W. J. Morgan, A non-linear rheology model for mid-ocean ridge topography, *J. Geophys. Res.*, 95, 17583-17604, 1990b.

Craig, C. H., and D. T. Sandwell, Global distribution of seamounts from Seasat profiles, *J. Geophys. Res.*, 93, 10408-10420, 1988.

DeMets, C.,R.G. Gordon, D.F. Argus, S. Stein, Current Plate Motions, *Geophys. J. Int., 101*, 425-478, 1990.

Fox, P. J., N. R. Grindlay, and K. C. Macdonald, The Mid-Atlantic Ridge (31°S-34.30°S): Temporal and spatial variations of the accretionary process, *Mar. Geophys. Res.*, 13, 1-20, 1991.

Francheteau, J., A. Yelles-Chaouche, and H. Craig, The Juan Fernandez microplate north of the Pacific-Nazca-Antarctic plate junction at 35° S, *Earth Planet. Sci. Lett.*, 86, 253-268, 1987.

Haxby, W.F., and J.K. Weissel, Evidence for small-scale mantle convection from Seasat altimeter data, J. Geophys. Res., 91, p.3507-3520, 1986.

Hey, R. N., D. F. Naar, M. C. Kleinrock, W. J. P. Morgan, and J. G. Schilling, Microplate tectonics along a superfast seafloor spreading system near Easter Island, *Nature*, 317, 320-325, 1985.

Heirtzler, J. R., and X. LePichon, FAMOUS: A plate tectonics study of the genesis of the lithosphere, Geology, 2, 273-278, 1974.

Lonsdale, P., Segmentation of the Pacific-Nazca spreading center, 1°N-20°S, *J. Geophys. Res.*, 94, 12197-12225, 1989.

Macdonald, K. C., J. C. Sempere, and P. J. Fox, East Pacific Rise from Siqueros to Orozco fracture zones: Along strike continuity of axial neovolcanic zone and structure and evolution of overlapping spreading centers, *J. Geophys. Res.*, 89, 6049-6069, 1984.

Malinverno, A., Inverse square-root dependence of mid-ocean ridge flank roughness on spreading rate, *Nature*, 352, 58-60, 1991.

Mayes, C. L., L. A. Lawver, and D. T. Sandwell, Tectonic history and new isochron chart of the South Pacific, *J. Geophys. Res.*, 95, 8543-8567, 1990.

Menard, H.W., Seafloor Spreading, Topography and the Second Layer, *Science*, 157, p.923-924, 1967.

Minster, J. B., and T. H. Jordan, Present day plate motions, J. Geophys. Res., 83, 5331-5354, 1978.

Parker, R.L. A new method for terrain correction of large amplitude topography, Submitted to *Geophysics*, 1993

Phipps Morgan, J., E. M. Parmentier, and J. Lin, Mechanisms for the origin of midocean ridge axial topography: Implications for the thermal and mechanical structure of accreting plate boundaries, *J. Geophys. Res.*, 92, 12823-12836, 1987.

RISE_Team, East Pacifi Rise: Hot springs and geophysical experiments, *Science*, 207, 1421-1433, 1980.

Sandwell, D., and G. Schubert, Lithospheric Flexure at Fracture Zones, *J. Geophys. Res.*, 87, 4657-4667, 1982.

Sandwell, D.T. and D.C. McAdoo, High Accuracy, High Resolution Gravity Profiles from 2 Years of the Geosat Exact Repeat Mission, *J. Geophys. Res.*, 95, p.3049-3060, 1990.

Sleep, N.H. Sensitivity of heat flow and gravity to the mechanism of seafloor spreading, *J. Geophys. Res.*, 74, 542-549, 1969.

Small, C. and D.T. Sandwell, An Abrupt Change in Ridge Axis Gravity with Spreading Rate, *J. Geophys. Res.*, 94, p.17383-17392, 1989.

Smith, W. H. F., On the accuracy of digital bathymetric data, *J. Geophys. Res.*, 98, p.9591-9605, 1993.

Tapponier, P. and J. Francheteau, Necking of the lithosphere and the mechanics of slowly accreting plate boundaries., *J. Geophys. Res.*, 83, 3955-3970, 1978.

Chapter 2

An Analysis of Ridge Axis Gravity Roughness and Spreading Rate

Christopher Small and David T. Sandwell

Submitted to *Journal of Geophysical Research*
March 23, 1991
Accepted September 25, 1991
Published March 1992

JOURNAL OF GEOPHYSICAL RESEARCH, VOL. 97, NO. B3, PAGES 3235-3245, MARCH 10, 1992

An Analysis of Ridge Axis Gravity Roughness and Spreading Rate

CHRISTOPHER SMALL AND DAVID T. SANDWELL

Scripps Institution of Oceanography, La Jolla, California

Fast and slow spreading ridges have radically different morphologic and gravimetric characteristics. In this study, altimeter measurements from the Geosat Exact Repeat Mission (Geosat ERM) are used to investigate spreading rate dependence of the ridge axis gravity field. Gravity roughness provides an estimate of the amplitude of the gravity anomaly and is robust to small errors in the location of the ridge axis. We compute gravity roughness as a weighted root mean square (RMS) of the vertical deflection at 438 ridge crossings on the mid-ocean ridge system. Ridge axis gravity anomalies show a decrease in amplitude with increasing spreading rate up to an intermediate rate of ~60-80 mm/yr and almost no change at higher rates; overall the roughness decreases by a factor of 10 between the lowest and highest rates. In addition to the amplitude decrease, the range of roughness values observed at a given spreading rate shows a similar order of magnitude decrease with transition between 60 and 80 mm/yr. The transition of ridge axis gravity is most apparent at three relatively unexplored locations on the Southeast Indian Ridge and the Pacific-Antarctic Rise; on these intermediate rate ridges the transition occurs abruptly across transform faults.

INTRODUCTION

It is well known that mid-ocean ridge topography varies as a function of spreading rate [*Menard*, 1967]. Slow spreading ridges (15-30 mm/yr) are characterized by a deep (1-3 km) axial valley and rugged flanking topography while fast spreading ridges (100-160 mm/yr) are characterized by a small axial ridge and smoother flanking topography [*Macdonald*, 1986]. Free air gravity anomalies over fast and slow spreading ridges also reflect this difference in structure. Fast spreading ridges have small (<10 mGal) positive free air anomalies, while slow spreading ridges have larger (>30 mGal) negative anomalies flanked by positive anomalies [*Cochran*, 1979; *Small and Sandwell*, 1989]. Through an analysis of the gravity/topography transfer function over the Mid-Atlantic Ridge (MAR) and the East Pacific Rise (EPR), *Cochran* [1979] has shown that the gravity/topography ratio decreases with increasing spreading rate; this implies either a lithospheric elastic thickness which is dependent on spreading rate or a change in the mode of compensation. Overall, these results suggest that topography, gravity, and the gravity/topography ratio all vary with spreading rate, and perhaps their variations are all different. Here we make use of the uniform global coverage of satellite gravity data to investigate the amplitude of short-wavelength ridge axis gravity anomalies and to determine how the amplitude varies with spreading rate.

While the location of the entire mid-ocean ridge plate boundary is approximately known from compilations of underway bathymetry data, only a few areas have been mapped in detail. The majority of mid-ocean ridge surveys are made on the slow spreading central MAR and the fast spreading northern EPR because these sites are conveniently located and include the end-member examples. However, since our knowledge of mid-ocean ridges is based primarily on these surveys, almost nothing is known about the change in ridge axis morphology that occurs at the intermediate spreading rates. The major intermediate spreading rate ridges are located in remote southern ocean areas (i.e., Pacific Antarctic Rise and Southeast Indian Ridge) and thus have remained almost completely unsurveyed by ships.

At present, satellite altimeters provide the only source of data with sufficient accuracy and areal coverage to study the entire ridge system at a 10-km spatial resolution along widely spaced profiles (~80 km). High-accuracy (~1 μrad = 0.98 mGal) and high-resolution (~10 km half wavelength) vertical deflection profiles were obtained by averaging up to 44 repeat cycles from the Geosat Exact Repeat Mission (ERM) [*Sandwell and McAdoo*, 1990]. Using these new data, we performed a systematic analysis of the roughness of the gravity field over the global mid-ocean ridge system. In well-surveyed northern ocean areas, the Geosat ERM profiles confirm the shipboard measurements. In the poorly surveyed southern ocean areas, the Geosat ERM profiles provide new information on the gravity and state of isostasy of the ridge axis. This gravity roughness analysis supports our earlier finding that the ridge axis gravity signature does not change gradually with spreading rate but rather changes abruptly in specific locations which occur within a narrow range of intermediate rates [*Small and Sandwell*, 1989].

The main advantage of computing gravity roughness, instead of measuring the amplitude and polarity of the ridge axis anomaly, is that the roughness does not depend on a precise knowledge of the location of the ridge axis. As noted in our earlier study [*Small and Sandwell*, 1989], the polarity of the ridge axis anomaly can be ambiguous when the position of the ridge axis is uncertain by more than about 15 km. The calculation of gravity roughness removes this polarity ambiguity so that the results are not affected significantly by errors in ridge axis location. To further demonstrate the nature of the abrupt transition, we present a new gravity map of the southern Pacific-Antarctic Rise based on extremely dense altimeter coverage (~2-km track spacing). In this area there is no ambiguity in the location of the ridge axis; we observe a sharp transition from an axial high to an axial valley that occurs at a spreading rate of 64 mm/yr.

ESTIMATION OF GRAVITY ROUGHNESS

In this study, we consider roughness of the along-track vertical deflection as a measure of roughness of the gravity field. The vertical deflection is the along-track derivative of the geoid (i.e., sea

Paper number 91JB02465.
0148-0227/92/91JB-02465$05.00

surface slope) and is proportional to the horizontal component of the gravity anomaly vector. The procedure used to calculate stacked vertical deflection profiles from Geosat ERM data is discussed by *Sandwell and McAdoo* [1990]. Because the derivative operator acts as a high-pass filter, vertical deflection profiles tend to accentuate short-wavelength features while suppressing long-wavelength orbit errors and oceanographic effects.

A variety of methods can be used to estimate the roughness of a profile. The power spectrum provides a convenient summary of the distribution of energy as a function of wavelength. *Brown et al.* [1983] averaged the power over bands of wavenumbers to study geoid roughness using Seasat data. An advantage of this method is that it provides roughness estimates over a wide range of wavelengths. One limitation is that the profiles must be long enough to obtain reliable spectral estimates in the longest band, thus limiting the spatial resolution of the roughness map. *Gilbert et al.* [1989] use the envelope of band-pass-filtered Seasat data to estimate the geoid roughness for the South Atlantic. This method extracts the roughness in the shortest wave band which results in better spatial resolution.

Since we are primarily interested in the shortest-wavelength anomalies resolvable in the Geosat profiles, we have adopted a modified version of the *Gilbert et al.* [1989] method. Individual vertical deflection profiles are first band-pass filtered by convolution with Gaussian kernels. After high-pass and low-pass filters are applied, the roughness R_t at a given point t along the filtered profile is the weighted average of the squares of the surrounding values:

$$R_t = \left[\frac{1}{W} \sum_{i=-n}^{n} w_i \, \eta_{t+i}^2 \right]^{1/2}$$

where w_i are the individual weights, W is the sum of the weights, and η_{t+i} are the vertical deflections. The weights consist of $2n + 1$ samples of a Gaussian function with a range of $\pm 3\sigma$.

As would be expected, the roughness estimate is sensitive to the size of the window. Larger windows attenuate small-scale roughness variations, while narrower windows give a more localized roughness estimate with greater spatial resolution. Because the data are band-pass-filtered before roughness is computed, the mean is not removed from the estimate. Therefore, if the window is significantly narrower than the wavelength of a particular feature the roughness will appear to decrease near the inflection points and increase near the extrema. This becomes apparent if one considers a narrow window operating on a sinusoid, for which the roughness should remain constant. We have experimented with different window lengths and found that by setting the window length equal to the long-wavelength cutoff of the band-pass filter we can accurately detect the salient features in the data without introducing artifacts.

The selection of the long- and short-wavelength cutoffs for the band-pass filter is dictated by two factors: the characteristic wavelengths of the features being investigated and the resolution of the data. *Sandwell and McAdoo* [1990] have shown that a reasonable resolution limit for the 44-fold stacked Geosat ERM data is about 20 km. Thus 20 km is chosen as the short-wavelength cutoff. The selection of a long-wavelength cutoff is less straightforward and requires more careful consideration.

One way of establishing the proper long-wavelength cutoff is to analyze the power spectra of vertical deflection profiles. Profiles from two areas were selected for this analysis: a gravitationally smooth region in the eastern equatorial Pacific and a gravitationally rough region in the equatorial Atlantic (Figure 1). To obtain reliable

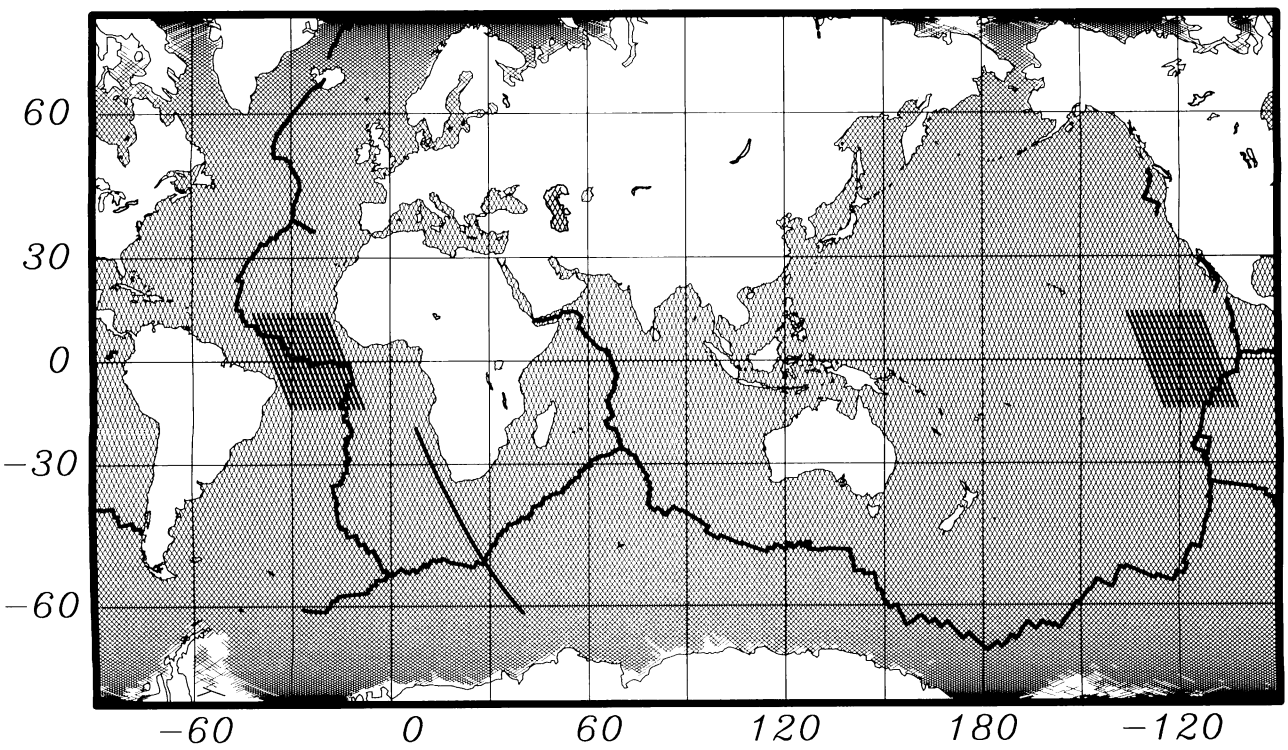

Fig. 1. Index map showing track coverage of the Geosat ERM and location of mid-ocean ridge plate boundary (thick line). Thick lines in the equatorial Atlantic and eastern Pacific show tracks used to estimate the power spectra of the vertical deflection profiles. Thick line south and west of Africa marks the profile shown in Figure 3.

spectral estimates, 16 profiles (1024 points long) were selected from each area. After windowing each profile, the power spectra were computed [*Welch*, 1967]. The composite spectra for each area are shown in Figure 2. At wavelengths longer than ~100 km, the spectra for both areas are relatively flat, and the Pacific data have about a factor of 10 less power than the Atlantic data. In each case there appears to be a natural corner frequency at ~100 km. For wavelengths less than 100 km the spectra of the rough and smooth areas decay at different rates. The spectral decay rate is related to the roughness of a surface [*Mandelbrot*, 1982]. For this reason, the difference in spectral slope for wavelengths between approximately 20 and 100 km is of particular interest.

Another method of establishing the long-wavelength cutoff is to compare the gravity profiles with topography profiles to determine the band where they have a high cross correlation. Cross spectral analyses of marine gravity and topography data have show high spectral coherence (and near zero phase) for wavelengths between 15 and 150 km [e.g., *Cochran*, 1979; *McNutt*, 1979]. Within this band both Airy and flexural compensation models also predict a high ratio of gravity to topography. For this reason we expect the vertical deflection roughness calculated in the 20-100 km band to be highly correlated with bathymetric roughness.

To demonstrate this high correlation between vertical deflection roughness and bathymetric roughness, we have compared profiles along coincident track lines. We chose example profiles from regions created at both slow and fast spreading ridges. Bathymetric roughness was computed from Sea Beam center-beam profiles using the methods described above. The first profile (slower spreading) was collected in the South Atlantic by the R/V *Conrad* in 1985 and runs from 8.4°S, 325.7°E to 28.1°S, 334.8°E along an ascending Geosat ground track. This 2400-km profile crosses several prominent fracture zones and a large seamount thus providing significant changes in both bathymetry and gravity roughness. The correlation coefficient between the vertical deflection roughness and bathymetry roughness is 0.95 for the entire profile and 0.88 for the ridge flanking portion of the profile excluding the seamount. A similar analysis was conducted for a Sea Beam profile collected in the eastern Pacific (faster spreading) by the R/V *Thomas Washington* in 1987. This 2900-km profile follows a descending Geosat ground track from 25°N, 235°E to 0°, 226°E and also provides several changes in topographic and gravimetric roughness. A comparison of this bathymetric roughness profile and the coincident satellite gravity roughness profile yielded a correlation coefficient of 0.97. Both examples demonstrate that in the 20-100 km wavelength band, variations in satellite gravity roughness accurately reflect variations in bathymetry roughness.

On the basis of these comparisons and the power spectral analyses shown in Figure 2, we adopted the 20-100 km wavelength range for our roughness analysis. The various processing steps are illustrated in Figure 3 for a profiles crossing the Southwest Indian Ridge (bottom profile, unfiltered; middle profile, band pass filtered; top profile, roughness estimate). Along-track vertical deflection roughness was calculated for all of the Geosat profiles shown in Figure 1. The roughness estimates were gridded to produce a global roughness map (Plate 1). (It should be noted that this map is used only to display the global data; individual roughness profiles are used for all of the quantitative analyses below.) The most striking feature of the global roughness map is the variation in roughness along the spreading ridges. The slow spreading ridges (e.g., Mid-Atlantic Ridge and Southwest Indian Ridge) show high roughness at the ridge axis (~15 μrad) and lower roughness (~6 μrad) on the flanks. In contrast, the fast spreading ridges (e.g., East Pacific Rise and northern Pacific-Antarctic Rise) show

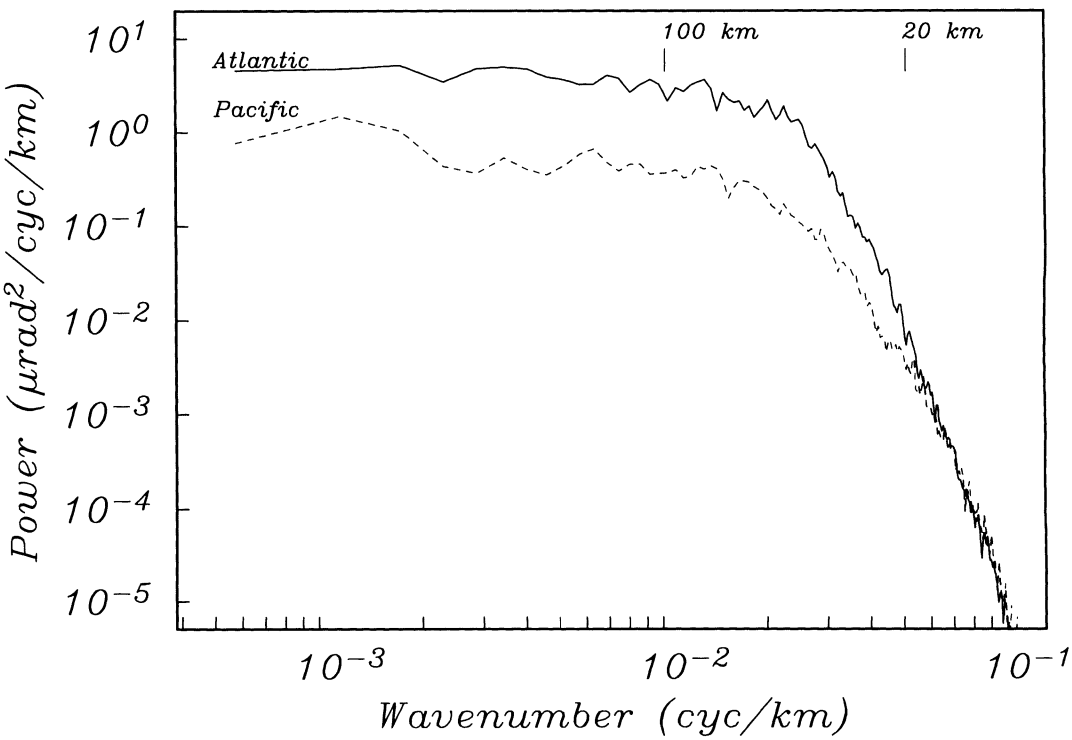

Fig. 2. Estimates of power spectra for vertical deflection profiles from two regions shown in Figure 1. Each spectrum is the composite of 16 profiles, 1024 points long. The Atlantic gravity field has more power than the Pacific at all wavelengths. Note the differences in the slopes of the power spectra between ~100 km and ~20 km.

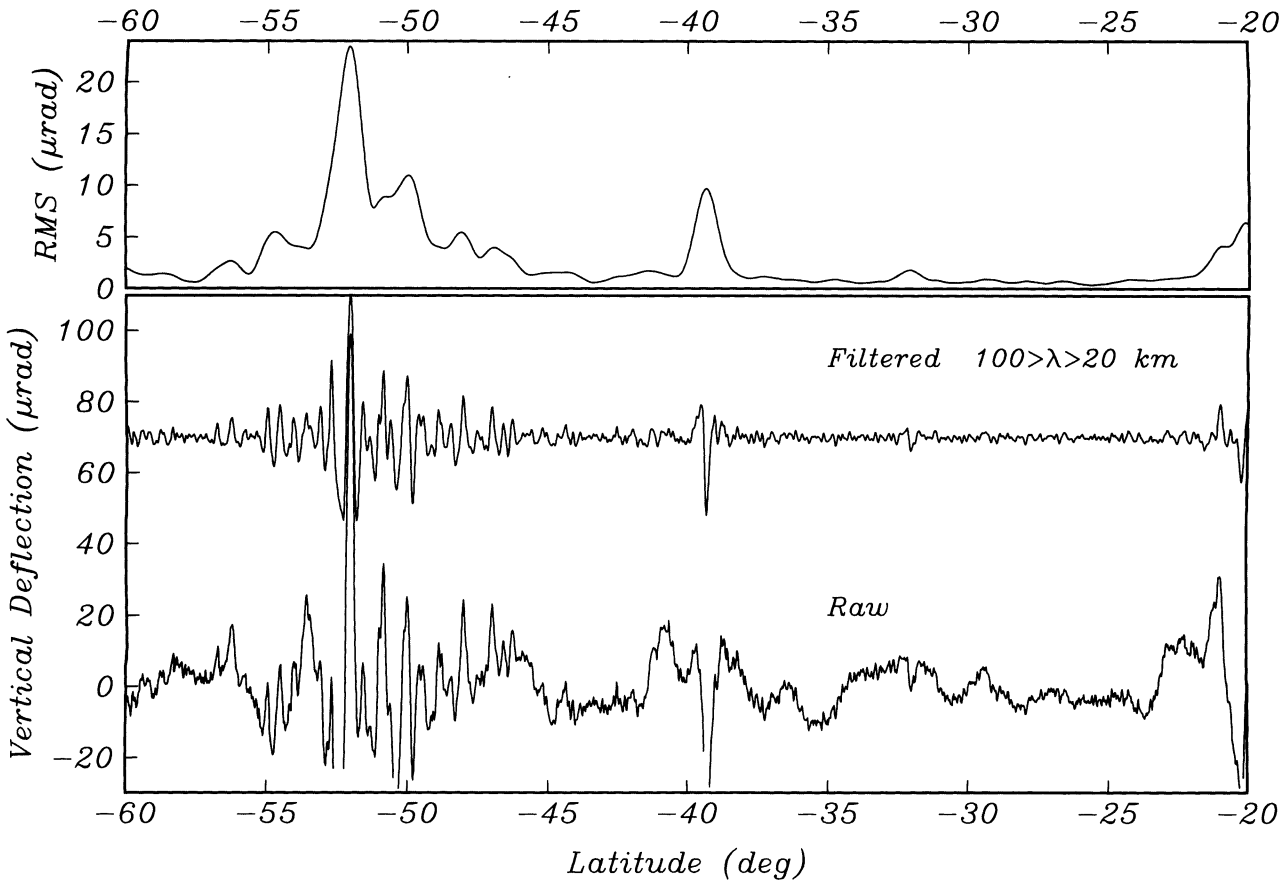

Fig. 3. Processing sequence: bottom, unfiltered vertical deflection profile; middle, profile after band-pass filtering ($20 < \lambda < 100$ km); top, along track roughness. The prominent feature near -52° is the anomaly due to the Southwest Indian Ridge. The smaller feature near -40° is anomaly of the Falkland Agulhas Fracture Zone. The anomaly near -20° results from the Walvis Ridge. The location of the profile is shown in Figure 1.

generally low roughness (< 2 μrad) on both the axis and the flanks (except near seamounts). In the remainder of this paper we provide a quantitative analysis of these first-order ridge axis roughness variations with special emphasis on the transition from high roughness to low roughness at intermediate spreading rates.

Mid-ocean Ridge Plate Boundary

The dynamics and structure of a mid-ocean ridge are certain to be influenced by the proximity of subduction zones (Chile Rise, Juan de Fuca, Gulf of California), the presence of large-scale propagating rifts (Easter microplate, Juan Fernandez microplate, Galapagos Rift) and the effects of continental rifting (Red Sea, Gulf of Aden). In this study we separate the continuous system into three major segments (Atlantic, Pacific, and Indian), smaller isolated ridges (Juan de Fuca, Cocos, Chile), and ridge segments which are known to be anomalous (Reykjanes Ridge, Australian-Antarctic Discordance Zone). In order not to complicate the analysis unnecessarily we have excluded continental rifts and propagating rifts.

We use a digitized plate boundary to define ridge and offset segments of the divergent plate boundaries. The plate boundary is derived primarily from published sources (Table 1), although some regions were digitized from GEBCO [*Canadian Hydrographic Service*, 1982] charts. Along the southern part of the Pacific Antarctic Rise, the plate boundary was determined from a high-resolution gravity map; this is discussed in the results section of this paper.

If one assumes that individual ridge segments and offsets (primarily transforms) can be approximated by line segments, then the plate boundary is described by the location of ridge transform intersections (RTIs). Once the RTIs are located, segments are identified as either ridges or transforms by comparing the azimuth of the segment to the azimuth of the plate motion vector at the midpoint of the segment. Plate motion azimuths and rates were computed using the NUVEL1 plate motion model [*DeMets et al.*, 1990]. We experimented with different criteria and found that the plate boundary could be represented accurately by categorizing any segment with an azimuth within ±45° of the plate motion vector as an offset and all others as ridge segments. Overlapping spreading centers were treated separately. The distribution of azimuths is strongly bimodal (as would be expected), and this scheme consistently picked alternating ridges and offsets correctly. An example of this procedure is shown in Figure 4. The vertical deflection profiles crossing the ridge segments are shown in Figure 5.

After calculating the along-track roughness profiles and identifying the ridge and transform segments, the roughness was extracted at the intersections of the satellite tracks and the plate boundary. Roughness values, spreading rates, intersection angles, and distances to the nearest RTI were computed for every intersection point. A total of 438 ridge crossings were detected.

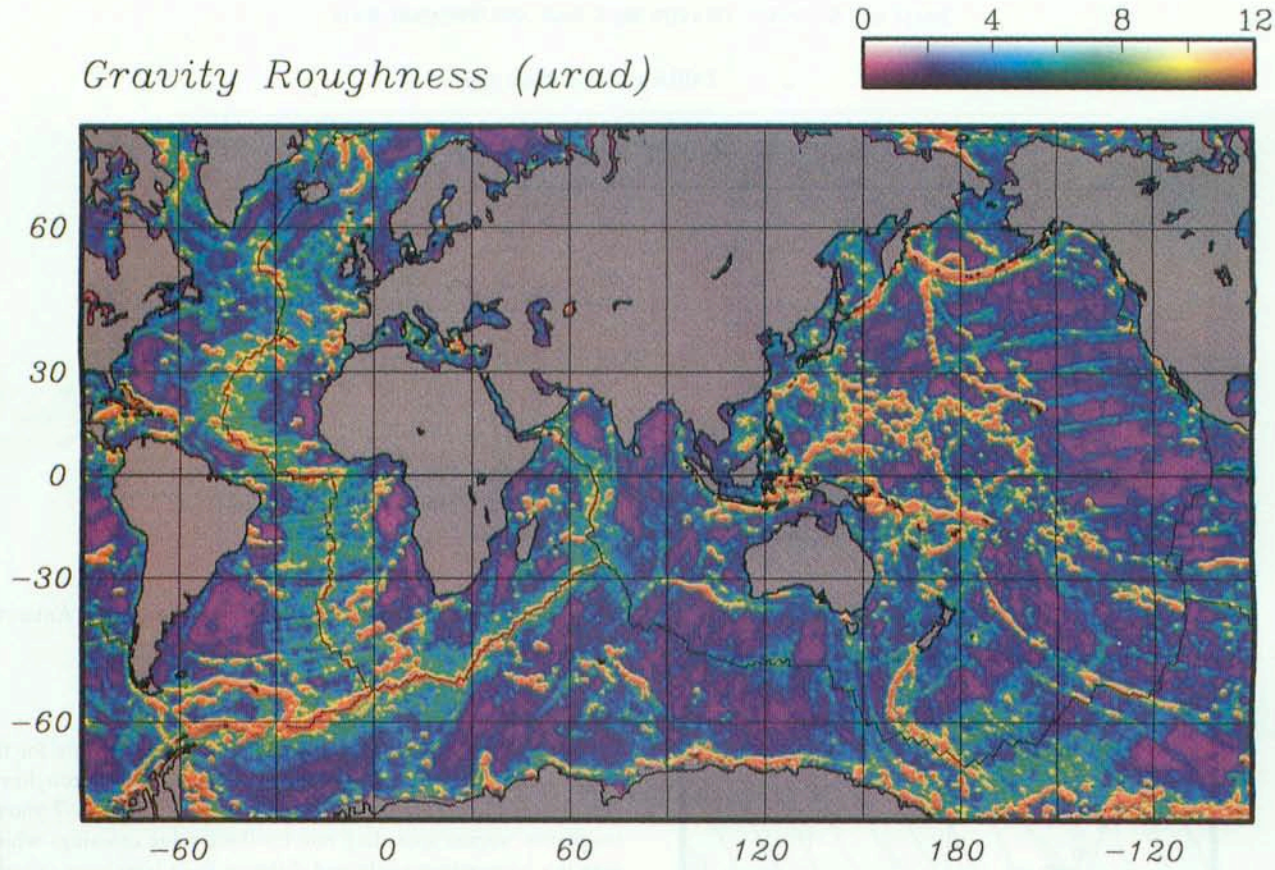

Plate 1. Global gravity roughness map gridded in 0.25° cells. Slower spreading ridges (e.g., Mid-Atlantic Ridge, Southwest Indian Ridge) have high flanking roughness and very high axial roughness. Roughness is low on both the axes and flanks of the fast spreading ridges (e.g., East Pacific Rise, northern Pacific-Antarctic Rise). Note the abrupt transition on the Southeast Indian Ridge and the bands of high roughness on the Pacific-Antarctic Rise flanks.

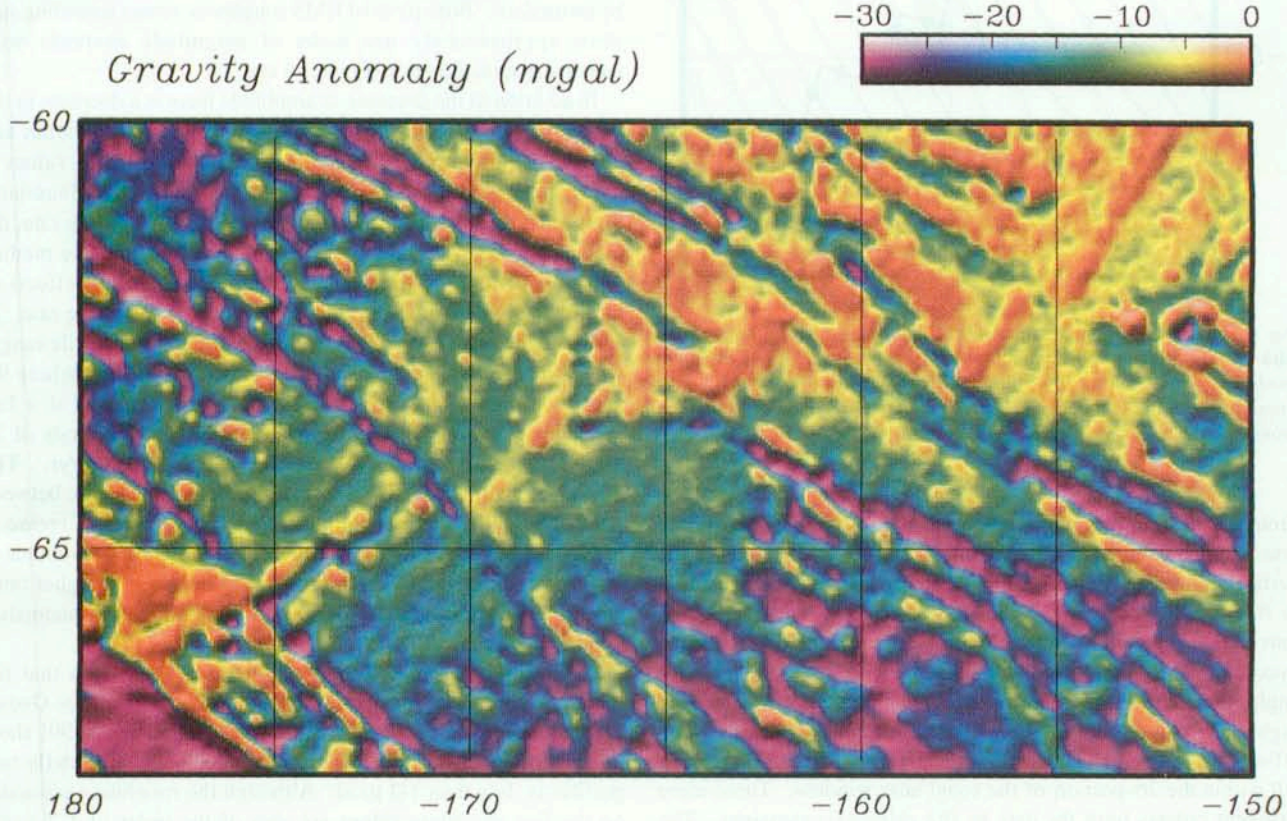

Plate 2. Free air gravity anomalies from closely spaced (~2 km) Geosat altimeter profiles on the Pacific-Antarctic Rise [*Sandwell*, 1991]. The linear anomaly oriented perpendicular to the direction of plate motion near (-65°, 185°) is interpreted as a ridge axis gravity low similar to that observed on slow spreading ridges. The linear high to the northeast (-64°, -162°) is interpreted as an axial high similar to that observed on fast spreading ridges. Note the abrupt decrease in fracture zone anomalies on younger crust near the ridge.

TABLE 1. Global Ridge Axis

Location	Range				References
	Latitude, deg	Longitude, deg	to Latitude, deg	Longitude, deg	
North Central Atlantic	50.06	331.00	15.26	314.88	*Klitgord and Schouten* [1986]
Equatorial Atlantic	15.26	314.88	5.65	327.03	*Cande et al.* [1988]
Equatorial Atlantic	5.65	327.03	0.30	343.50	*Roest* [1987]
Equatorial Atlantic	0.30	343.50	-6.02	348.74	GEBCO
South Atlantic	-6.02	348.74	-54.86	359.53	*Cande et al.* [1988]
Southwest Indian	-54.86	359.53	-25.64	69.96	*Royer et al.* [1988]
Central Indian	9.97	56.92	-25.64	69.96	*Royer et al.* [1988]
Southeast Indian	-25.64	69.96	-50.07	120.19	*Royer et al.*]1989]
Pacific-Antarctic	-34.60	249.43	-60.00	207.85	GEBCO
East Pacific Rise	-32.19	247.95	-26.45	247.14	GEBCO
East Pacific Rise	-23.09	245.44	0.44	257.73	*Lonsdale* [1989]
East Pacific Rise	0.44	257.73	2.45	257.39	*Atwater and Severinghaus* [1989]
East Pacific Rise	2.90	258.60	17.77	254.60	*Atwater and Severinghaus* [1989]

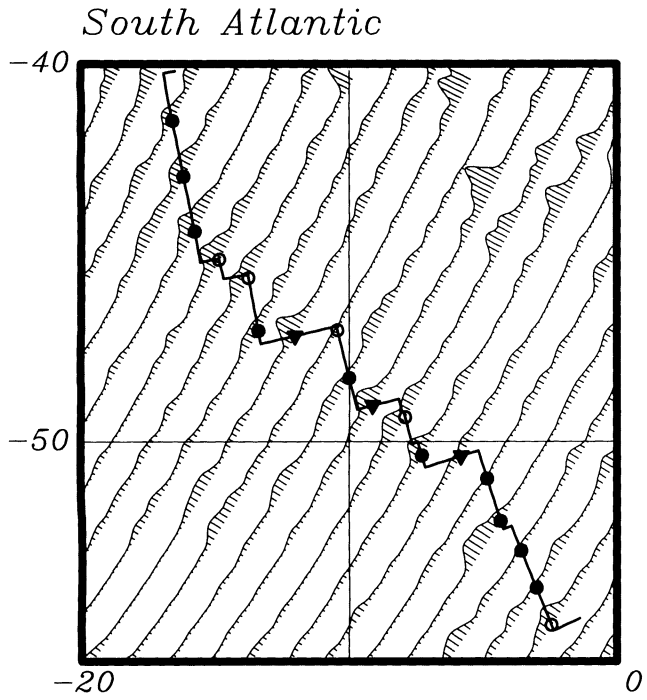

Fig. 4. Example of roughness profiles (20 μrad/deg) across the southern Mid-Atlantic Ridge. Solid symbols show location of roughness estimates used in the study, and open symbols show locations not used because of proximity to ridge-transform intersections. Triangles indicate transform crossings, and circles indicate ridge crossings.

From this data set we flagged all points for which the track azimuth was within 35° of the segment azimuth, since the amplitude of the vertical deflection is greatly diminished for features nearly parallel to the satellite track. When RMS was plotted as a function of intersection angle for all available ridge crossings, we found that the maximum RMS diminished with decreasing intersection angle for angles less than ~30°-35° but showed no azimuthal dependence for higher angles. In order to eliminate the influence of nearby ridge offsets, we flagged all ridge crossings for which an offset crossing fell within the 2σ portion of the roughness window. These more stringent criteria limit the data to 192 ridge axis crossings. The intersection angle criteria limited the number of measurements on the north-south trending EPR and MAR. The density of fracture zones on the MAR further limited the number of points available on this ridge as well as most points in the Australian-Antarctic Discordance Zone.

RESULTS

Plots of the RMS roughness versus full spreading rate for the ridges are shown in Figures 6 and 7. Figure 7 shows roughness versus spreading rate for all ridge crossings. Figure 7 shows roughness versus spreading rate for those ridge crossings which pass the intersection angle and distance from transform criteria. The subdivision of the ridge system discussed above is indicated with different symbols for the Atlantic, Pacific, and Indian ridge systems as well as the smaller ridges and those which are known to be anomalous. Both plots of RMS roughness versus spreading rate show approximately one order of magnitude decrease with increasing spreading rate (Figures 6 and 7).

In addition to the decrease in amplitude there is a decrease in the degree of dispersion with increasing spreading rate. Within any given range of spreading rates, the distribution of RMS values is not symmetric about the mean value (therefore non-Gaussian). Thus to further quantify RMS roughness versus spreading rate, the median was used instead of the mean. The length of the median window (15 mm/yr) was chosen to minimize spurious effects of data gaps and maximize resolution in terms of spreading rate. In addition, the dispersion about the median (i.e., interquartile range) was also calculated. The results are shown in Figure 7 where the median roughness decreases rapidly from 21 μrad at a full spreading rate of 15 mm/yr to a value of 3.0 μrad at a rate of 75 mm/yr then only gradually to 1.8 μrad at 150 mm/yr. The dispersion about the median shows a similar rapid decrease between rates of 15 and 75 mm/yr followed by a more gradual decrease at higher rates. The rapid decrease in ridge axis anomaly amplitude at lower rates followed by the more gradual decrease at higher rates agrees with our earlier study of peak-to-trough ridge axis anomalies [*Small and Sandwell*, 1989].

At the higher spreading rates, there is a suggestion that the minimum roughness may be limited by the accuracy of the Geosat vertical deflection profiles. *Sandwell and McAdoo* [1990] show that in most areas the estimated uncertainty in the vertical deflection profiles is less than 1-2 μrad. Although the roughness estimates on the fast spreading ridges are also of the order of 1-2 μrad, inspection of vertical deflection profiles shows that the ridge axis anomaly is usually distinct from the flanking anomalies [*Small and Sandwell*, 1989]. Furthermore, because the roughness estimate is

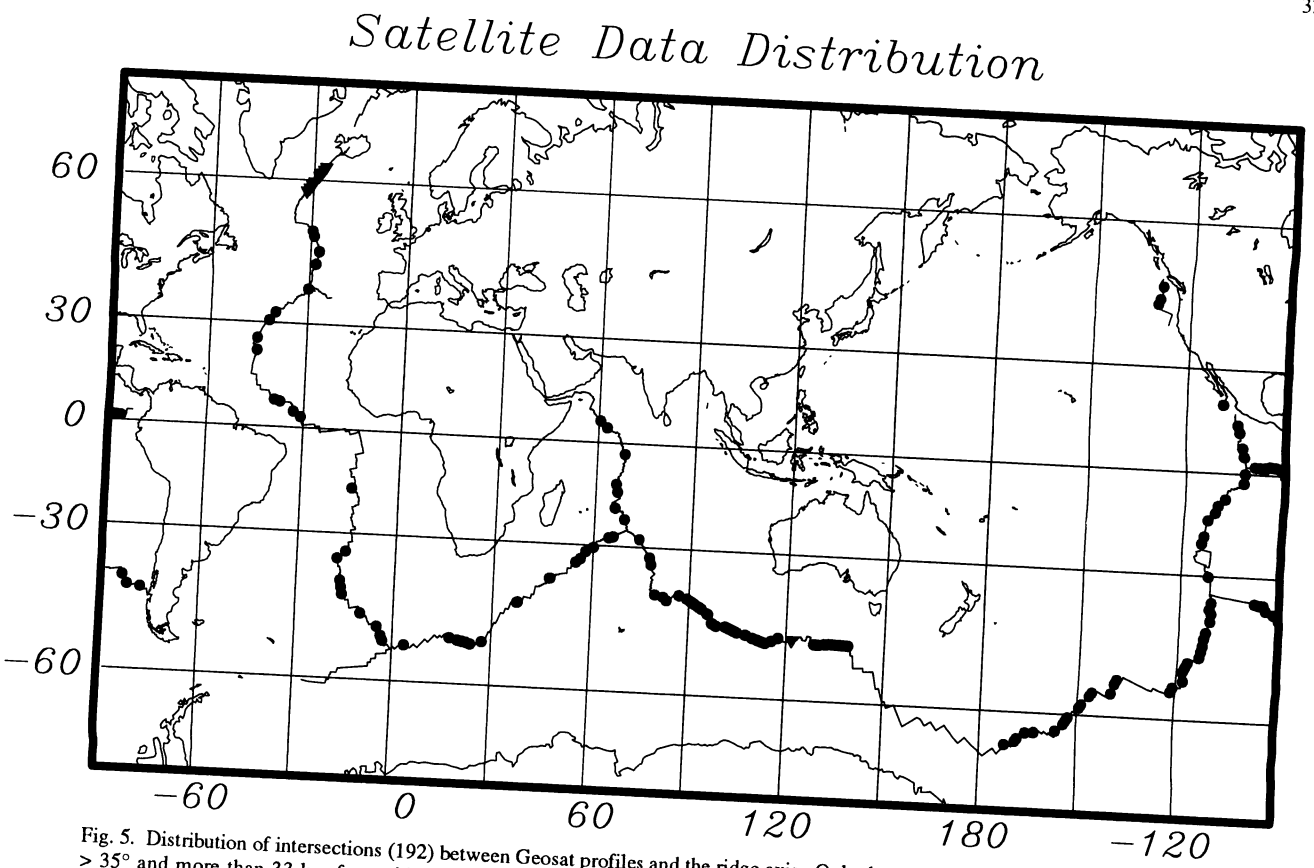

Fig. 5. Distribution of intersections (192) between Geosat profiles and the ridge axis. Only those crossings with intesection angles > 35° and more than 33 km from ridge-transform intersections are plotted. Crossings of anomalous ridges are indicated by triangles. The gap between 140° and ~180° longitude results from exclusion of the poorly mapped Pacific-Antarctic Rise.

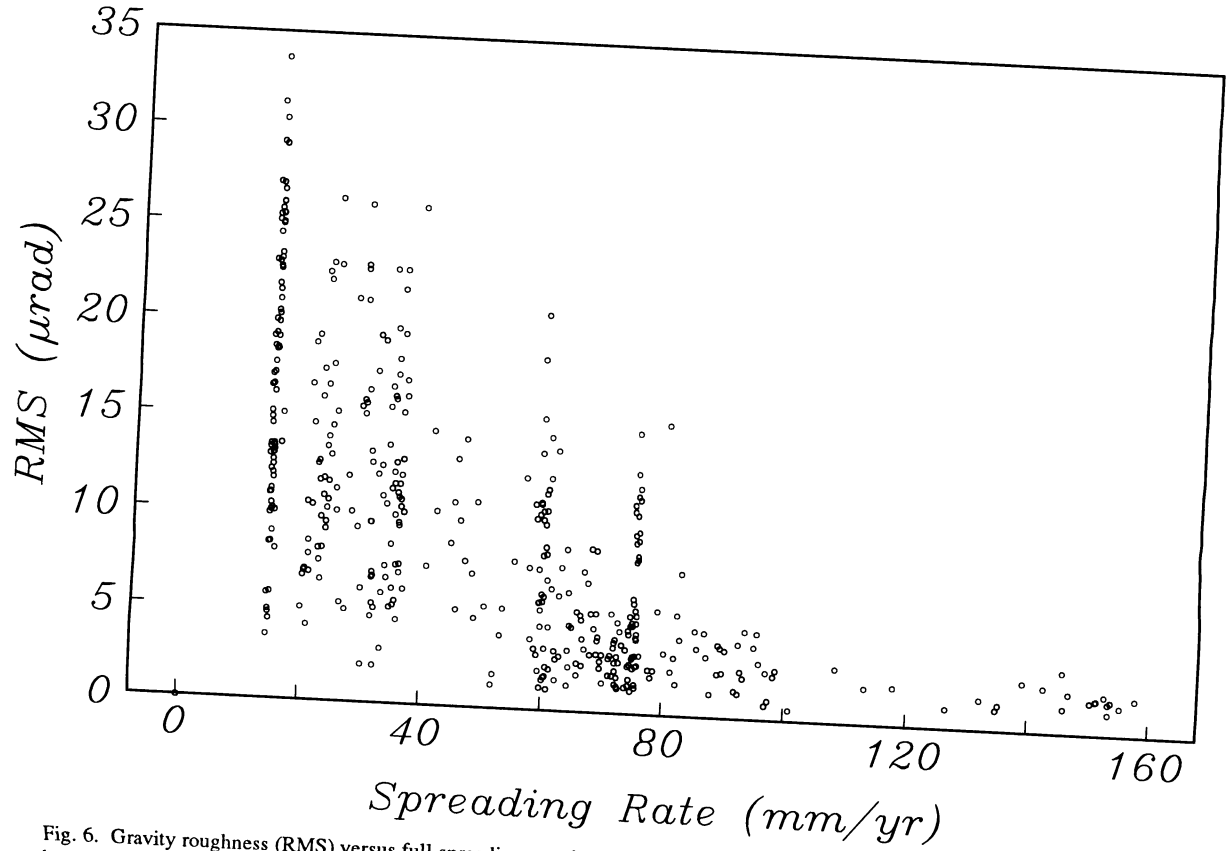

Fig. 6. Gravity roughness (RMS) versus full spreading rate for all ridge crossings. RMS roughness decreases by a factor of 10 between the lowest (16 mm/yr) and highest (155 mm/yr) spreading rates. Beyond 80 mm/yr, roughness is uniformly low.

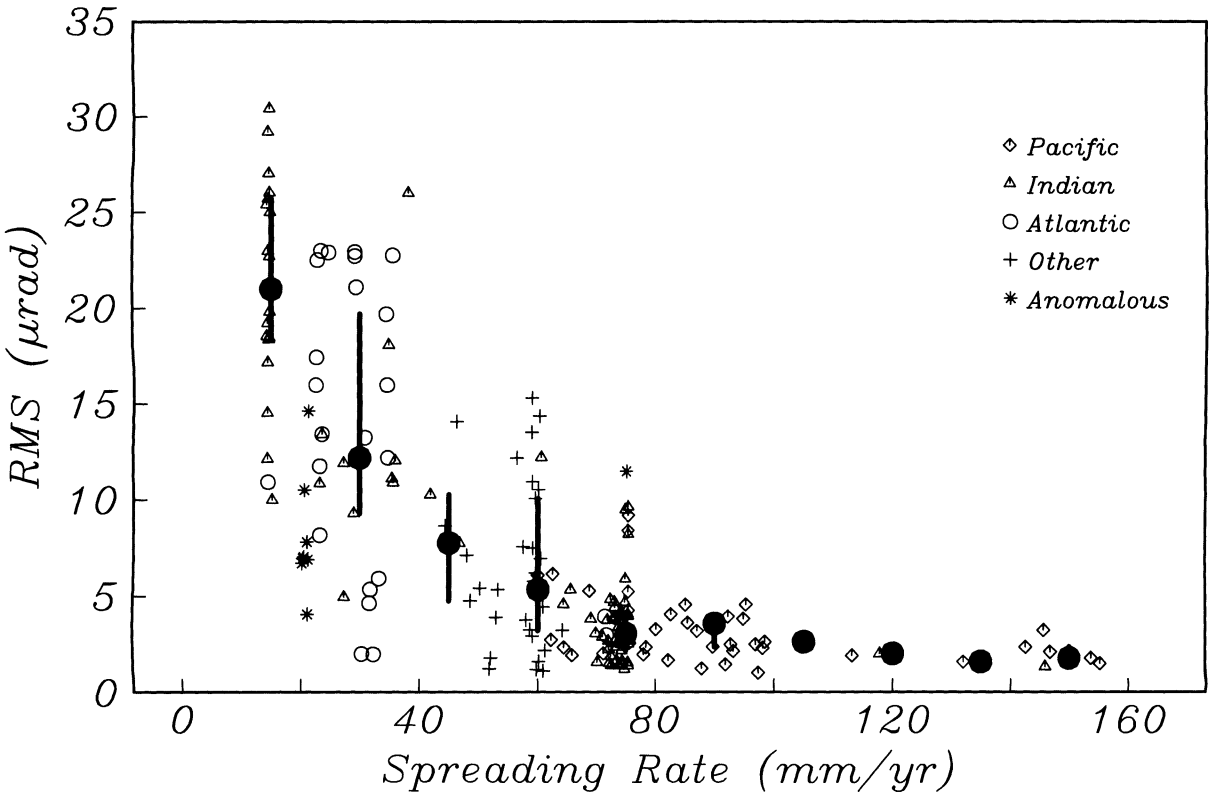

Fig. 7. Gravity roughness versus full spreading rate for ridge crossings > 33 km from a RTI and > 35° intersection angle. Open symbols indicate individual crossings from different ridges. Solid circles indicate median RMS roughness, and vertical bars indicate the interquartile range. A 15 mm/yr window was used. Median RMS roughness decreases from 21 μrad at 15 mm/yr to 5.3 μrad at 60 mm/yr. At higher rates (75-150 mm/yr), the decrease is much more gradual (3.0-1.8 μrad).

an average within the window, roughness values will always underestimate peak values for narrow anomalies. Thus we believe that the 1-2 μrad value at fast spreading ridges reflects the true roughness rather than the limitations of the data

To further investigate the spreading rate transition in ridge axis gravity roughness shown in Figures 6 and 7, we have studied the intermediate rate ridges in more detail. There are five regions of the global mid-ocean ridge system where spreading occurs at intermediate rates. In order to minimize the number of factors influencing the ridge axis dynamics we emphasize those within the continuous ridge system which might be considered "typical". The Chile Rise and the Juan de Fuca Ridge are spreading at intermediate rates, but they are both directly adjacent to active subduction zones and neither is part of the primary ridge system. In addition, the East Pacific Rise spreads at an intermediate rate in the vicinity of the mouth of the Gulf of California, but this area is also adjacent to the edge of an active subduction zone and the recent continental rifting of the Gulf of California. The best examples of intermediate spreading rate ridges are the Southeast Indian Ridge and the Pacific-Antarctic Rise. Unfortunately, both of these ridges lie in relatively unexplored regions of the southern oceans where underway shipboard data are sparse. Since satellite altimetry provides the most complete, consistent coverage available for such remote regions, we have conducted a more detailed study of these ridges with the available altimeter data.

The Southeast Indian Ridge forms part of a continuous segment stretching from the Gulf of Aden through the central Indian Ocean to the Rodriguez Triple Junction and through the southeast Indian Ocean to the Australian-Antarctic Discordance Zone. Along this ridge, spreading rates increase from ~25 mm/yr near the Gulf of Aden to ~45 mm/yr at the Rodriguez Triple Junction to ~70 mm/yr at Amsterdam and St. Paul islands to ~76 mm/yr near the Discordance Zone. Figure 8 shows descending vertical deflection profiles along this section of ridge. Both axial and flanking anomaly amplitudes decrease southeastward along the ridge axis between the Rodriguez Triple Junction and Amsterdam and St. Paul islands. Eastward from Amsterdam and St. Paul, anomaly amplitudes remain low but then increase abruptly near 100°E.

This effect is seen more clearly in Figure 9, where ridge axis gravity roughness is plotted versus longitude along the ridge. There is a rapid, order of magnitude, decrease in roughness between spreading rates of 27 and 69 mm/yr followed by low roughness values at higher rates (70-76 mm/yr) eastward to 100°E, where the roughness again increases. Available bathymetric data also show a transition from an axial valley to an axial high in the vicinity of Amsterdam and St. Paul islands [*Royer*, 1985; *Royer and Schlich*, 1988; R.L. Fisher, personal communication, 1991]. *Small and Sandwell* [1989] also found a transition from an axial low to an axial high in gravity anomlies in this region. It is interesting to note that the roughness increases again near 100°E, although the spreading rate does not change significantly (76 mm/yr). Although it is possible that our ridge axis is mislocated between 110° and 115°, this would not explain the variations in both axial and flanking roughness on adjacent profiles between 100° and 110°E. These observations are consistent with results of a recent study by Cochran [1991] which showed an abrupt change in axial morphology, flanking roughness and magnetic anomaly amplitude near 100°E.

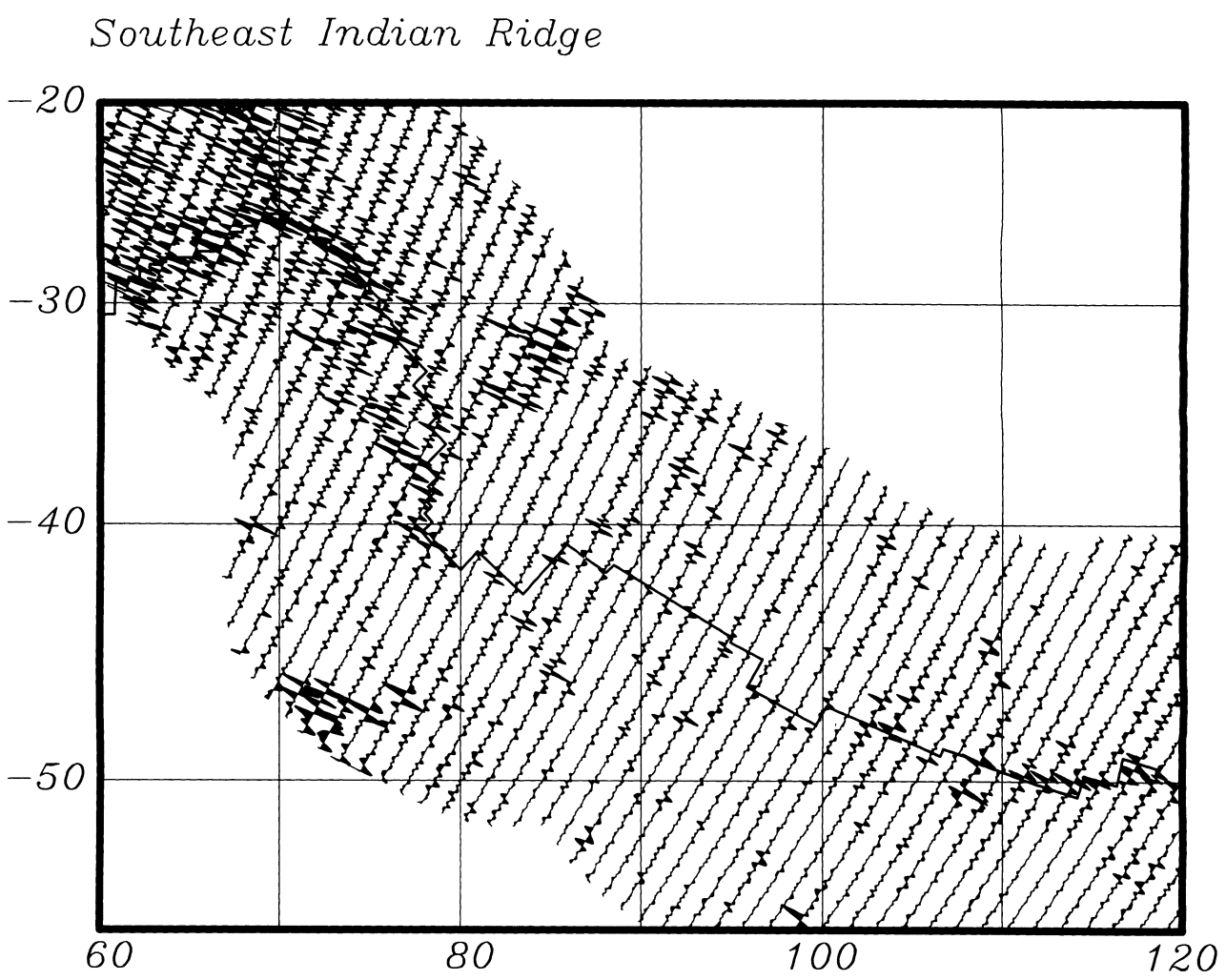

Fig. 8. Descending Geosat vertical deflection profiles along the Southeast Indian Ridge. Vertical deflections within 500 km of the ridge are plotted along satellite tracks at a scale of 20 μrad/deg with positive anomalies filled. The plate boundary is indicated by the thick line. Note the abrupt decrease in amplitude of both axial and flanking anomalies to the east of ~78°E.

The Pacific-Antarctic Rise is a second location along the primary ridge system where spreading occurs at intermediate rates. Recent declassification of data from the Geosat Geodetic Mission (GM) south of 60°S allow a much more detailed view of the gravity field along the Pacific-Antarctic Rise. The dense track spacing of the GM data allows a complete two-dimensional gravity field to be derived from vertical deflection profiles [*Sandwell*, 1991]. Gravity anomalies for this area are shown in Plate 2. While axial gravity roughness in this area does not change drastically, it is apparent from Plate 2 that the character of the axial gravity anomaly does. The westernmost ridge segment (-175° to -170° longitude, 60 mm/yr) clearly shows an axial valley anomaly (i.e., a linear gravity low flanked by highs oriented perpendicular to the fracture zone anomalies). The region to the northeast of this segment (-170° to -164° longitude, 64 mm/yr) shows almost no linear axial anomaly. Finally, the region to the east of -164° (71 mm/yr) clearly shows axial ridge anomalies (i.e., axial highs perpendicular to the fracture zone anomalies). Thus there is a clear transition from axial valley to axial high that occurs over a narrow range of spreading rates (60-71 mm/yr) Although underway data in this area are scarce, available bathymetric profiles confirm this transition from an axial valley to an axial ridge.

DISCUSSION

It is apparent from Figures 6 and 7 that there is a pronounced change in the amplitude and variability of ridge axis gravity anomalies that occurs between spreading rates of ~60 and 80 mm/yr. The distribution of points in the 60-100 mm/yr range of spreading rates is sufficient to demonstrate that this change is real and not a result of poor sampling at intermediate rates. While it may be argued that gravity roughness varies continuously with spreading rate, as has been proposed by *Malinverno* [1991] for ridge flank bathymetry roughness, we feel that the abrupt decrease in amplitude variability and the transition in axial anomaly polarity [*Small and Sandwell*, 1989] indicate an abrupt transition. This interpretation seems to be supported by the spatially abrupt transitions in the three regions discussed above.

This decrease in gravity roughness with increasing spreading rate is also apparent in the global gravity roughness map in Plate 1; slow spreading ridges have large amplitude axial anomalies, while fast spreading ridges have small-amplitude anomalies and the transition between the two is quite abrupt. However, in addition to the change in the ridge axis anomalies, the global roughness map shows that the gravity roughness on the ridge flanks also decreases with

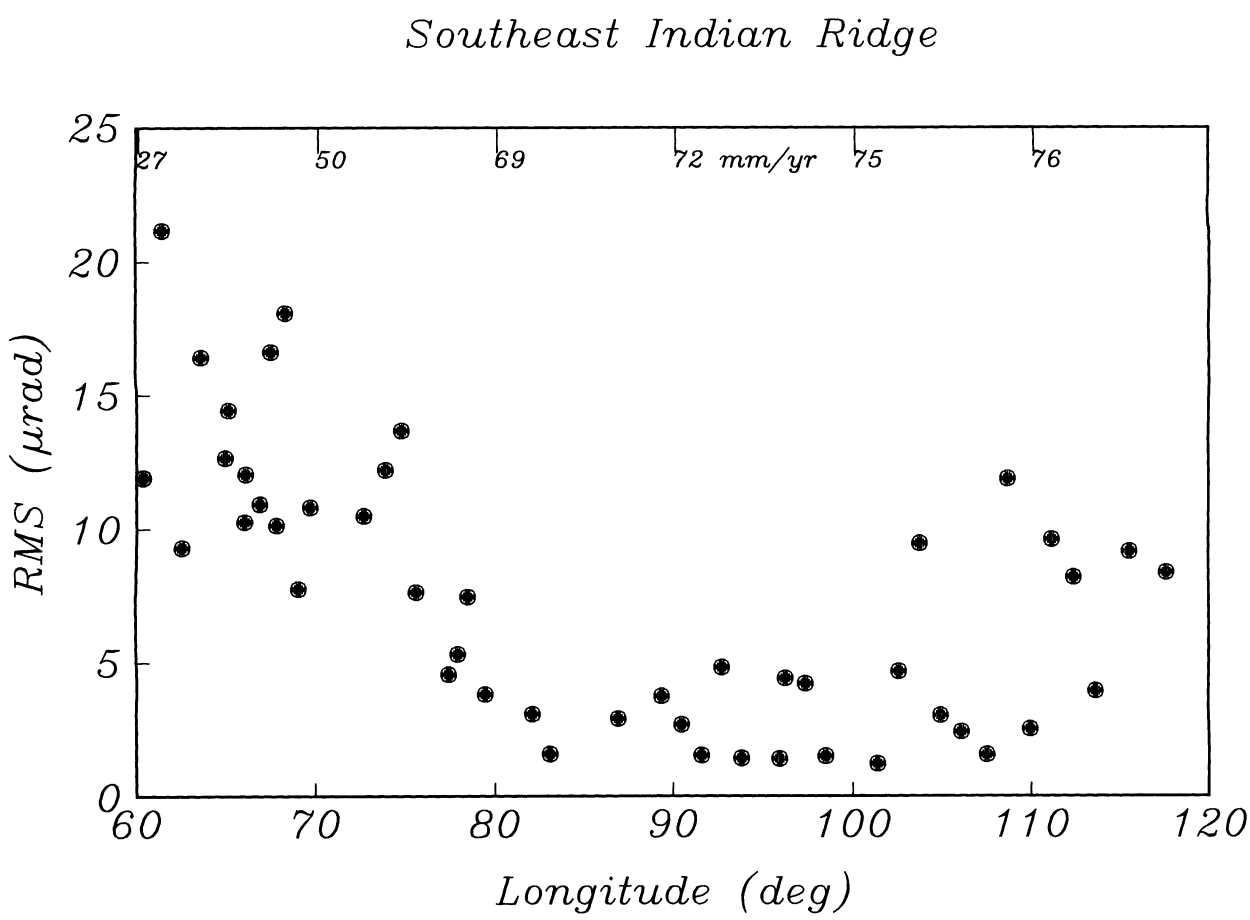

Fig. 9. Gravity roughness (RMS) plotted as a function of longitude for ridge axis anomalies shown in Figure 8. On the western end of the ridge these data show a pattern similar to that of the global data set with a rapid decrease in roughness between rates of 27 and 69 mm/yr followed by uniform roughness at rates greater than ~70 mm/yr. Farther to the east the roughness again increases abruptly near 100°E and varies between 2 and 13 μrad eastward to the Australian-Antarctic Discordance Zone.

increasing spreading rate. This is consistent with the observation that slow spreading ridges have rougher flanking topography than fast spreading ridges [*Menard*, 1967; *Malinverno*, 1991; *Hayes and Kane*, 1991]. The relationship of gravity roughness to topographic roughness on the ridge flanks is more complicated, however, because of sedimentation, changes in water depth and the presence of fracture zones. The relative scarcity of satellite tracks which follow plate motion flowlines would seem to preclude a simple comparison of our ridge flank roughness data with the results obtained by *Malinverno* [1991] for ridge flank bathymetric roughness. While the transition in flanking roughness is probably related to the abrupt transition in axial roughness, an analysis of the flanking roughness is considerably more involved and will be discussed in a separate study.

Although the transition shown in Figure 6 spans the range of spreading rates from ~60 to 80 mm/yr, examination of the regions discussed above indicates that the transition is spatially abrupt within this range of spreading rates. The limited bathymetric data available indicate that these transition zones are accompanied by changes in axial morphology [*Royer*, 1985; *Cochran*, 1991]. This is consistent with the findings of our previous study [*Small and Sandwell*, 1989] in which we found changes in the polarity of axial anomalies in this range of spreading rates.

If the change from variable, high-amplitude gravity anomalies to uniform, low-amplitude axial gravity anomalies reflects a change in the process of crustal accretion, then it is clearly dependent on other factors in addition to spreading rate. Mantle temperature and melt distribution (e.g., crustal thickness) would be expected to exert a strong influence on the axial morphology and compensation mechanism [*Chen and Morgan*, 1990]. This is consistent with our observations. For example, the transition from an axial valley to an axial ridge on the Reykjanes Ridge occurs at a spreading rate of ~20 mm/yr, which is not within the 60-80 mm/yr transition range of the majority of the ridges. Elevated mantle temperatures and excess melt are expected on the Reykjanes Ridge as a result of the proximity of the Iceland hot spot. Likewise, lower temperatures and diminished melting are inferred for the Australian-Antarctic Discordance Zone (~74 mm/yr), where a deep axial valley and large amplitude axial gravity anomalies are present [*Marks et al.*, 1990; *Klein and Langmuir*, 1987; *Christie et al.*, 1988].

The distribution of offsets in the ridge may also affect the axial structure. Along the Reykjanes Ridge, where the axial morphology is more typical of a fast spreading ridge, there is an absence of large transform offsets. Along the Southeast Indian Ridge, the average distance between significant transform offsets increases abruptly near Amsterdam and St. Paul islands where the anomaly amplitude decreases. The axial anomaly amplitude begins to increase toward the discordance zone where the distance between transform offsets begins to decrease. Although the abundance of fracture zones eliminated all but one of our roughness measurements in the

discordance zone, inspection of the vertical deflection profiles indicates a large amplitude anomalies consistent with the deep axial valley which is known to be present. *Cochran* [1991] also finds that transitions in axial morphology and flanking roughness occur across transform offsets in the vicinity of 100°E on the Southeast Indian Ridge. On the Pacific-Antarctic Rise, shown in Plate 2, the gravity anomalies on the ridge flanks seem to show several abandoned fracture zones, possibly indicating a recent change in the plate boundary geometry. If this is the case, then this ridge segment may currently be in the process of changing modes of accretion. If crustal accretion at the ridge axis is controlled by mantle temperature and melt distribution, then transform offsets would effectively segment the ridge thereby controlling the axial structure.

The data presented here seem to indicate that ridge axis structure changes abruptly in certain locations which occur at intermediate spreading rates of ~60-80 mm/yr. Although it is unlikely that spreading rate is the only factor affecting ridge structure, it is certainly an important and possibly dominant control. Without detailed surveys of these transition zones we cannot determine the relative importance of these factors, but it should be apparent that intermediate spreading rate ridges are critical to our understanding of the system as a whole.

Acknowledgments. We thank Karen Marks for suggesting a global gravity roughness study. John Chen, Peter Lonsdale, Dan McKenzie, and Walter Smith also contributed useful comments and suggestions. In addition, we thank Jim Cochran and Marcia McNutt for careful reviews. Chris Small was supported by the NSF Marine Geology and Geophysics Program (OCE89-22751). David Sandwell was supported by Scripps Inststution of Oceanography and NASA Solid Earth Sciences Program (NAG 1266).

REFERENCES

Atwater, T., and J. Severinghaus, *The Geology of North America*, vol. N, *Tectonic Maps of the Northeast Pacific*, Geological Society of America, Boulder, Colo., 1989.

Brown, R.D., W.D. Kohn, D.C. McAdoo, and W.E. Himwich, Roughness of the marine geoid from Seasat altimetry, *J. Geophys. Res.*, *88*, 1531-1540, 1983.

Canadian Hydrographic Service, General bathymetric map of the oceans (GEBCO), scale 1:10,000,000, Ottawa, Ont., 1982.

Cande, S., J. L. LaBrecque, and W.B. Haxby, Plate kinematics of the South Atlantic: Chron 34 to present, *J. Geophys. Res.*, *93*, 13,479-13,492, 1988.

Chen, Y., and W.J. Morgan, A nonlinear rheology model for mid-ocean ridge topography, *J. Geophys. Res.*, *95*, 17,583-17,604, 1990.

Christie, D.M., D. Pyle, J.-C. Sempere, J.P. Morgan, and A Shor, Petrologic and tectonic observations in and adjacent to the Australian-Antarctic Discordance, *Eos Trans. AGU, 69*, 1426, 1988.

Cochran, J.R., An analysis of isostasy in the world's oceans, 2, Mid-ocean ridge crests, *J. Geophys. Res.*, *84*, 4713-4729, 1979.

Cochran, J.R., Systematic variation of axial morphology along the Southeast Indian Ridge, *Eos Trans. AGU*, *72*, 260, 1991.

DeMets, C.,R.G. Gordon, D.F. Argus, and S. Stein, Current plate motions, *Geophys. J. Int.*, *101*, 425-478, 1990.

Gilbert, D., V. Courtillot, and J.L. Olivet, Seasat altimetry and the South Atlantic geoid 2, Short-wavelength undulations, *J. Geophys. Res.*, *94*, 5545-5559, 1989.

Hayes, D.E., and K.A. Kane, The dependence of seafloor roughness on spreading rate, *Geophys. Res. Lett.*, *18*, 1425-1428, 1991.

Klein, E.M., and C.H. Langmuir, Global correlations of oceanic ridge basalt chemistry with axial depth and crustal thickness, *J. Geophys. Res.*, *92*, 8089-8115, 1987.

Klitgord, K.D., and H. Schouten, Plate kinematics of the central Atlantic, in *The Geology of North America*, vol. M, *The Western North Atlantic Region*, edited by P.R. Vogt and B.E. Tucholke, pp. 351-378, Geological Society of America, Boulder, Colo., 1986

Lonsdale, P., Segmentation of the Pacific-Nazca Spreading Center, 1°N-20°S, *J. Geophys. Res.*, *94*, 12,197-12,225, 1989.

Macdonald, K.C., The crest of the Mid-Atlantic Ridge: Models for crustal generation and tectonics, in *The Geology of North America*, vol. M, *The Western North Atlantic Region*, edited by P.R. Vogt and B.E. Tucholke, pp. 51-68, Geological Society of America, Boulder, Colo., 1986.

Malinverno, A., Inverse square-root dependence of mid-ocean ridge flank roughness on spreading rate, *Nature*, *352*, 58-60, 1991.

Mandelbrot, B., *The Fractal Geometry of Nature*, 460 pp. W.H. Freeman, San Francisco, New York, 1982.

Marks, K.M., and R.V. Sailor, Comparison of GEOS 3 and Seasat altimeter resolution capabilities, *Geophys. Res. Lett.*, *7*, 193-196, 1980.

Marks, K.M., P.R. Vogt , and S.A. Hall, Residual depth anomalies and the origin of the Australian-Antarctic discordance zone., *J. Geophys. Res.*, *95*, 17,325-17,337, 1990.

McNutt, M., Compensation of ocean topography: An application of the response funciton technique to the *Surveyor* area, *J. Geophys. Res.* , *84*, 7589-7598, 1979.

Menard, H.W., Seafloor spreading, topography and the second layer, *Science*, *157*, 923-924, 1967.

Roest, W.R., Seafloor spreading patterns of the North Atantic between 10° and 40°N, *Geol. Ultraiectina*, *48*, 121 pp., 1987.

Royer, J.-Y., Evolution cinematique detaillee de la dorsale est-indienne entre le point triple de Rodriguez et les iles Amsterdam et Saint Paul pendant les 20 demiers millions d'annees, these de doctorat, 213 pp., Univ. Louis Pasteur, Strasbourg, France, 1985.

Royer, J.-Y., P. Patriat, H.W. Bergh, and C.R. Scotese, Evolution of the Southwest Indian Ridge from the Late Cretaceous (anomaly 34) to the middle Eocene (anomaly 20), *Tectonophysics*, *155*, 235-260, 1988.

Royer, J.-Y., and R. Schlich, Southeast Indian Ridge between the Rodriguez Triple Junction and the Amsterdam and Saint-Paul islands: Detailed kinematics for the past 20 m.y., *J. Geophys. Res.*, *93*, 13,524-13,550, 1988.

Royer, J.-Y., J.G. Sclater, and D.T. Sandwell, A preliminary tectonic fabric chart of the Indian Ocean, *Proc. Indian Acad. Sci.*, *98*, 7-24, 1989.

Sandwell, D.T., and D.C. McAdoo, High-accuracy, high-resolution gravity profiles from 2 years of the Geosat Exact Repeat Mission, *J. Geophys. Res.*, *95*, 3049-3060, 1990.

Sandwell, D.T., Antarctic marine gravity field from high density satellite altimetry, *Geophys. J. Int.*, in press, 1991.

Small, C., and D.T. Sandwell, An abrupt change in ridge axis gravity with spreading rate, *J. Geophys. Res.*, *94*, 17,383-17,392, 1989.

Welch, P.D., The use of the fast Fourier transform for estimation of power spectra: A method based on time averaging over short modified periodograms, *IEEE Trans. Audio Electroacoust.*, *AU15*, 70-73, 1967.

D.T. Sandwell and C. Small, Scripps Institution of Oceanography, Geological Research Division, 9500 Gilman Drive, La Jolla, CA 92093-0220.

(Received March 23, 1991;
Revised September 23, 1991;
accepted September 25, 1991.)

Geophys. J. Int. (1994) **116**, 64–84

A global analysis of mid-ocean ridge axial topography

Christopher Small
Scripps Institution of Oceanography, UCSD, La Jolla, CA 92093-0208, USA

Accepted 1993 June 15. Received 1993 June 10; in original form 1992 August 20

SUMMARY

Current views of mid-ocean ridges are strongly influenced by extensive mapping of the Mid-Atlantic Ridge and East Pacific Rise. The global picture of the mid-ocean ridge system, particularly in the sparsely surveyed Southern Oceans, is still based primarily on underway bathymetry profiles collected over the past 40 years. This study presents a quantitative analysis of global mid-ocean ridge morphology based on 156 of these underway bathymetric profiles, thereby allowing commonly recognized features such as axial valleys and axial ridges to be compared on a global basis. An Empirical Orthogonal Function (EOF) analysis is used to separate deterministic and stochastic components of axial morphology and to quantify the dependence of each on parameters such as spreading rate and axial depth. *It is* found that approximately 50 per cent of the variance in axial morphology may be described as a linear combination of five independent symmetric and anti-symmetric modes; the remainder is considered stochastic. Maximum axial valley relief decreases with spreading rate for rates less than 80 mm yr^{-1} while axial ridge relief remains relatively constant for all rates greater than 50 mm yr^{-1}. The stochastic component of the axial morphology, referred to as bathymetric *roughness*, also decreases with spreading rate for rates less than 80 mm yr^{-1} and remains relatively constant at higher rates. Although both axial valley relief and bathymetric roughness near the ridge axis show a similar spreading rate dependence, they are weakly correlated at slow spreading centres. The distinct differences in morphologic variability of fast and slow spreading ridges may result from the episodicity of magmatic heat input which controls the lithospheric rheology at slow spreading ridges. These observations support the notion of a critical threshold separating two dynamically distinct modes of lithospheric accretion on mid-ocean ridges.

Key words: Mid-Atlantic Ridge, oceanic lithosphere, sea-floor spreading, topography.

INTRODUCTION

It is well known that mid-ocean ridge axial morphology varies with spreading rate. The traditional view of the ridge system states that slow spreading ridges are characterized by a 1–2 km deep axial valley bounded by rift valley mountains and rugged flanking topography, while fast spreading ridges are characterized by a more continuous axial ridge, less than 1 km in height and bounded by smoother flanking topography. Numerous multibeam surveys of the northern Mid-Atlantic Ridge and East Pacific Rise have modified the traditional view of the ridge system. It is now known that both fast and slow spreading ridges are considerably more segmented than was previously believed. In particular, the distinction of smaller scale migrating offsets from the larger scale, more stable transform offsets has been recognized. It has also been shown that axial depth and relief often vary in a consistent manner with distance from different types of offset on both fast and slow spreading ridges.

Although systematic multibeam surveys provide a more complete view of the ridge axis, the majority of the ridge system has been surveyed only with single wide beam echosounders. As mentioned above, the majority of our knowledge of ridge axis morphology is based on multibeam surveys of the northern Mid-Atlantic Ridge and East Pacific Rise. While these ridges provide convenient access to the fast and slow spreading end members of the system, they comprise less than half of the global mid-ocean ridge system. Current knowledge of the ridges in the Southern Oceans is still based almost entirely on expeditions conducted prior to the mid 1970s (Smith 1992). Because very few multibeam surveys have been conducted on the

ridges in the Southern Oceans, most of the available data consist of isolated underway profiles which cross the ridge at random locations and orientations. By considering the large body of underway data presently available, it may be possible to quantify global characteristics of ridge morphology and supplement the information obtained from more detailed regional studies.

Despite the importance of local segmentation that has been recognized in recent years, axial morphology is often considered to be controlled by spreading rate. On a global scale, spreading rate is undisputably the dominant influence although it is certainly not the only factor to affect the morphology. The existence of anomalous ridges such as the Reykjanes Ridge and the Australian–Antarctic Discordant Zone prove that the influence of spreading rate may be overridden by larger scale controls such as mantle flow and thermal structure. Observations from regional surveys indicate that the presence of offsets also exerts a profound influence on ridge morphology although the segmentation is inherently more difficult to quantify than spreading rate. Unlike spreading rate, the detailed segmentation of a ridge is known only after it has been completely surveyed. An additional difficulty arises in that it is not known whether segmentation is controlled primarily by the regional tectonic history of a ridge segment or by the nature of mantle upwelling. Spreading rate may be considered a more absolute control in the sense that both the regional tectonic history and the pattern of upwelling at the ridge crest are affected by large scale divergent plate motions.

The primary objective of this study is to provide a means of quantifying global ridge axis morphology which may be used to constrain models for its origin as well as to understand its relationship to flanking topography. A secondary objective is to distinguish between the variability related to spreading rate and that related to local controls such as segmentation and tectonic history. On a global basis, spreading rate is undoubtedly the most well constrained of these parameters. Simple models of global plate motions provide reasonably accurate estimates of spreading rate over most of the ridge system (Minster & Jordan, 1978; DeMets *et al.* 1990). The segmentation of the ridge system is reasonably well known in many areas but on a global scale it is severely biased by uneven mapping. For this reason it is possible to quantify the dependence of ridge axis morphology on large scale segmentation although unmapped small scale segmentation may exert a larger influence on local morphology. Given the random distribution of underway bathymetry profiles currently available over most of the ridge system, it is not yet possible to accurately relate them to ridge segmentation. For this reason the analysis will focus primarily on spreading rate. It should not be inferred that spreading rate is the only important parameter or even the dominant control on a local scale. It is, however, the only parameter that is accurately known over most of the mid-ocean ridge system. Because of local complexity and the scarcity of data, tectonic history and segmentation will not be considered here.

QUANTITATIVE CHARACTERIZATION OF RIDGE AXIS TOPOGRAPHY

Ridge axis topography may be envisioned as the sum of a regional deterministic component and a local stochastic component. If the stochastic component can be removed then the analysis of the deterministic component is greatly facilitated. It should be pointed out here that 'deterministic' merely refers to a recognizable component of topography such as an axial valley or an axial ridge. Similarly, 'stochastic' is not used in a strict statistical sense but rather refers to a component of topography that varies appreciably from location to location such as seamounts and abyssal hills. For the purposes of this study, axial valleys and ridges are considered deterministic in the sense that they are characteristic of spreading centre morphology and have a relatively consistent form. All other components of ridge axis morphology such as seamounts, abyssal hills and other features, often referred to as bathymetric roughness, are considered to be stochastic. It will be shown that the analysis used in this study provides a natural basis for this distinction. The underlying implication is that the large scale features of a particular ridge axis might ultimately be understood well enough to be explained deterministically whereas the particular pattern of topographic roughness will not.

The preferred method of separating the two components is to construct a forward model of the deterministic component and remove it from the observed data, leaving the residual as the stochastic component. This method, however, presupposes a thorough understanding of the processes responsible for creating the deterministic component and is therefore useful only in studies of the stochastic component. Our current understanding of the processes responsible for the generation of ridge axis morphology preclude such an approach for this study.

A second method of separating the deterministic and stochastic components is on the basis of wavelength discrimination. This method usually assumes that the long wavelength features are the deterministic components while the short wavelength features are stochastic, and reduces the separation to a filtering operation. This is often a valid approach but the use of wavelength alone has two major drawbacks for a study of ridge axis morphology. The primary drawback of this approach is the lack of suitable criteria for determining a cut-off wavelength separating the stochastic from the deterministic component. A second drawback is that merely smoothing ridge axis bathymetry profiles does not provide an objective means of quantifying characteristics such as axial relief or asymmetry.

In this study an Empirical Orthogonal Function (EOF) analysis is used to determine the fundamental modes or spatial characteristics of ridge axis structure and to relate them to spreading rate and depth. As the name implies, an Empirical Orthogonal Function analysis decomposes a 2-D field of data into orthogonal modes or basis functions which span one dimension of the data space while simultaneously providing information about the variation of these modes in the other dimension of the data space. In this study, the data consist of a collection of bathymetric profiles from different locations on the global mid-ocean ridge system. Hence the data field is composed of sea-floor depths which vary as a function of distance (perpendicular to the ridge axis) and spreading rate. This decomposition will find independent spatial modes which best describe the ridge axis morphology and the dependence of these modes on spreading rate and other parameters. By decomposing a 2-D field into empirically determined independent components,

we are also provided with a basis upon which to separate the deterministic (recognizable) from the stochastic (unrecognizable) components of the axial morphology.

EMPIRICAL ORTHOGONAL FUNCTION ANALYSIS

We consider a 2-D field of topography $D(v, x)$ which varies as a function of distance from the ridge axis x and as a function of spreading rate v. Our objective is to factor this field into a product of spatial modes $M(x)$ and rate-dependent coefficients $C(v)$. This may be written as

$$D(v_i, x_j) = \sum_{k=1}^{N} C_k(v_i) M_k(x_j). \quad (1)$$

The function M_k represents a spatial mode and C_k represents the rate-dependent coefficient for that mode. N is defined as Min (m, n) where m is the number of rate increments and n is the number of spatial increments. The problem may be written as a matrix equation and factored using a singular value decomposition as

$$\mathbf{D} = \mathbf{USV}^T \quad (2)$$

where **D** represents the data matrix, **U** and **V** are orthogonal matrices and **S** is a diagonal matrix of singular values. The singular values are the square roots of the eigenvalues of the square symmetric matrix $\mathbf{DD}^T$ and are often referred to as the spectrum of the matrix **D**. The number of non-zero eigenvalues in **S** indicates the rank of the matrix **D** while the matrix **V** consists of a set of orthonormal basis functions (eigenvectors) which span the row space of **D**. The factorization shown in eq. (1) may be obtained from the singular value decomposition in eq. (2) if $\mathbf{C} = \mathbf{US}$ and $\mathbf{M} \equiv \mathbf{V}^T$. Further explanations of the theory are given by Lorenz (1959), Davis (1976), Shaw (1988) and Menke (1989).

The decomposition allows an individual bathymetric profile to be described as a linear combination of independent basis functions or modes as

$$D(x) = c_1 M_1(x) + c_2 M_2(x) + \cdots + c_r M_r(x) + R(x), \quad (3)$$

where $D(x)$ is the bathymetric profile as a function of distance x at a particular spreading rate v; $M_1(x)$, $M_2(x) \cdots M_r(x)$ are the spatial modes; $c_1, c_2 \cdots c_r$ are the individual coefficients for this profile; r is the number of significant modes; and $R(x)$ is the sum of the remaining modes. The number of significant modes may be determined by some *a priori* criterion or by the rank of the matrix **D** as given by the number of non–zero singular values in **S**. In general, the higher order singular values will not be exactly zero but if there is a noticeable distinction between the large and small values then this may provide some basis upon which to separate consistently recognizable components of the topography from those which appear to vary in a random manner. If this is the case, the residual $R(x)$ may be considered the stochastic component or bathymetric roughness.

This decomposition yields three useful pieces of information. The spatial modes provide estimates of the dominant forms of the ridge structure while the coefficients provide an estimate of how the independent modes combine to form the ridge axis morphology. The coefficients also offer an objective measure of how characteristics such as axial valley relief and asymmetry each vary with spreading rate or other parameters. In addition, it is shown by Davis (1976) that each singular value gives the portion of the variance associated with the corresponding mode. If such a distinction can be made between the recognizable and random components of the bathymetry then the normalized singular values provide a quantitative estimate of the partition of variance between the two components.

Although the decomposition given above is not the only possible, it is optimum in the sense that it minimizes the mean square error in the representation of the data field in terms of a limited number of basis functions (Davis 1976). The use of EOFs is somewhat analogous to the filtering approach discussed above but has several advantages. The empirically determined basis functions provide a natural means for quantifying independent components of axial morphology, such as relief and asymmetry, which cannot be easily obtained from the larger number of complex exponentials used as basis functions in the Fourier approach. Also, the spectrum of singular values, or even the modes themselves, may provide some criterion for discriminating between the deterministic and stochastic components of the morphology. These modes may then be examined separately and related to spreading rate or any other parameter. The EOF decomposition is particularly well suited for characterizing ridge axis topography because, unlike the Fourier approach, it makes no assumptions about the statistical stationarity of the input field.

Since the eigenvalue decomposition of a matrix is invariant to row (or column) exchanges, it is not necessary to conduct a separate analysis to investigate the dependence on depth or any other parameter. Each profile has an individual depth z associated with it in the same sense that it has a spreading rate v. For this reason, the same decomposition results, but the $C(z)$ are arranged in a different order from the $C(v)$.

The results presented in this paper are for an EOF decomposition of a global set of 156 bathymetric profiles as summarized in Table 1. In order to eliminate any bias resulting from the directional orientation, each profile was included in both forward and reversed orientation. Since the directional orientation of a profile is only a result of the ship's cruise plan and has no morphologic significance, this eliminates an unnecessary bias in the results. The results are nearly identical to those obtained if each profile is used only once but the resulting modes are purely symmetric and anti-symmetric.

An example of an EOF analysis of a grid of Seabeam bathymetry data collected on the southern Mid-Atlantic ridge is presented in the appendix. The purpose of the Seabeam example is to illustrate the characteristics of the analysis on a data set that may also be interpreted visually. Because adjacent profiles taken from a continuous grid are highly correlated, it is easier to see the relationship between the input data and the results of the analysis. This is intended to give the reader a feel for the analysis which will hopefully make the results of the global analysis easier to interpret. Because there is very little correlation between adjacent profiles in the global data set, it is almost impossible to interpret visually in matrix form and hence is not shown here.

In addition to the Seabeam example, the appendix also

Table 1. Summary of bathymetric profiles.

Profile	Cruise	Year	Lat (deg)	Lon (deg)	Rate (mm/yr)	Ax Depth (m)	RTI Dist. (km)
1	a2936	1976	-25.99	68.92	14	-4760	9.5
2	i1277	1977	-52.86	20.17	14	-3997	102.2
3	brm01	1969	-33.06	56.47	14	-4008	54.6
4	v1605	1959	-33.79	56.11	14	-3790	31.1
5	mmdu1	1973	-37.76	49.78	14	-2800	14.3
6	brm01	1969	-58.88	343.60	17	-4372	26.7
7	e3078	1978	36.63	326.36	21	-2906	12.8
8	ka406	1973	55.07	324.84	21	-2671	12.8
9	v1713	1961	31.93	319.46	22	-3068	12.2
10	ss014	1965	48.80	331.92	23	-3935	23.0
11	inm11	1978	31.47	318.92	23	-3180	33.9
12	ka522	1975	45.75	332.21	23	-3362	233.5
13	v2805	1970	45.24	332.02	23	-3125	289.1
14	ch992	1970	29.54	317.01	23	-3437	66.6
15	ggl94	1983	41.71	330.75	24	-2669	116.8
16	c2115	1978	28.32	316.28	24	-3234	203.5
17	ss007	1965	28.03	316.03	24	-3575	240.5
18	a9321	1977	27.48	316.48	24	-3066	289.0
19	tag71	1971	26.74	315.41	24	-3270	364.1
20	ttagz	1971	26.02	315.14	24	-4487	277.8
21	tag70	1970	25.45	314.67	24	-3623	204.0
22	ss006	1965	24.93	314.46	24	-4105	123.4
23	c3001	1989	22.83	315.01	25	-3796	80.4
24	a2426	1968	19.18	313.94	26	-3352	28.6
25	a2426	1968	19.53	314.06	26	-3217	33.5
26	v2306	1966	17.29	313.60	26	-3826	31.4
27	cag71	1971	14.09	314.96	26	-2907	42.2
28	wi821	1978	7.40	59.71	26	-4033	62.8
29	cag71	1971	14.59	315.01	26	-3565	66.5
30	ch997	1970	6.10	60.87	27	-4034	111.2
31	equ72	1972	11.89	316.24	27	-3674	20.2
32	equ72	1972	11.50	316.31	27	-3968	64.5
33	equ72	1972	10.33	319.06	28	-3991	35.6
34	c1707	1974	3.72	63.79	30	-4198	13.0
35	c1311	1970	1.90	329.35	31	-3023	122.3
36	c1504	1972	-48.30	350.00	33	-3482	104.0
37	v2604	1968	-10.64	346.94	34	-3636	83.7
38	a0681	1972	-12.82	345.41	35	-3865	25.0
39	c1604	1972	-15.24	346.64	35	-2833	48.8
40	a2677	1972	-15.57	346.71	35	-3001	11.2
41	ggl39	1974	-35.69	342.17	35	-4276	5.4
42	mrt13	1985	-33.81	345.45	35	-3991	17.9
43	mrt13	1985	-33.69	345.41	35	-4176	5.2
44	mrt13	1985	-33.33	345.65	35	-3867	20.3
45	mrt13	1985	-32.98	345.55	35	-2502	53.6
46	mrt13	1985	-32.69	345.54	35	-3166	21.2
47	mrt13	1985	-31.98	346.73	35	-3588	7.8
48	mrt13	1985	-31.84	346.65	35	-3157	23.5
49	mrt13	1985	-31.64	346.62	35	-3169	38.4
50	mrt13	1985	-31.51	346.51	35	-3588	22.4
51	mrt13	1985	-31.15	346.56	35	-3319	19.3
52	v1809	1962	-30.49	346.61	35	-2807	12.2
53	a2605	1971	-21.72	348.20	35	-3645	25.4
54	a2605	1971	-21.96	348.21	36	-4278	52.7

Table 1. (*Continued.*)

Profile	Cruise	Year	Lat (deg)	Lon (deg)	Rate (mm/yr)	Ax Depth (m)	RTI Dist. (km)
55	c1402	1971	-15.38	67.23	39	-3565	29.8
56	ant05	1970	-18.97	65.58	41	-2942	120.0
57	dodo8	1964	-21.67	68.89	46	-3235	34.8
58	bnt15	1973	2.28	263.94	48	-2815	53.2
59	gam21	1968	22.41	251.63	51	-2631	62.8
60	gam21	1968	22.19	251.52	51	-3041	89.2
61	gam21	1968	21.99	251.39	52	-2298	115.9
62	gam21	1968	21.77	251.24	52	-2589	144.4
63	inm15	1979	2.21	266.80	53	-2590	124.4
64	gam21	1968	21.51	251.14	54	-2858	172.1
65	gam21	1968	21.28	251.04	55	-2954	145.4
66	gam11	1967	21.04	250.83	56	-2679	111.6
67	gam11	1967	20.86	250.79	56	-2630	90.3
68	a2936	1976	-26.24	71.48	58	-3777	1.2
69	iido4	1971	42.53	233.15	58	-3590	37.1
70	a2936	1976	-26.46	71.87	58	-3766	77.8
71	pp008	1970	-37.75	265.98	59	-3440	80.0
72	sot02	1972	-40.23	268.44	59	-3711	100.0
73	eel14	1964	-40.67	268.07	59	-3278	59.6
74	eel25	1966	-42.78	276.42	60	-3629	26.5
75	eel19	1965	-43.33	277.30	60	-3608	31.6
76	eel25	1966	-44.62	277.83	60	-3826	48.3
77	v2903	1972	-28.03	74.19	60	-3749	36.4
78	eel33	1968	-63.78	191.64	62	-2100	86.2
79	eel42	1970	-62.94	196.03	64	-2228	24.8
80	aan2	1971	-62.47	158.38	68	-1720	63.0
81	eel27	1966	-62.46	157.86	68	-2310	58.0
82	ggal1	1968	-41.01	78.83	68	-2801	21.0
83	c1105	1967	-41.36	81.22	69	-2811	34.1
84	eel54	1972	-41.94	87.80	71	-2369	25.5
85	eel49	1971	-42.52	90.08	71	-2497	155.4
86	eel47	1971	-43.60	92.39	72	-2740	229.7
87	eel46	1970	-43.92	93.42	72	-2738	149.4
88	v1608	1960	-50.16	138.37	72	-2735	87.9
89	ee41a	1970	-50.25	137.51	73	-2540	148.3
90	eel39	1969	-50.34	133.91	73	-2795	91.0
91	eel41	1969	-50.22	132.18	73	-2891	37.6
92	eel54	1972	-46.82	96.55	74	-2490	64.9
93	inm05	1978	-49.06	105.39	74	-3397	81.4
94	eel45	1970	-49.42	109.04	75	-3492	60.9
95	ggl28	1972	-50.04	111.85	75	-3284	177.1
96	v1609	1960	-58.50	211.17	75	-2955	125.3
97	dpsn2	1976	16.43	254.64	80	-2815	67.7
98	lk7112	1972	15.78	254.58	81	-2283	73.8
99	eel23	1966	-54.41	221.60	82	-2064	99.4
100	eel33	1968	-55.13	238.90	85	-2430	0.1
101	c1212	1968	-54.39	241.59	86	-2451	17.0
102	eel43	1970	-53.61	241.98	87	-2379	0.1
103	scn10	1969	14.16	255.62	88	-2571	131.0
104	eel19	1965	-51.60	241.98	89	-2426	152.9
105	sot02	1972	-51.17	242.26	89	-2871	212.3
106	eel25	1966	-50.10	242.97	90	-2229	88.7
107	c1011	1966	12.98	255.98	90	-2638	251.0
108	c1307	1970	12.84	256.06	91	-2815	275.9

Table 1. (*Continued.*)

Profile	Cruise	Year	Lat (deg)	Lon (deg)	Rate (mm/yr)	Ax Depth (m)	RTI Dist. (km)
109	yq69a	1969	12.79	255.71	91	-2889	281.7
110	ggl16	1971	11.92	256.24	92	-2797	204.3
111	sot02	1972	-49.24	246.37	93	-2341	58.8
112	eel20	1965	-47.62	246.75	93	-2895	247.2
113	eel20	1965	-44.49	247.83	95	-2772	597.4
114	eel28	1967	-43.24	248.31	95	-2446	734.7
115	eel21	1965	-39.98	248.20	97	-2351	397.0
116	pp008	1970	-38.01	249.06	97	-2215	176.0
117	dpsn2	1976	11.13	256.28	100	-2574	104.6
118	kk063	1980	11.08	256.29	100	-2565	108.7
119	papa1	1965	9.24	255.78	107	-2595	87.4
120	kk030	1974	6.80	257.36	114	-2743	179.5
121	lus10	1963	5.63	257.55	115	-2706	309.5
122	p7101	1971	5.39	257.57	115	-2738	336.0
123	eel24	1966	-35.62	249.08	116	-2772	69.0
124	c1004	1966	3.16	257.80	118	-2925	171.3
125	scan9	1969	3.10	257.79	118	-2868	168.7
126	ggl09	1969	2.94	257.71	119	-3193	151.5
127	v2403	1967	1.47	258.01	129	-3267	10.1
128	plds3	1976	1.01	257.80	129	-2999	62.3
129	kk901	1974	0.53	257.78	130	-2904	117.5
130	kk025	1974	0.20	257.72	130	-2868	155.3
131	kk025	1974	0.05	257.67	130	-2841	172.0
132	kn734	1978	-1.03	257.52	131	-2940	203.3
133	c1307	1970	-1.42	257.51	131	-2971	159.8
134	pp304	1973	-7.11	252.35	141	-2809	227.9
135	pp304	1973	-7.83	252.14	141	-2752	185.8
136	pp304	1973	-8.30	252.04	142	-2765	129.5
137	we772	1977	-9.11	251.98	142	-2901	37.2
138	cchb1	1971	-11.87	249.26	146	-2592	192.9
139	ggl34	1973	-13.88	247.10	150	-2953	64.3
140	kk723	1973	-13.99	247.50	150	-2678	76.2
141	p7302	1973	-15.99	246.79	150	-3059	303.4
142	ggl92	1983	-16.63	246.94	151	-2637	395.5
143	c1306	1970	-17.02	246.90	151	-2650	420.5
144	c1306	1970	-17.17	246.83	151	-2697	435.9
145	c1306	1970	-17.41	246.83	151	-2675	463.8
146	c1306	1970	-17.59	246.75	151	-2676	483.6
147	c1306	1970	-17.84	246.72	151	-2685	512.7
148	c1306	1970	-17.98	246.44	151	-2449	528.1
149	c1306	1970	-18.19	246.41	151	-2613	551.9
150	c1306	1970	-18.41	246.62	151	-2620	538.5
151	c1714	1974	-21.14	245.76	152	-2808	229.8
152	yq734	1973	-31.28	248.99	155	-2404	34.9
153	yq734	1973	-31.16	248.09	156	-2340	19.9
154	yq734	1973	-31.02	248.12	157	-2403	6.5
155	eel29	1967	-28.28	247.11	157	-2201	44.8
156	p7303	1973	-30.48	247.94	157	-1939	7.2

contains several examples of the robustness of the EOF analysis of the global data. Specifically, it is shown that the analysis gives virtually identical results for distinct (non-intersecting) subsets of the data and is robust to significant variations in profile length. It is also shown that conducting separate analyses for fast and slow spreading ridges gives somewhat different results, both of which are consistent with a single analysis of the entire data set.

DATA

The data used in this study consist of 156 underway bathymetric profiles from various locations on the global mid-ocean ridge system. The locations of these profies are shown in Fig. 1. The profiles were selected on the basis of sampling rate, orientation with respect to the ridge axis and overall data quality. Profiles were rejected if their mean sample spacing was greater than 2 km or if the mean azimuth crossed the ridge axis at an angle less than 45°. Additional profiles were eliminated if they crossed the axis too close to a ridge transform intersection in a poorly surveyed area. Although this may result in elimination of usable data, it minimizes the possibility of contaminating the input data field with transform topography. In heavily surveyed areas only profiles that had the highest sample rate and were most nearly perpendicular to the ridge axis were used. The majority of the profiles on the Juan de Fuca ridge were eliminated because heavy sedimentation on the ridge flanks obscured the basement topography.

The ridge axis on each profile was determined by a two-step procedure. Initial estimates of the location of the ridge axis were defined as the intersection of the profile with the digitized ridge axis used by Small & Sandwell (1992). After finding the approximate location of the ridge axis, the actual location was selected visually using either magnetic anomaly profiles or the axis of symmetry of the bathymetric profile. In most cases this resulted in an adjustment of less than 10 km and in no case more than 40 km. On profiles with a wide central anomaly where there was not a clear axis of symmetry the local depth minimum or maximum was used, depending on the morphology.

Once the profiles and axis crossings were selected, each was projected perpendicular to the ridge axis and interpolated at a 1 km sample interval using an Akima spline (Akima 1970). As mentioned above, profiles were chosen to be nearly perpendicular and profiles more than 20° from normal were used only when there were no others available in the vicinity (33 of 156 profiles). A common length of 80 km was chosen for this analysis on the basis of a visual inspection of the profiles and the results of Le Douaran & Francheteau (1981) and Malinverno (1990). Using a significantly longer cut-off distance substantially decreases the number of profiles available for analysis by eliminating those which change heading or make a series of short passes across the ridge. Using significantly shorter profiles does not adequately represent some of the wider axial valleys on slow spreading ridges. As shown in the appendix, the resulting decomposition is extremely robust to moderate changes in profile length. In addition to drastically reducing the number of profiles available for analysis, a large increase in the profile length would change the emphasis of the analysis. At greater length scales, on the order of hundreds of kilometres, the axial topography becomes insignificant in comparison to the thermal subsidence component of the flanking topography. An investigation of the thermal subsidence characteristics of oceanic lithosphere is beyond

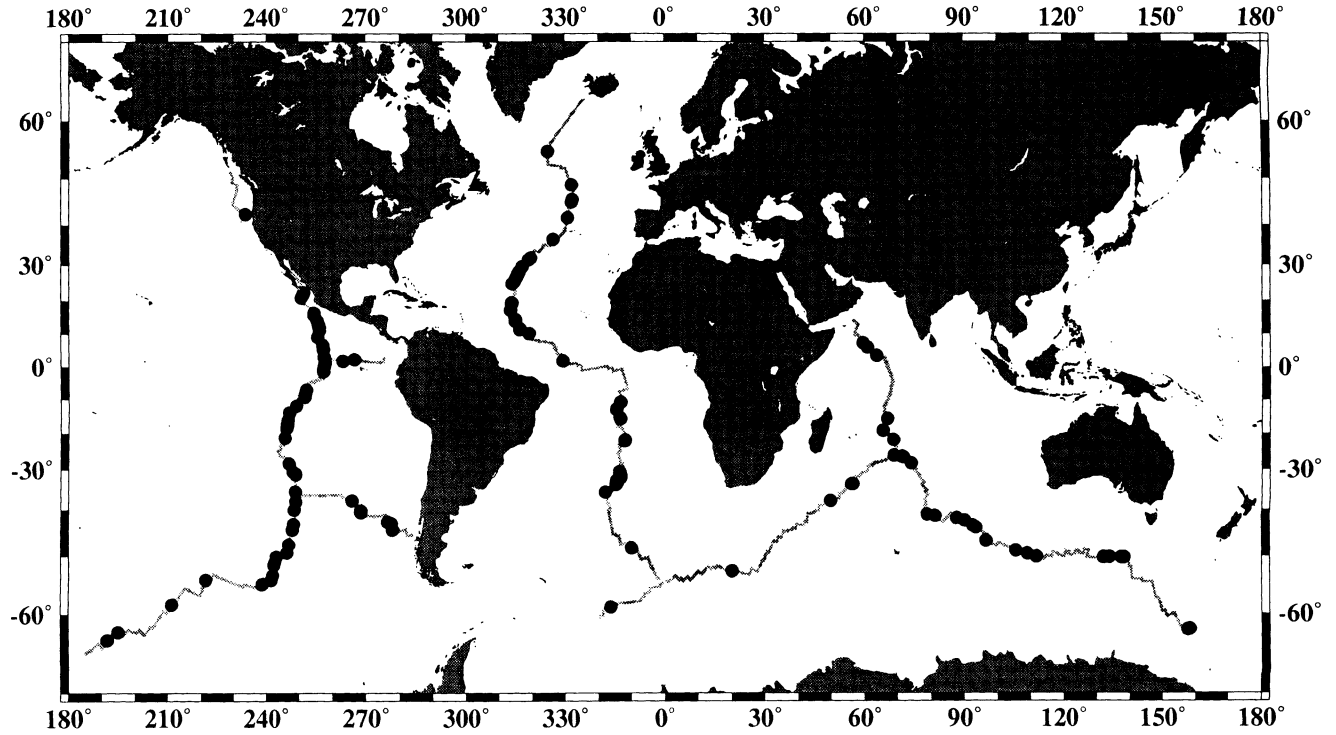

Figure 1. The global distribution of the 156 profiles used in this study. Circles indicate the approximate location of the intersections with the ridge axis. The scarcity of profiles on the Central and South-west Indian Ridges results from sparse data coverage and the abundance of poorly constrained fracture zones.

the scope of this paper and would probably not be well suited to this type of analysis given our current understanding of thermal boundary layer theory.

Spreading rates were computed using the NUVEL 1 plate motion model for all profiles except those on the Pacific–Rivera Rise. Pacific–Rivera spreading rates were taken from DeMets & Stein (1990). Although the NUVEL 1 spreading rates may differ slightly from individual rates computed using marine magnetic anomalies, the difference is not expected to be significant given the local variability of morphology on most ridge segments.

RESULTS

The spectrum of normalized singular values $S(j)$ shown in Fig. 2 indicates that 46 per cent of the topographic signal seen at the ridge axis may be represented in terms of the first five modes. These modes $M(x)$ are shown in Fig. 3 along with their corresponding coefficients $C(v)$. The two primary modes, $M1$ and $M2$, are both symmetric and account for 28 per cent of the topography. The three smaller modes, $M3$, $M4$ and $M5$, account for an additional 18 per cent of the topography. As is typical of eigenvalue decompositions, the higher order modes become increasingly wigglier and do not resemble any recognizable form of ridge axis topography. This partition is also indicated by a distinct break between the first five singular values and the continuum of higher order singular values.

The coefficients $C(v)$ for each mode are also shown in Fig. 3. Since relief is usually defined as the vertical distance between the extremes, each coefficient is multiplied by the range of the corresponding mode to give relief of that mode in metres for each profile. Each of the first five modes shows a consistent decrease in maximum amplitude with spreading rate for slower rates and remains relatively constant at higher rates. It should be noted that all modes have some low amplitude coefficients at slow spreading rates.

It can be seen that each of the primary modes represents a recognizable component of mid-ocean ridge

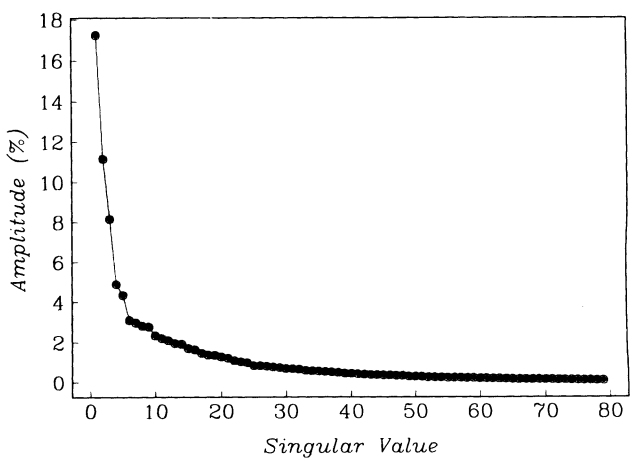

Figure 2. The spectrum of singular values for the global data set. The amplitude of the singular value indicates the percentage of variance accounted for by the corresponding mode in the decomposition. It can be seen that 46 per cent of the variance in this data set may be described by the first five modes. The higher order modes are considered the stochastic component of the topography.

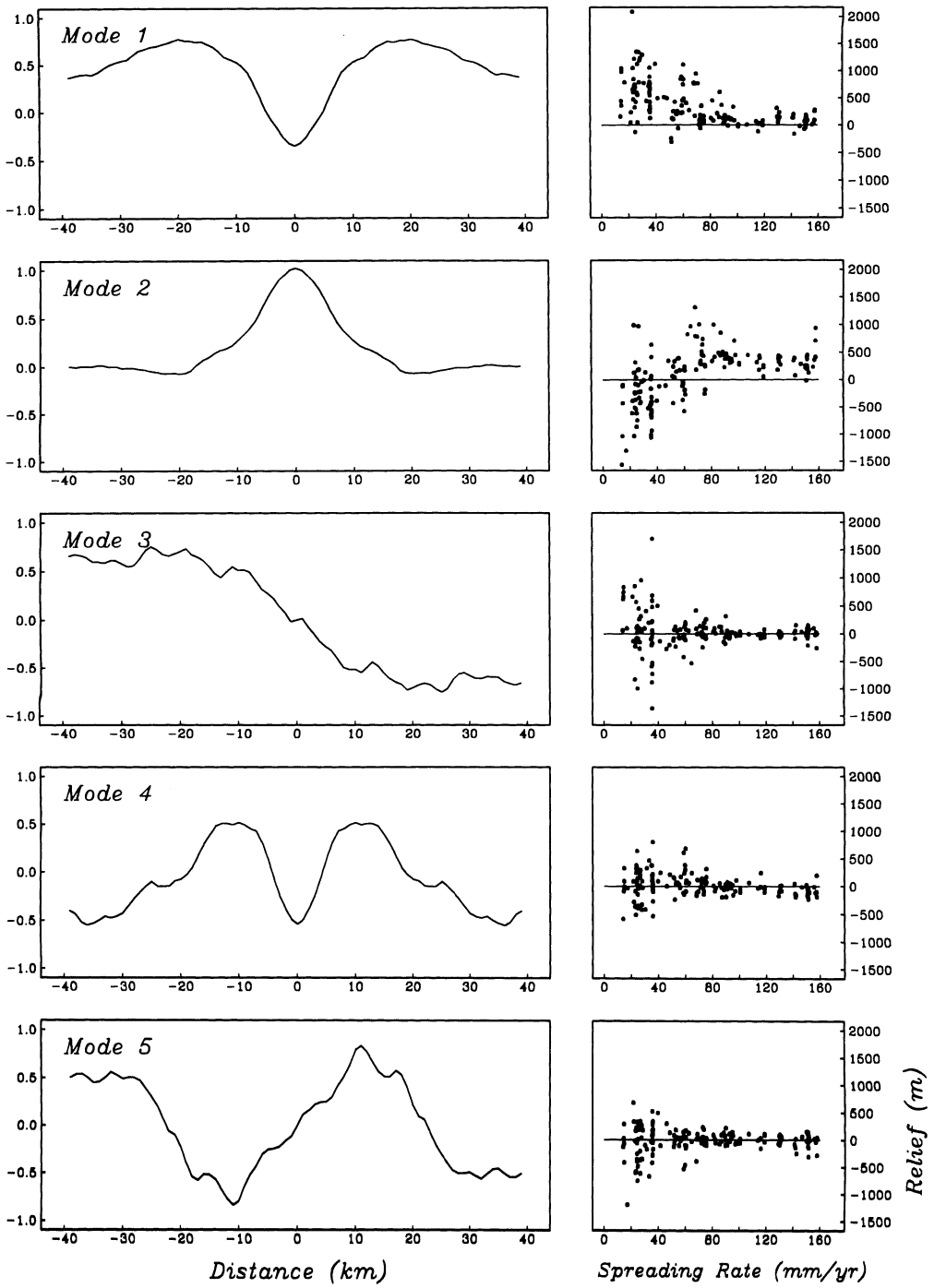

Figure 3. The five significant modes, $M(x)$, and their corresponding coefficients, $C(v)$. Each mode represents a recognizable component of mid-ocean ridge morphology. Modes 1, 2 and 4 are approximately symmetric while modes 3 and 5 are anti-symmetric. The coefficients of all modes are highly variable for spreading rates less than ~90 mm yr^{-1} and relatively constant at higher rates.

axial topography. Mode 1 resembles a slow spreading ridge axis in cross-section although it is primarily positive in value and as such may represent the uplifted flanks usually seen on slow spreading ridges. Mode 2 could resemble an enlarged fast spreading ridge or an inverted slow spreading ridge with negative values at the axis which may correspond to an axial valley. This accounts for the transition from negative to positive coefficients shown by $C2$ in Fig. 3. Mode 3 represents a monoclinal anti-symmetric component which may also be inverted by negative values of $C3$. Modes 4 and 5 also represent symmetric ($M4$) and anti-symmetric ($M5$) components although their importance is significantly less than the three primary components. Mode 4 represents a steeper sided, narrower axial valley structure which controls the width of the axial valley when combined with modes 1 and 2. Mode 5 represents a narrower

anti-symmetric component which controls the asymmetry of the axial valley walls.

The symmetric and anti-symmetric modes may be summed to give the symmetric and asymmetric components of the axial topography. The measured values of the total, symmetric and asymmetric relief are defined as the range of the corresponding linear combinations of the modes given by the EOF decomposition (Fig. 4). Axial valleys are denoted by negative relief and axial ridges by positive relief. For slow spreading ridges there is a large degree of variability but the maximum axial valley depth decreases with increasing spreading rate. A graphic example of this variability is provided by the ridge segment shown by the Seabeam data in the appendix. Axial ridge height on fast spreading ridges remains relatively constant at <500 m. The transition between axial ridge and axial valley topography occurs between ~50 and 80 mm yr^{-1}. Fig. 4(b) shows the absolute range of the sum of the two anti-symmetric modes. Asymmetry is seen to decrease markedly for spreading rates greater than 40 mm yr^{-1} while ranging between 100 and 1800 m for lower rates. These results are consistent with those of Severinghaus & Macdonald (1988) for ridge transform intersections on the Mid-Atlantic Ridge and East Pacific Rise.

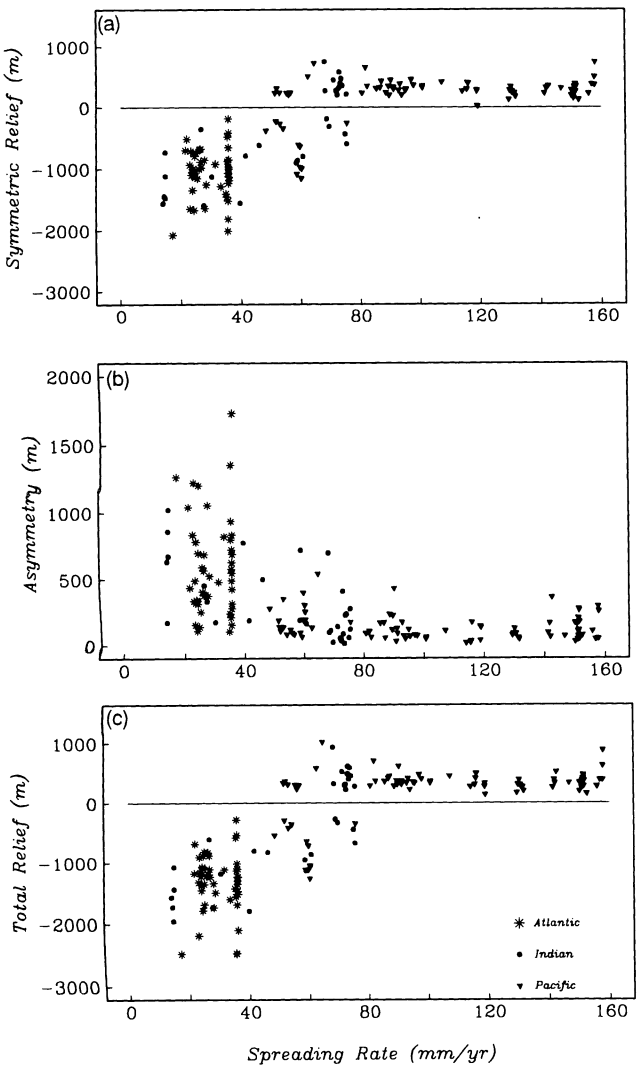

Figure 4. Axial relief versus spreading rate for the global data set. Negative relief indicates an axial valley while positive relief indicates an axial ridge. (a) Symmetric relief is a sum of coefficients for modes 1, 2 and 4. (b) Asymmetric relief is a sum of the absolute values of modes 3 and 5. (c) Total relief is the sum of the symmetric and asymmetric components when the asymmetric component is assigned the sign of the symmetric component. Maximum axial valley depth decreases with spreading rate for rates less than ~80 mm yr^{-1} while axial ridge height remains relatively constant for rates greater than ~50 mm yr^{-1}. Significant asymmetry is limited to ridges with spreading rates less than 40 mm yr^{-1}.

Individual examples of this decomposition are shown for 20 example profiles in the appendix. As it is not feasible to show all 156 profiles here, only the most instructive have been included. These represent both the best and worst examples of this representation of the data as well as profiles that differ substantially from classical ridge axis bathymetry. Each example shows the original profile, the profile reconstructed from the first five modes and the residual plotted above. It is apparent that in almost every case the first five modes do an excellent job of representing the salient features in the data. It can also be seen that the residual profiles are not dominated by misfits of the axial relief but rather appear relatively uniform along the length of the profile and contain isolated off-axis features such as seamounts. The largest residual in the data set is associated with profile 12; although the steep sides of the axial valley are poorly approximated by the first five modes, the residual profile is dominated by two rather large (>1 km) features off axis. These profiles illustrate the substantial variability in both amplitude and shape of axial valleys at similar spreading rates on slow spreading ridges. It is apparent that this type of variability would make it very difficult to describe these profiles accurately with analytic functions.

Axial depth, shown in Fig. 5, was measured at the axis of each profile prior to the analysis. As with axial relief, axial depth shows considerable variability for spreading rates less than 80 mm yr^{-1} and relatively little scatter for higher rates. Although axial depth does not remain constant for rates greater than 80 mm yr^{-1}, it does vary consistently and shows

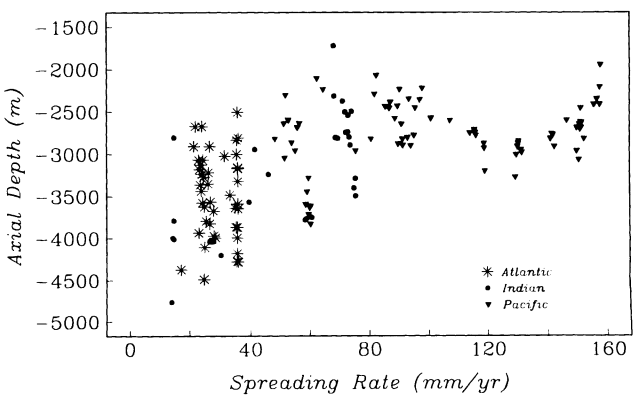

Figure 5. Axial depth versus spreading rate for the global data set. Maximum axial depth decreases with spreading rate for rates less than 80–100 mm yr^{-1}. Variance about the mean trend decreases abruptly for rates greater than 80 mm yr^{-1} although the trend shows a local deepening on the East Pacific Rise near the Galapagos Rise at 120 mm yr^{-1}.

very little scatter at any given spreading rate. The consistent variation in depth at the faster spreading rates is a result of the deepening of the East Pacific Rise near the Galapagos Rise. It has been observed that axial depth is correlated with axial ridge shape on the East Pacific Rise (Macdonald & Fox 1988) and with axial valley relief on the Mid-Atlantic Ridge (Le Douaran & Francheteau 1981). As shown by Malinverno (1990), some correlation between relief and depth is expected if the relief measurement is a component of the depth measurement. Fig. 6 shows axial depth plotted versus axial relief for the 156 profiles used in this study. The axial depth shows the expected positive correlation ($r = 0.8$) for axial valleys at slow rates and for ridges with positive relief at faster rates. Also plotted are the flanking depths in which the axial relief is subtracted from the axial depth (total depth = flanking depth + axial relief). When the relief is subtracted from the total depth a correlation between the two is not required as the depth to the flank is statistically independent of the relief itself. The flanking depth is also correlated with axial relief although in the opposite sense ($\rho = -0.7$). When considered separately, axial valley relief is still correlated with both axial depth and flanking depth

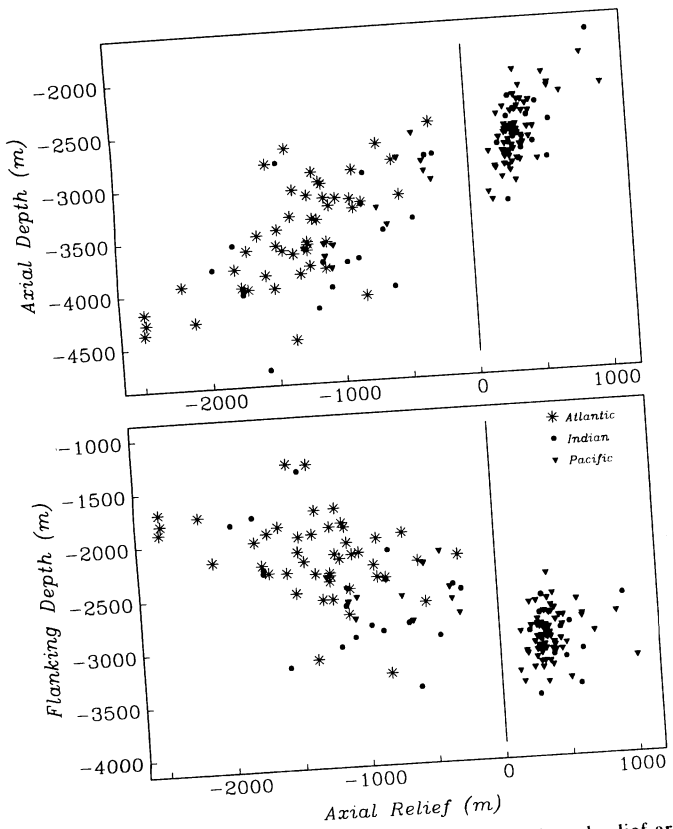

Figure 6. Axial depth versus axial relief. Axial depth and relief are strongly correlated ($\rho = 0.8$) for both fast and slow spreading ridges (top). When axial relief is subtracted from axial depth to give flanking depth, the correlation remains ($r = -0.7$) but becomes negative. When slow spreading ridges are considered separately, the correlation of axial and flanking depths with negative relief have equal slopes of 0.6 and −0.4 respectively and a common intercept of −2745 m, thus supporting the observation that axial valley depth is balanced by flanking uplift. As axial valley relief decreases, corrected axial valley depth approaches that of fast spreading ridges.

although to a lesser extent ($\rho = 0.6$ and -0.5 respectively). Linear trends fit to the axial depth and flanking depth give slopes of −0.6 and 0.4, respectively, and a common intercept of −2838 m. Because the parameters discussed in this study are generally not normally distributed, all correlation coefficients are computed using the Spearman Rank Order coefficient, ρ (Press *et al.* 1992) and linear trends are fit by minimizing the $L1$ norm. All correlations quoted are significant at the 99 per cent confidence level.

An advantage of an EOF decomposition is that it may provide a basis for distinguishing between the deterministic components of the topography and the stochastic components. Although the decomposition does not provide a means for explicitly determining which components are deterministic and which are stochastic in a statistical sense, it does provide a set of modes which may be compared with those forms of axial topography which have been previously observed. Modes 1–5 have obvious physical interpretations as discussed above and, for the purpose of this study, are considered to be the recognizable modes of topographic expression. Modes 6–79 have no obvious physical interpretation and may be considered stochastic components of topographic roughness. Visual examination of profiles as shown in the appendix indicates that modes 1–5 do indeed account for the majority of the recognizable topographic expression in almost every profile while the sum of the higher modes resembles topographic roughness. It is also encouraging that this decomposition relegates sporadic features such as off-axis seamounts to the roughness component of the topography as shown by profiles 78, 135, 136 and 147. Because the residual profiles often contain seamounts and are, in general, not normally distributed, the Median Absolute Deviation (MAD) is used as an estimate of their topographic roughness. Although the MAD produces lower estimates of roughness than the commonly used RMS, it provides a more robust estimate in the presence of outliers such as seamounts. The roughness is plotted as a function of spreading rate in Fig. 7.

It has been proposed by Malinverno (1991) that ridge flanking roughness, as defined by the RMS of the bathymetry, varies inversely with the square root of spreading rate as $R = A/\sqrt{v} + B$. This assertion is considered in Fig. 8. The roughness values computed here were fit with a function of the form $R = A/\sqrt{v} + B$ and this function was subtracted from the observed data. The residual (observed − predicted) roughness is shown in Fig. 8(b). Although the data can be fit with this curve, it should be noted that the scatter about the predicted value is consistently higher for rates less than ~80 mm yr^{-1} and that the predicted curve fails to fit the trend of the observed data for rates greater than 80 mm yr^{-1}. The parameters A and B were estimated by minimizing the $L1$ norm and give $A = 1214$ and $B = -46$. In order to be directly comparable with the aforementioned study, the roughness was also estimated using the RMS instead of the MAD and gives $A = 1122$ as compared to Malinverno's value of $A = 1296$. Also shown in Fig. 8 is a log–log plot of the roughness versus spreading rate. It can be seen that the data do not show a well-defined linear trend in log–log space, thereby providing a strong argument against any power law dependence of roughness on spreading rate.

It is immediately apparent that the roughness shows a

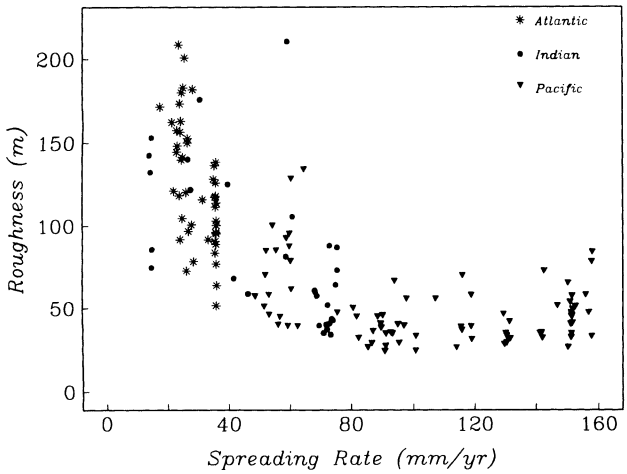

Figure 7. Bathymetric roughness versus spreading rate for the global data set. Roughness is defined as the Median Absolute Deviation (MAD) of the residual profile which is obtained by removing the first five modes from the original profile. Roughness decreases with spreading rate for rates less than 80 mm yr^{-1} and remains relatively constant at higher rates.

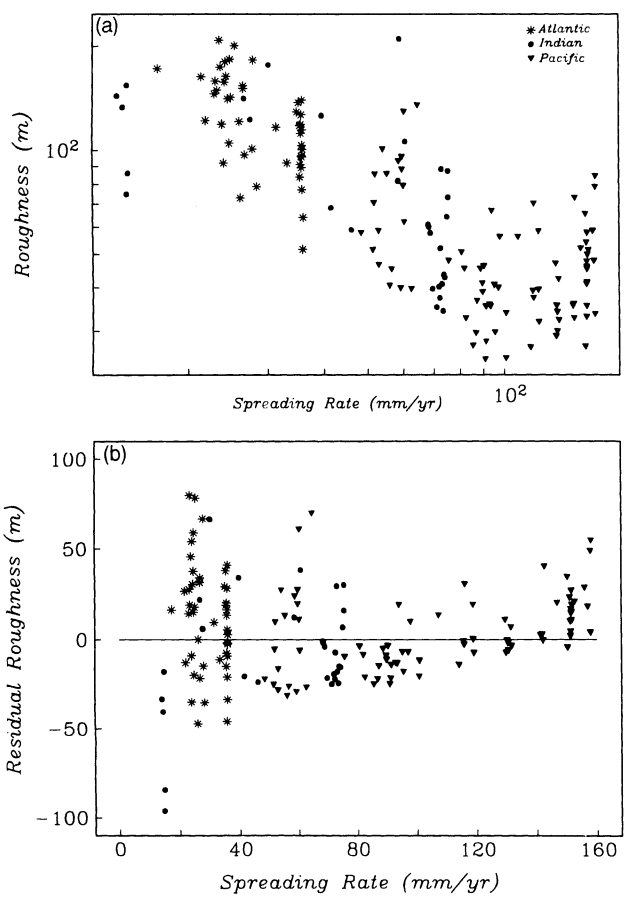

Figure 8. Roughness and spreading rate are tested for a power law relationship. (a) Roughness and spreading rate are plotted in log–log space and show a significant deviation from a linear relationship at spreading rates >80 mm yr^{-1}. (b) Residual roughness is plotted after the best fit $A/\sqrt{v} + B$ is removed from the data. There is considerable scatter for rates less than 80 mm yr^{-1} and a significant misfit to the trend at rates greater than 80 mm yr^{-1}.

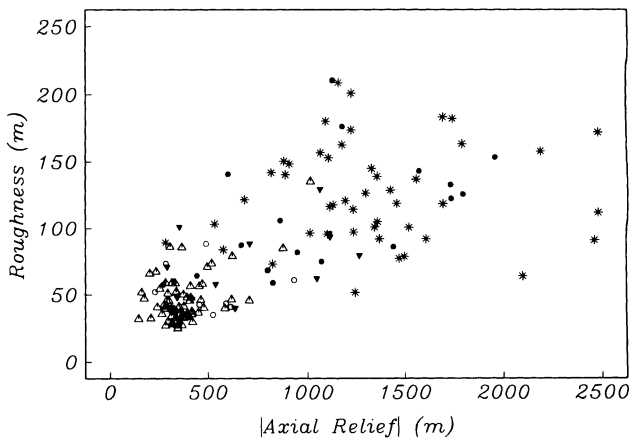

Figure 9. Bathymetric roughness versus absolute axial relief for the global data set. Different symbols indicate primary ocean basins as in previous figures; open symbols indicate positive relief. Although there is an overall correlation ($\rho = 0.7$), axial valley relief alone is weakly correlated ($\rho = 0.4$) with flanking bathymetric roughness.

similar variation with spreading rate to the axial relief shown in Fig. 4. The obvious implication is that topographic roughness is somehow related to axial relief. Roughness is plotted as a function of absolute axial relief in Fig. 9 and shows a correlation of 0.7. Roughness is also weakly correlated with mode 1 ($\rho = 0.5$) and mode 2 ($\rho = -0.6$) individually although not with mode 3 ($\rho = 0.2$), mode 4 ($\rho = 0.2$) or mode 5 ($\rho = 0.2$). Although the correlations are statistically significant, an examination of the profiles shows numerous exceptions. If slow spreading ridges are considered separately the correlation decreases ($\rho = 0.4$), implying that axial valley depth is not related in a simple way to a near-axis bathymetric roughness.

DISCUSSION

Deterministic and stochastic topography

A primary result of this analysis is that approximately 50 per cent of the topographic relief on the ridge axis may be described as a combination of simple modes. The implication is that the remaining 50 per cent cannot be described simply and appears to be stochastic. Although the decomposition does not provide a statistical basis for establishing the separation, the distribution of singular values and the distinction of the five primary modes strongly support this interpretation. Additional support is offered by the profiles shown in the appendix. The stochastic component is referred to as bathymetric roughness and is discussed below.

This analysis also shows that the majority of morphologic variability is related to slow spreading ridges. When fast spreading ridges are analysed independently, the two dominant modes are similar in form and account for only 29 per cent of the topographic relief. This may be attributed to, the presence of off-axis seamounts which are comparable to or larger in size than, the axial ridge, but are distributed throughout the length of the profile thereby requiring a large number of modes to represent them. Although it has

been shown that the shape of axial ridges often varies with respect to the segmentation (Macdonald & Fox 1988), the large scale structure of fast spreading centres is relatively invariant in comparison with slow spreading ridges. For this reason the majority of fast spreading ridge topography may be represented with just one mode in the global analysis. This is indicated by the dominance of mode 2 for fast spreading ridges as shown by *C*2 in Fig. 3.

It is not yet possible to determine how much of the variability seen on slow spreading ridges may be attributed to segmentation. Once the fine scale segmentation of the world's slow spreading centres has been mapped in greater detail this type of analysis may provide a convenient means of quantifying the relationship between segmentation and morphology. It appears that we are presented with two types of variability in ridge axis morphology: a large scale variability (Fig. 4) which may possibly be explained by the dynamics of lithospheric accretion; and a smaller scale variability (Fig. 7) which may be related to these dynamics but probably cannot be explained deterministically.

Axial and flanking depth variations

The nearly equal slopes seen in Fig. 6 support the notion that axial valley depth is, to some degree, balanced by uplift of the flanking walls as predicted by isostasy (Weissel & Karner 1989) and numerous theoretical models (e.g. Lachenbruch 1973; Collette, Verhoef & Mulder 1980; Parmentier 1987; Phipps Morgan, Parmentier & Lin 1987). Although it would be necessary to integrate the axial topography to demonstrate such a mass balance, the measure used here is more robust because it is not dependent on a datum level or a profile length. The variation in axial depth is slightly greater than the variation of flanking depth with axial relief (0.6 versus −0.4). This may be a result of axial deepening near transform offsets which is not exactly balanced by flanking uplift.

As might be expected, flanking depths on slow spreading ridges approach the mean flanking depth of fast spreading ridges (3012 ± 223 m) as the spreading rate increases. This is consistent with the results of Marty & Cazenave (1989) which show increased subsidence rates for ridges with mean axial depths less than ~3000 m. These observations support the notion of a dynamic equilibrium for spreading ridges. The intermediate scale segmentation and 3-D structure of slow spreading ridges may be considered perturbations which become increasingly unstable at higher spreading rates.

Bathymetric roughness

The dependence of bathymetric roughness on spreading rate is similar to that found by Goff (1991), Hayes & Kane (1991) and Malinverno (1991) for ridge flanking topography. Although the different methods used to estimate roughness give different values, the variation with spreading rate is similar. The Median Absolute Deviation (MAD) gives lower estimates than the RMS but is preferable in this case because the distributions of the residual profiles are significantly non-Gaussian. When the RMS is used to estimate the amplitude of the residual profiles the results are consistent with the studies mentioned above.

It has been proposed by Malinverno (1991) that sea-floor roughness varies continuously and is *inversely* proportional to the square root of the spreading rate. This hypothesis is not supported by the results of this study, as shown by Fig. 8. While these results do not disprove Malinverno's hypothesis, they do imply some additional complications. The slight increase in both average roughness and in the range of roughness values seen in this analysis and in that by Goff (1991) for spreading rates greater than 80 mm yr^{-1} implies factors which cannot be explained by a monotonically decreasing function of spreading rate. In addition to the well known increase in seamount production in the vicinity of the Easter Microplate, Goff (1991) also finds consistent differences in size and shape of abyssal hills on the Pacific Cocos and Pacific Nazca sections of the East Pacific Rise. Some of the variability of the roughness values at slow spreading ridges may be accounted for by the length of the profiles used in this study. Longer profiles, such as those used in the aforementioned studies, may tend to average out time-dependent variations in faulting and volcanism which are responsible for creating abyssal hill topography. An additional complication arises from the results of Malinverno (1991) and a recent study by Bird & Pockalny (private communication) which find significantly different spreading-rate variations for ridge flank roughness.

Although the amount of scatter in the roughness estimates at slow spreading rates could mask either a linear dependence (Hayes & Kane 1991) or a power law dependence (Malinverno 1991), existing profile data are not adequate to distinguish between the two models. Furthermore, the low spatial resolution and uneven sampling which are characteristic of wide beam echosounders introduce a variety of bases related to spatial aliasing. A more complete understanding of the processes involved in the creation of abyssal hill topography requires a number of detailed multibeam surveys at all spreading rates. Roughness estimates based only on profile data obviously lack the information content of more thorough investigations such as that of Goff (1991); however, the coverage of the ridge system currently offered by multibeam data precludes a thorough global study at this time.

A complication which is usually overlooked in studies of sea-floor roughness is that of multiple sources. In addition to abyssal hill topography, ridge flank roughness may also include substantial contributions from time-dependent variations in ridge axis segmentation. Oblique fracture zones and propagating offsets create significant topography which cannot be avoided even by sampling along tectonic flow times. It is well known that there are marked differences in the nature of offset propagation and segmentation on fast and slow spreading ridges. In light of this observation, any variation (continuous or abrupt) of roughness with spreading rate must consider segmentation as well as volcanism and faulting. Unfortunately, any study of ridge flank roughness that is based only on profile data will suffer from this ambiguity.

Fast versus slow spreading structure

A fundamental result of this study is that axial relief, depth and roughness all show similar variations with spreading

rate. Although the differences between fast and slow spreading ridges have been known for some time (e.g. Menard 1967), these results show a consistent global pattern of high variability and rate dependence at slow spreading centres changing to low variability and rate independence at fast spreading centres. The transition occurs at spreading rates in the 50–80 mm yr^{-1} range and may be the result of marked differences in the episodicity of processes occurring at the ridge axis.

Multibeam surveys on the southern Mid-Atlantic Ridge indicate that at spreading rates as low as 35 mm yr^{-1} axial valleys may shallow and disappear completely (Welch *et al.* 1987; Kuo & Forsyth 1988; Blackman & Forsyth 1991; Fox, Grindlay & Macdonald 1991). This does not necessarily imply a change in the mode of crustal accretion although it may result from a local relaxation of the forces responsible for maintaining the axial valley as proposed by Blackman & Forsyth (1991). The axial valley is also seen to disappear on the northern Mid-Atlantic Ridge in the vicinity of the Iceland and Azores hotspots; this is presumably a result of the elevated thermal structure in these areas. The South-east Indian Ridge has two well-developed transitions from axial ridge to axial valley structures although neither has been surveyed in detail. High-resolution satellite gravity measurements from the Geosat Geodetic Mission (GM) show a similar transition on the Pacific Antarctic Rise although bathymetric coverage of this area is also extremely sparse.

At present, the majority of models for mid-ocean ridge axial topography assume some type of steady-state mechanism which varies with spreading rate. If the variation in axial morphology is continuous, as implied by the model of Phipps Morgan *et al.* (1987), then it would be expected to be controlled by factors that vary continuously with spreading rate such as the large scale thermal structure. Alternatively, a threshold model such as that proposed by Chen & Morgan (1900a, b) would be more sensitive to factors which change rapidly or are easily perturbed by local variability. More recent models, such as those of Phipps Morgan & Chen (1993) and Neumann & Forsyth (1992), are based on the mechanisms in the aforementioned studies and account for additional complexities such as crustal thickness variations and the existence of a steady-state magma chamber. Theoretical models also suggest that the fundamental nature of mantle flow fields (Parmentier & Phipps Morgan 1990) and the existence of a steady-state magma chamber (Phipps Morgan & Chen 1993) may be controlled by the thermal structure at the ridge axis. These models are appealing because they can explain both the change in structural/morphologic variability seen between fast and slow spreading ridges as well as the characteristics of anomalous ridges such as the Reykjanes Ridge and the Australian Antarctic Discordance Zone. In spite of the constraints offered by the data shown here, a thorough understanding of the cause of these differences will require detailed surveys of intermediate rate ridges where the transitions are seen to occur.

The striking differences in the morphologic variability of fast and slow spreading ridges may be a result of the episodicity of crustal accretion on slow spreading ridges. While the maximum attainable axial valley relief is seen to decrease with spreading rate, shallow axial valleys appear to be present at all spreading rates less than ~80 mm yr^{-1}. An episodic supply of magma to the ridge axis would create a temporal variability in the thermal structure at any given location on the ridge axis. Since the thermal structure is probably the dominant control on the mechanism which maintains the axial valley, this would account for the variability seen in axial relief. The thermal structure also controls the ductile deformation in the lower crust, thereby limiting the yield strength of the lithosphere near the ridge axis. Episodic brittle failure would occur during episodes of amagmatic extension producing greater roughness from faulting. This temporal variability may explain the imperfect correlation between axial valley relief and roughness. At higher spreading rates the elevated thermal structure and greater magma supply may allow the existence of a steady-state melt lens and a composite magma chamber as proposed by Sinton & Detrick (1992) and Phipps Morgan & Chen (1993). The temporally consistent, elevated thermal structure results in a consistently weak lower crust and upper mantle which would prevent large stresses from accumulating. If the lithosphere is able to alleviate stresses more frequently with smaller displacements, the overall roughness resulting from faulting would be expected to decrease accordingly.

CONCLUSIONS

The use of Empirical Orthogonal Functions to represent mid-ocean ridge morphology provides a basis for the separation of the data field into deterministic and stochastic components and gives the dependence of each on parameters such as spreading rate and axial depth. It is shown that this representation of the axial morphology is extremely robust to variations in the input data set and gives quantitative results which agree with qualitative observations from previous studies. On the basis of the spectral decomposition of 156 bathymetric profiles, approximately half of the morphologic relief within 30–50 km of the ridge axis may be represented as a linear combination of five recognizable modes; the remainder is considered stochastic.

Maximum values of both deterministic and stochastic components of axial morphology show a consistent variation with spreading rate for rates less than 80 mm yr^{-1} but remain relatively constant at higher rates. This implies that the maximum attainable axial valley relief is ultimately controlled by spreading rate. Minimum relief of axial valleys shows no spreading rate dependence, indicating that local conditions can prevent the formation of an axial valley at slow spreading rates but cannot create an axial valley at faster rates. This supports the notion that a critical threshold exists above which an axial valley cannot be maintained. This threshold is not expected to be dependent on spreading rate alone but more directly on thermal structure, rheology and melt availability, which are strongly influenced by spreading rate but are also subject to other influences such as upwelling structure and the proximity of hotspots.

Axial depth is positively correlated with axial relief, as would be expected. Flanking depth is negatively correlated with relief. In the case of slow spreading ridges with axial valleys this supports the common assumption that the axial valley depth is, to some extent, balanced by uplift of the rift flanks. Flanking depth on slow spreading ridges approaches

the mean axial depth of fast spreading ridges as the axial valley shallows, implying an equilibrium depth for mid-ocean ridges.

Spreading centres with axial ridges show consistently lower roughnesses than those with axial valleys but axial valley depth is not strongly correlated with flanking roughness at slow spreading centres. A possible explanation for these observations is the episodicity of magmatic heat supplied to slow spreading ridges. The thermal structure of slow spreading ridges is expected to have greater temporal and spatial variability, which may account for the variability in axial valley relief and roughness. Faster spreading ridges would be expected to maintain a thermal steady state with a significantly weaker lower crust and upper mantle which would limit the degree of roughness that could be produced by episodic brittle failure.

ACKNOWLEDGMENTS

This study would not have been possible without the support and encouragement of David Sandwell. I am deeply indebted to Catherine Johnson for countless discussions and reviews which resulted in a much improved work. I also wish to thank Russ Davis, Peter Lonsdale and Robert Parker for useful discussions and criticisms and two anonymous reviewers for their suggestions. Donna Blackman kindly provided the gridded Seabeam data shown in the appendix. This work was supported by NSF Ocean Sciences Program (OCE 92-17164).

REFERENCES

Akima, H., 1970. A new method of interpolation and smooth curve fitting based on local procedures, *J. Ass. Comput. Mach.*, **17,** 589–602.

Blackman, D. K. & Forsyth, D. W., 1991. Isostatic compensation of tectonic features of the Mid-Atlantic Ridge: 25–27.30°S, *J. geophys. Res.*, **96,** 11 741–11 758.

Carbotte, S., Welch, S. M. & Macdonald, K. C., 1991. Spreading rates, rift propagation and fracture zone offset histories during the past 5 Myr on the Mid-Atlantic Ridge, *Mar. geophys. Res.*, **13,** 51–80.

Chen, Y. & Morgan, W. J., 1990a. A non-linear rheology model for mid-ocean ridge topography, *J. geophys. Res.*, **95,** 17 583–17 604.

Chen, Y. & Morgan, W. J., 1990b. Rift valley/no rift valley transition at mid-ocean ridges, *J. geophys. Res.*, **95,** 17 571–17 583.

Collette, B. J., Verhoef, J. & Mulder, A. F. J. D., 1980. Gravity and a model of the median valley, *J. Geophys.*, **47,** 91–98.

Davis, R. E., 1976. Predicatability of sea surface temperature and sea level pressure anomalies over the North Pacific Oceans, *J. Phys. Ocean.*, **6,** 249–266.

DeMets, C. & Stein, S., 1990. Present-day kinematics of the Rivera plate and implications for tectonics in southwestern Mexico, *J. geophys. Res.*, **95,** 21 931–21 948.

DeMets, C., Gordon, R. G., Argus, D. F. & Stein, S., 1990. Current plate motions, *Geophys. J. Int.*, **101,** 425–478.

Fox, P. J., Grindlay, N. R. & Macdonald, K. C., 1991. The Mid-Atlantic Ridge (31°S–34.30°S): Temporal and spatial variations of the accretionary process, *Mar. geophys. Res.*, **13,** 1–20.

Goff, J. A., 1991. A global and regional stochastic analysis of near-ridge abyssal hill morphology, *J. geophys. Res.*, **96,** 21 713–21 737.

Hayes, D. E. & Kane, K. A., 1991. The dependence of seafloor roughness of spreading rate, *Geophys. Res. Lett.*, **18,** 1425–1428.

Kuo, B. Y. & Forsyth, D. W., 1988. Gravity anomalies of the ridge–transform system in the South Atlantic between 31 and 34.5°S: Upwelling centers and variations in crustal thickness, *Mar. geophys. Res.*, **10,** 205–232.

Lachenbruch, A. H., 1973. A simple mechanical model for oceanic spreading centers, *J. geophys. Res.*, **78,** 3395–3417.

LeDouaran, S. Francheteau, J., 1981. Axial depth anomalies from 10° to 50° north along the Mid-Atlantic Ridge: Correlation with mantle properties, *Earth planet. Sci. Lett.*, **54,** 29–47.

Lorenz, E. N., 1959. Empirical Orthogonal Functions and statistical weather prediction, *Statistical Forecasting Project*, Vol. 1. Dept. Meteorology, MIT.

Macdonald, K. C. & Fox, P. J., 1988. The axial summit graben and cross-sectional shape of the East Pacific Rise as indicators of axial magma chambers and recent volcanic eruptions, *Earth planet. Sci. Lett.*, **88,** 119–131.

Malinverno, A., 1990. A quantitative study of the axial topography of the Mid-Atlantic Ridge, *J. geophys. Res.*, **95,** 2645–2660.

Malinverno, A., 1991. Inverse square-root dependence of mid-ocean ridge flank roughness on spreading rate, *Nature,* **352,** 58–60.

Marty, J. C. & Cazenave, A., 1989. Regional variations in subsidence rate of oceanic plates: a global analysis, *Earth planet. Sci. Lett.*, **94,** 301–315.

Menard, H. W., 1967. Seafloor spreading, topography and the second layer, *Science,* **157,** 273–278.

Menke, W., 1989. *Geophysical Data Analysis: Discrete Inverse Theory,* Academic Press, New York.

Minster, J. B. & Jordan, T. H., 1978. Present day plate motions, *J. geophys. Res.*, **83,** 5331–5354.

Neumann, G. A. & Forsyth, D. W., 1992. An extensional model that predicts along-axis variation in bathymetry and rift valley structure along the Mid-Atlantic Ridge, *EOS, Trans. Am. geophys. Un.*, **73,** 551.

Parmentier, E. M., 1987. Dynamic topography in rift zones; Implications for lithospheric heating, *Phil. Trans. R. Soc. Lond.*, A, **321,** 23–25.

Parmentier, E. M. & Morgan, J. P., 1990. The spreading rate dependence of three dimensional structure in oceanic spreading centres, *Nature,* **348,** 325–328.

Phipps Morgan, J. & Chen, Y. J., 1993. The genesis of ocean crust: Magma injection, hydrothermal circulation, and crustal flow, *J. geophys. Res.*, **98,** 6283–6298.

Phipps Morgan, J., Parmentier, E. M. & Lin, J., 1987. Mechanisms for the origin of midocean ridge axial topography: Implications for the thermal and mechanical structure of accreting plate boundaries. *J. geophys. Res.*, **92,** 12 823–12 836.

Press, W. H., Flannery, B. P., Teukolsky, S. A. & Vetterling, W. T., 1992. *Numerical Recipes,* 2nd edn, Cambridge University Press, New York.

Severinghaus, J. P. & Macdonald, K. C., 1988. High inside corners at ridge–transform intersections, *Mar. geophys. Res.*, **9,** 353–367.

Shaw, P. R., 1988. An investigation of small-offset fracture zone geoid waveforms, *Geophys. Res. Lett.*, **15,** 192–195.

Sinton, J. M. & Detrick, R. S., 1992. Mid-ocean ridge magma chambers, *J. geophys. Res,* **97,** 197–216.

Small, C. & Sandwell, D. T., 1992. An analysis of ridge axis gravity roughness and spreading rate, *J. geophys. Res.*, **97,** 3235–3245.

Smith, W. H. F., 1992. On the accuracy of digital bathymetric data, *J. geophys. Res.*, **98,** 9591–9604.

Weissel, J. K. & Karner, G. D., 1989. Flexural uplift of rift flanks due to mechanical unloading of the lithosphere during extension, *J. geophys. Res.*, **94,** 13 919–13 950.

Welch, S. M., Macdonald, K. C., Miller, S. P., Fox, P. J. &

Grindlay, N., 1987. Magnetic analysis of a slow spreading plate boundary in the South Atlantic, *EOS, Trans. Am. geophys. Un.*, **67**, 44.

APPENDIX

An example of an EOF analysis using Seabeam data

The techniques described above may also be applied to a data set $D(x, y)$ with two spatial dimensions such as a continuous grid of Seabeam bathymetry measurements. Although such analysis is rarely necessary for a continuous grid of bathymetry, it does provide an instructive example of the decomposition because the individual profiles are highly correlated, thus allowing the reader to visually compare the results of the analysis with the data. A 80×90 km grid of bathymetry measurements collected on the Marathon expedition on the southern Mid-Atlantic Ridge (Carbotte, Welch & Macdonald 1991; Fox *et al.* 1991; Blackman & Forsyth 1991) was chosen to illustrate the analysis. The data, shown in Fig. A1, consist of 90 grid profiles, each 80 km long with 1 km sample spacing and 1 km profile spacing. The grid origin is located at 26.81°S 14.16°W on the southern Mid-Atlantic Ridge and was chosen because it shows significant morphologic variability along axis in the form of shallowing and disappearance of the axial valley. The results of the analysis are shown in Fig. A2. The spectrum of singular values indicates that the topography is dominated by the first mode which accounts for almost 80 per cent of the relief in the form of the axial valley. The coefficients of the first mode indicate a relatively constant amplitude with slight deepening toward the ends of the segment. The second mode accommodates the inside corner high and nodal deep at the northern end of the segment. The third mode modifies the shape of the primary mode by steepening the valley walls and uplifting the flanks. When inverted, the third mode also accounts for the disappearance of the axial valley near 60 km north as shown by the negative values of the sum of modes 1 and 3.

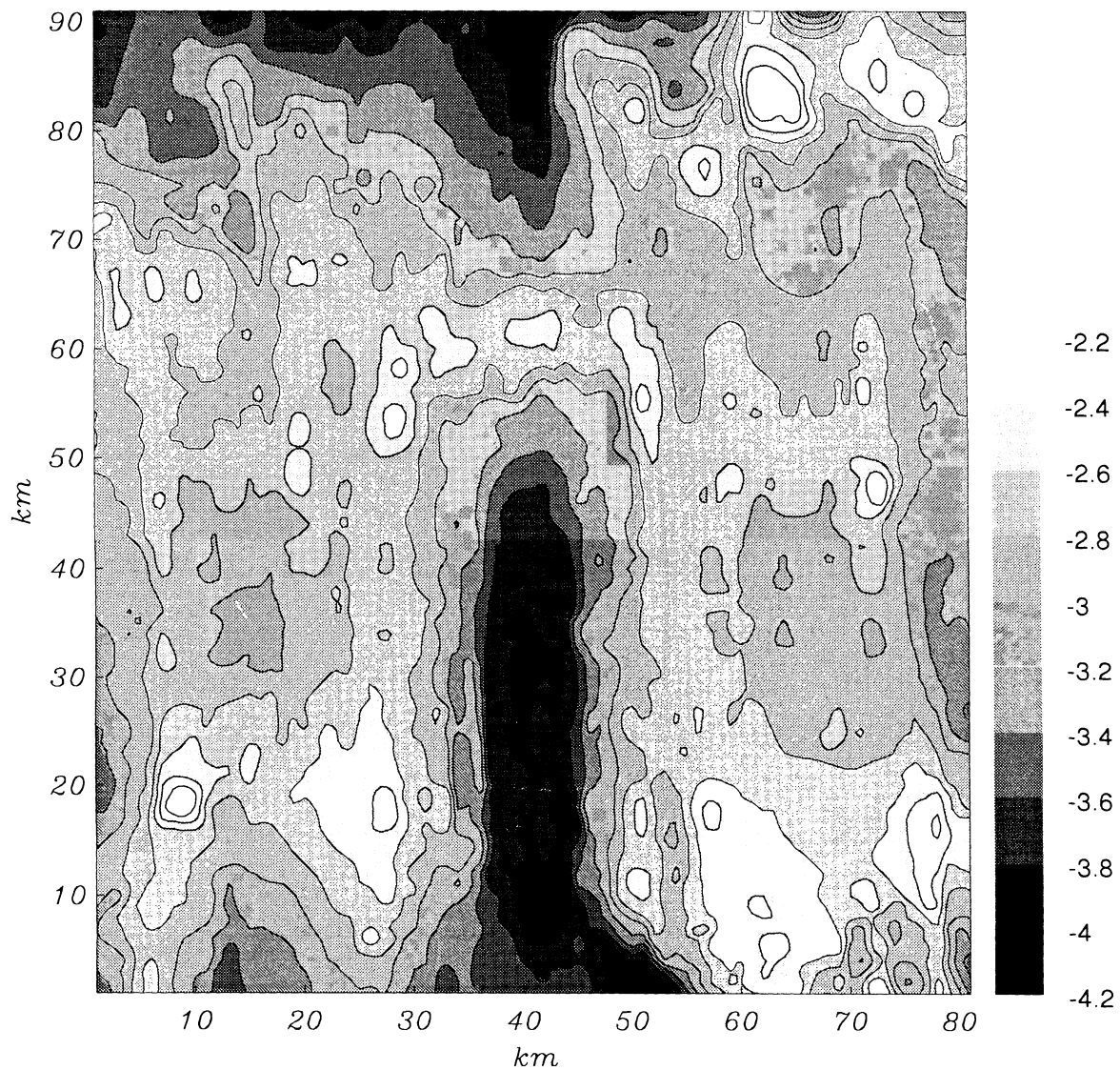

Figure A1. Gridded bathymetry from a Seabeam survey of the southern Mid-Atlantic Ridge from Blackman & Forsyth (1991). The origin of the grid is at 26.81°S 14.16°W and all distances and depths are in kilometres. This grid shows the extreme variability of axial valley morphology possible at a single spreading rate (36 mm yr^{-1}).

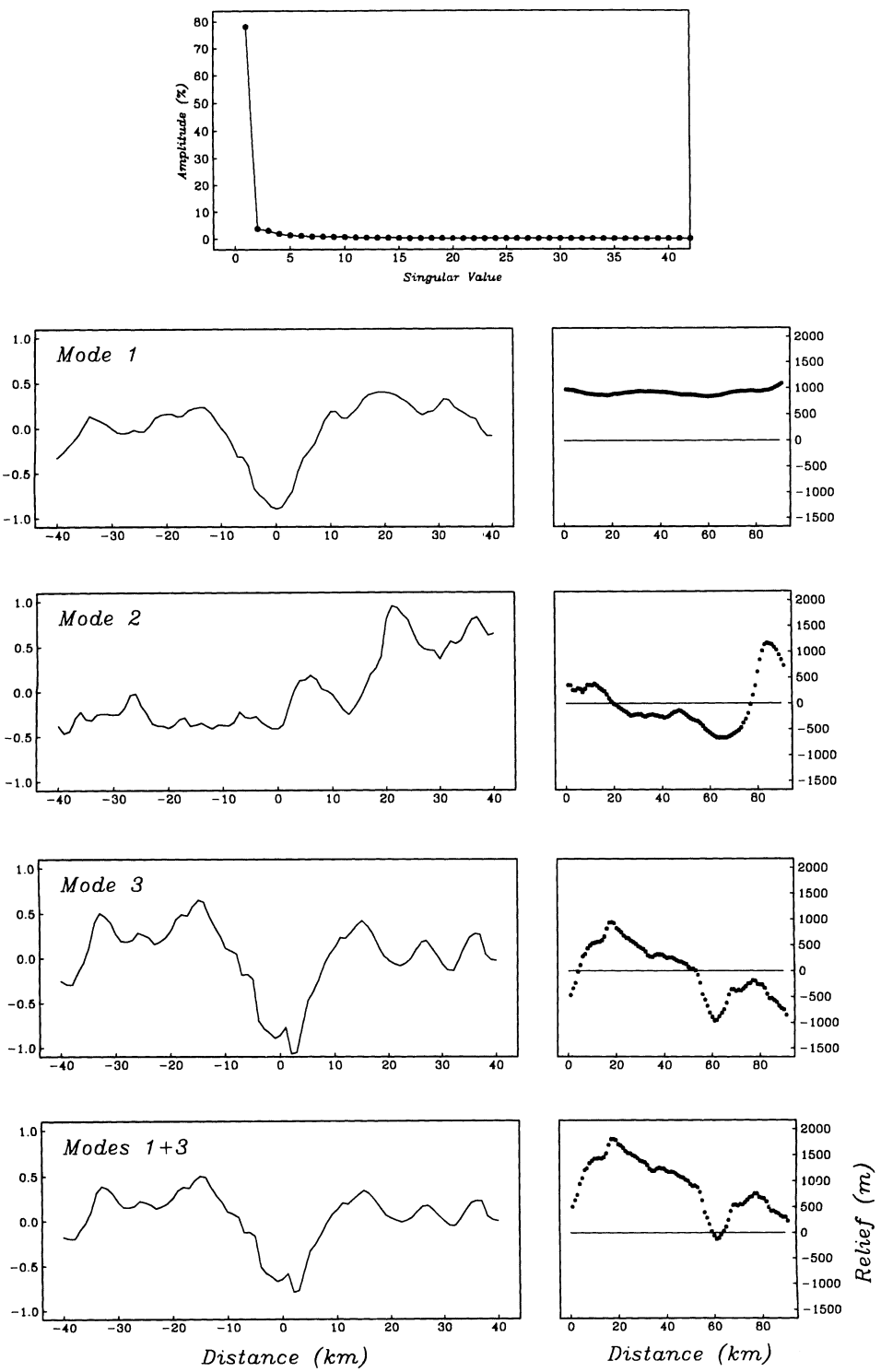

Figure A2. Example of an EOF decomposition of 90 horizontal profiles taken from the grid shown in Fig. A1. Each profile is 80 km long with a 1 km sample spacing. The spectrum of singular values indicates that the first mode accounts for almost 80 per cent of the morphology in this grid. The second and third modes account for an additional 10 per cent and accommodate the inside corner high and nodal deep at the northern end of the grid as well as the disappearance of the axial valley near 60 km. The sum of the first and third modes shows the variations in axial depth along the first 80 km of the ridge axis.

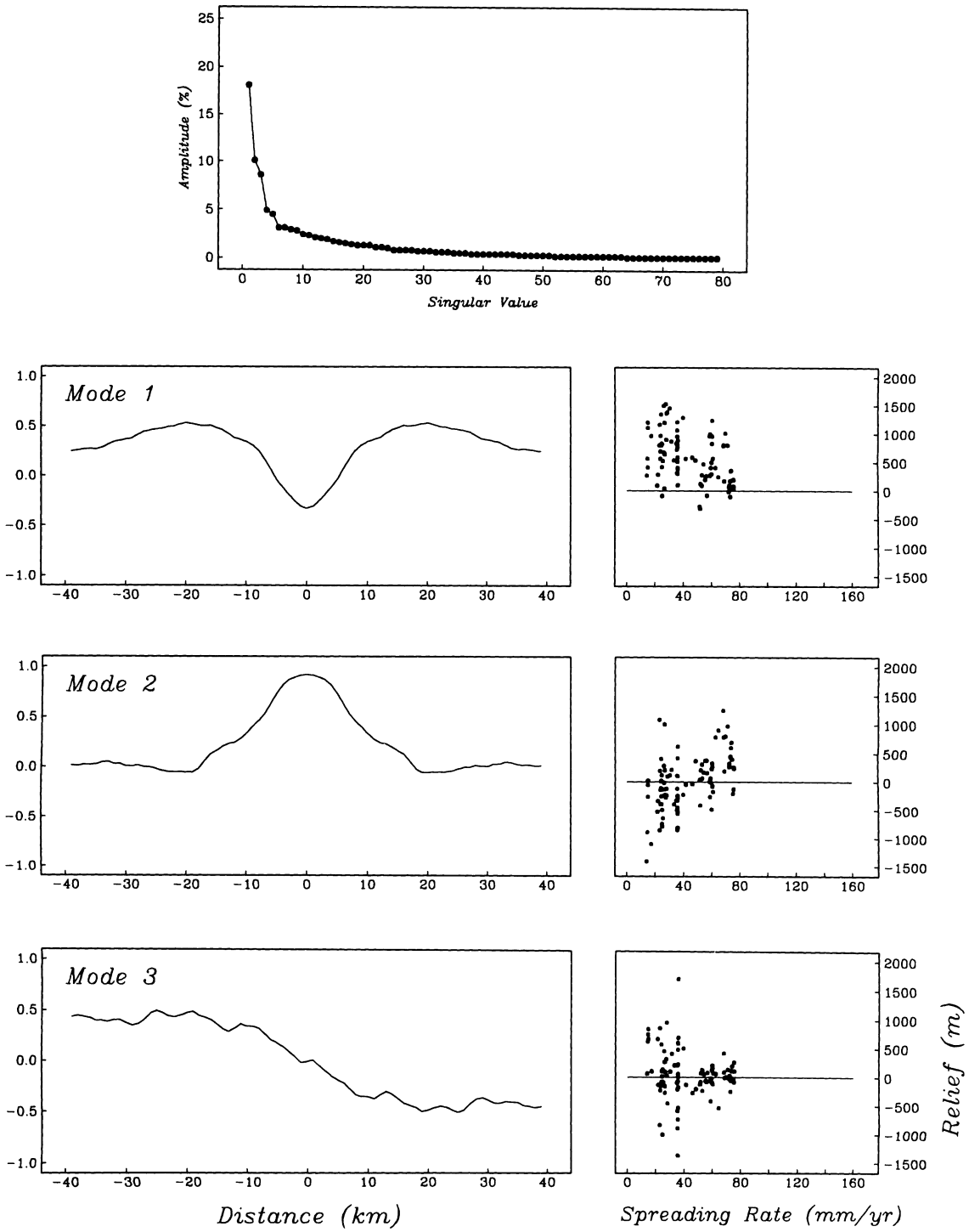

Figure A3. EOF decomposition of profiles from the global data set with spreading rates less than 80 mm yr^{-1}. The singular values and the primary modes are virtually identical to those obtained for the entire data set because the high amplitude topography of the slow spreading ridges dominates the global data set.

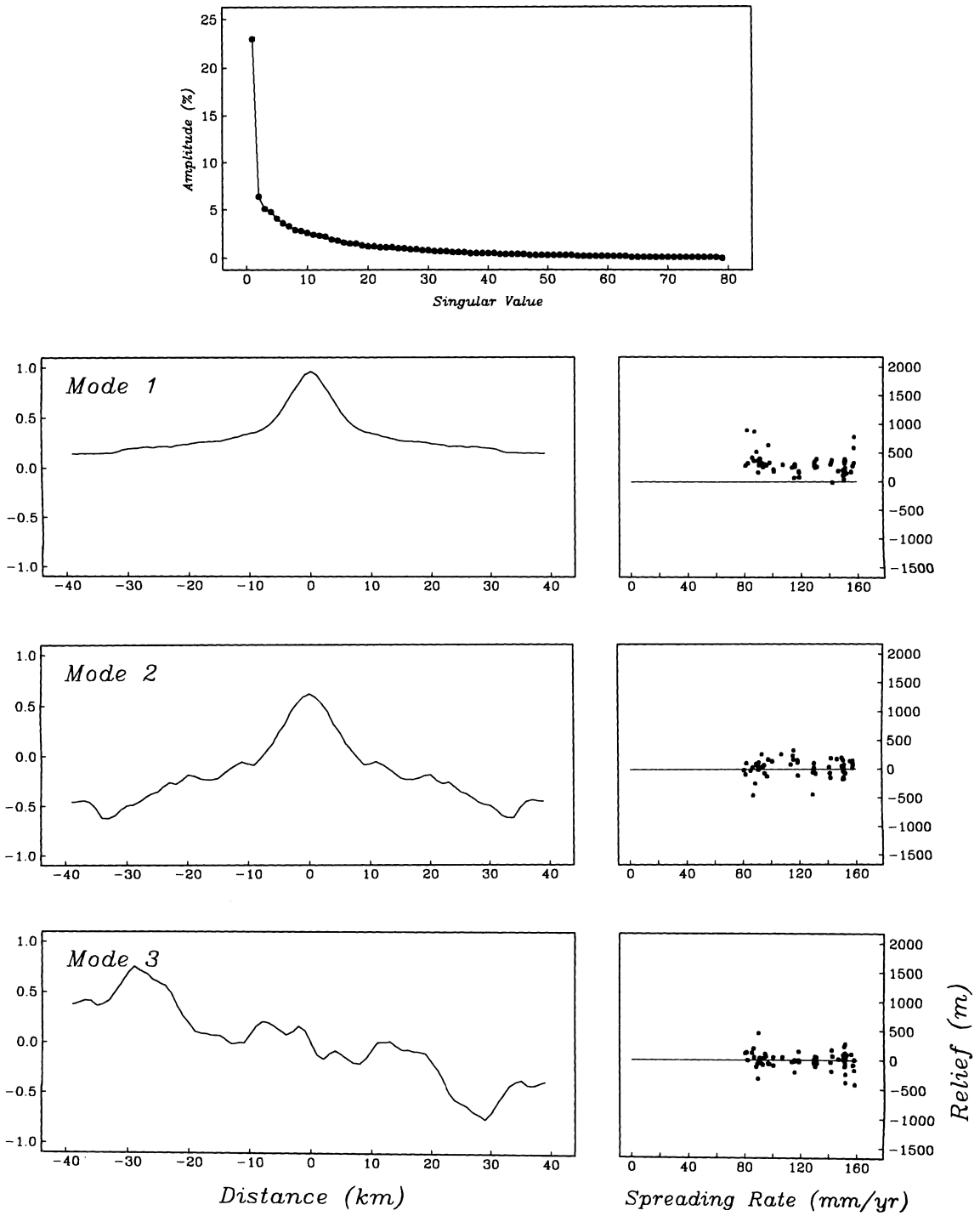

Figure A4. EOF decomposition of profiles from the global data set with spreading rates greater than 80 mm yr^{-1}. These results are significantly different from those from the global data set. Two primary modes account for 30 per cent of the topographic relief and the first five modes account for ~50 per cent. Although the modes are different from those of the global decompositions, the results are equivalent. Axial ridge height does *not vary* with spreading rate and maintains a nearly constant value of ~500 m.

Robustness of EOF analysis of the global data set

Although the results of the analysis are generally consistent with previous observations of ridge axis morphology, it is necessary to verify the robustness of the EOF analysis on these data. As the analysis focuses on $D(x, v)$, variations in the ranges of x and v are of primary concern. Also, given the extreme variability of ridge axis morphology and the uneven distribution of underway data available on the global ridge system, the sensitivity of the analysis to differences in the profiles used in the input data set must also be considered.

In light of the extreme difference between fast and slow spreading ridge axis morphology, these two subsets would be expected to give different results in separate analyses. Fig. A3 shows the results of an EOF analysis of profiles with spreading rates less than 80 mm yr^{-1}. The results are almost indistinguishable from the results of the global analysis. This is not surprising since the slow spreading morphology accounts for most of the amplitude and variability in the global data set. Fig. A4 shows the results of an analysis of the profiles with spreading rates greater than 80 mm yr^{-1}. These results appear significantly different from the global analysis in the shape of the primary modes and the distribution of singular values. The first two modes account for ~30 per cent of the relief and the first five modes account for more than 50 per cent of the topographic relief. The first two modes are similar to what would be expected for fast spreading ridges while the higher order modes do not correspond to recognizable forms of axial morphology. Although the form of fast spreading ridges is relatively homogeneous in comparison to slow spreading ridges, the primary modes still account for only half of the morphology. This may be attributed to the presence of off-axis features which are comparable in size to the axial ridge but vary in location and thus require many independent modes to represent them. Despite the differences between the global and separate analyses for fast spreading ridges, the results are consistent. The primary modes result in a relatively constant axial ridge height of less than 1000 m with no significant asymmetry and no consistent variation with spreading rate. The separate analyses confirm that a global analysis does not result in any significant misrepresentation of the data while simplifying the comparison of fast and slow spreading morphology.

As stated above, the profile length was chosen to maximize the number of usable profiles while adequately representing axial morphology. A significantly shorter

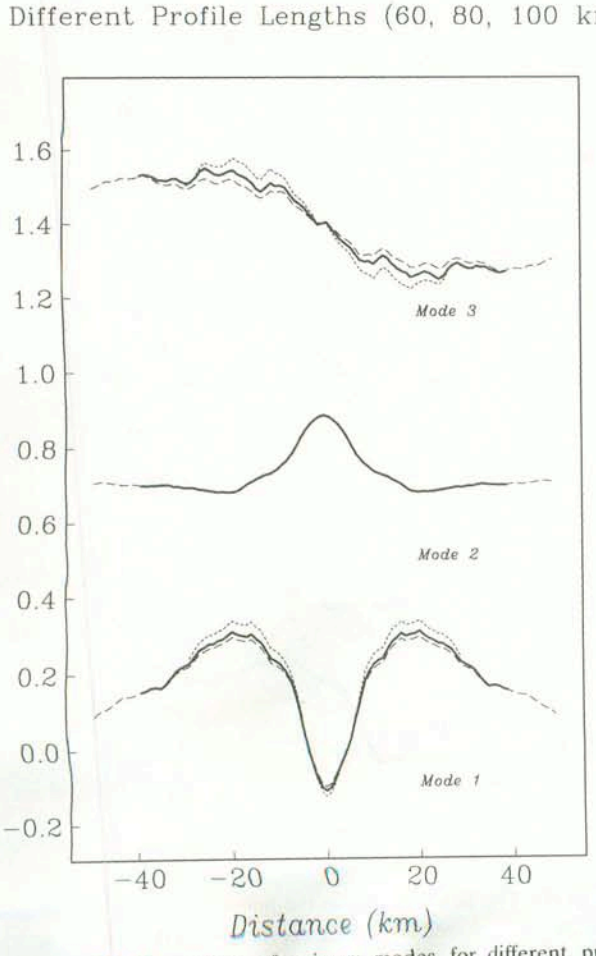

Figure A5. Comparison of primary modes for different profile lengths. Profile lengths of 60, 80 and 100 km result in nearly identical singular values and primary modes indicating that the results are not sensitive to moderate changes in profile length.

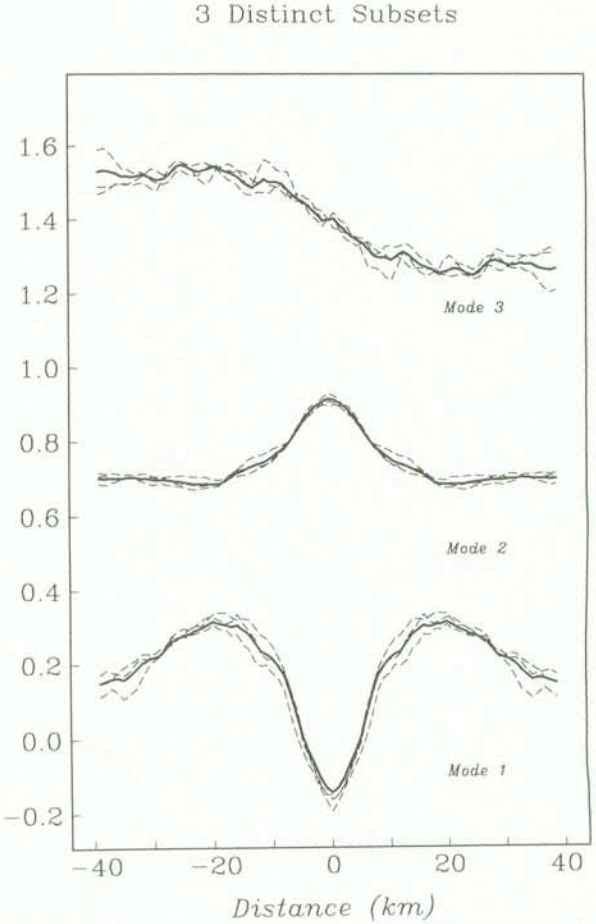

Figure A6. Comparison of primary modes obtained for three distinct subsets of the global data set. The heavy line indicates the modes obtained from the global analysis. In spite of the much smaller independent data sets the modes are still nearly identical indicating that the results of the global analysis are extremely robust with respect to variations in the input data set.

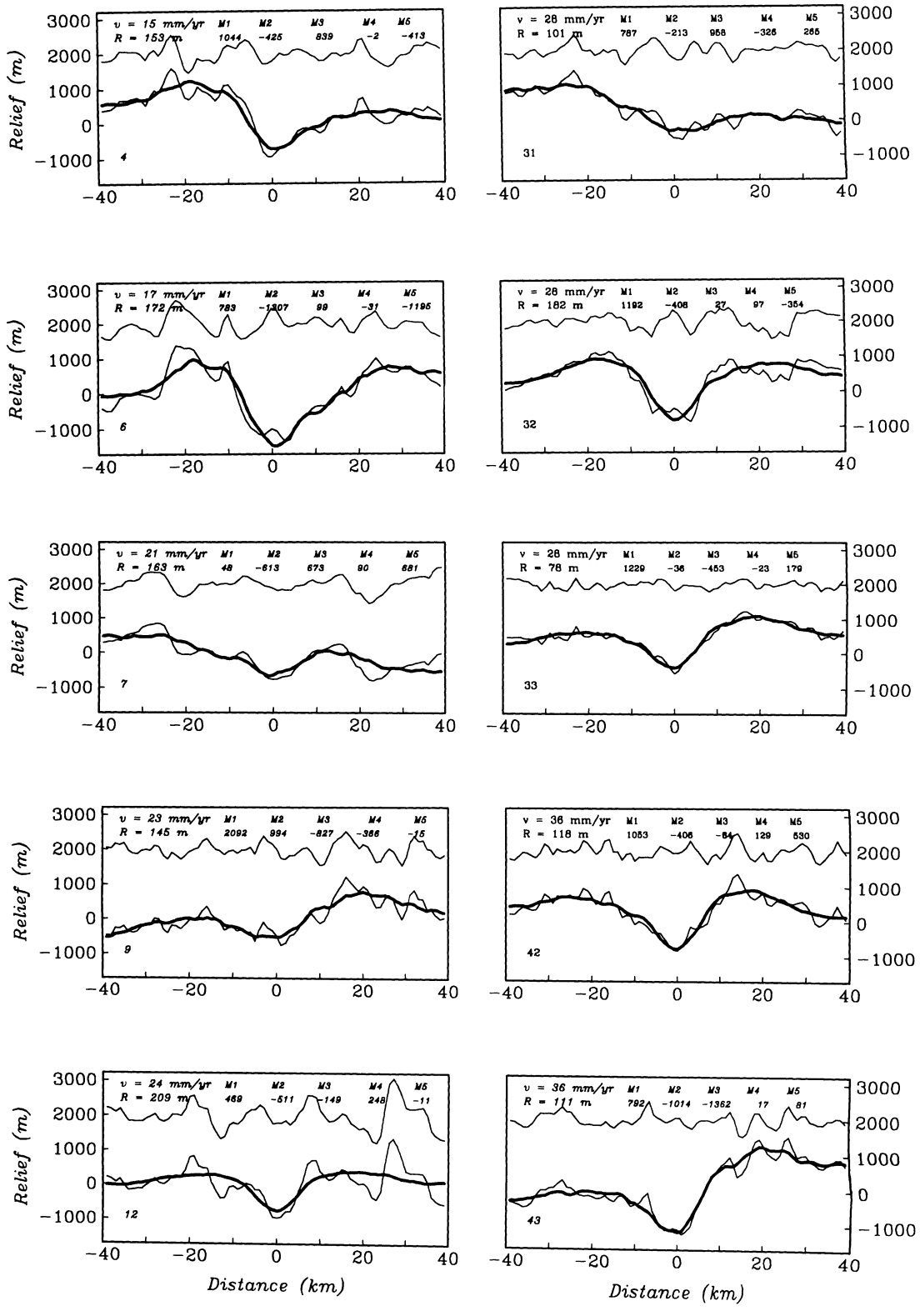

Figure A7. Examples of individual profiles as represented by the five primary EOFs. The heavy line shows the linear combination of the first five modes for each profile. The original profile is superimposed and the residual profile is plotted above. The coefficients of the first five modes are shown as well as the spreading rate and MAD of the residual profile.

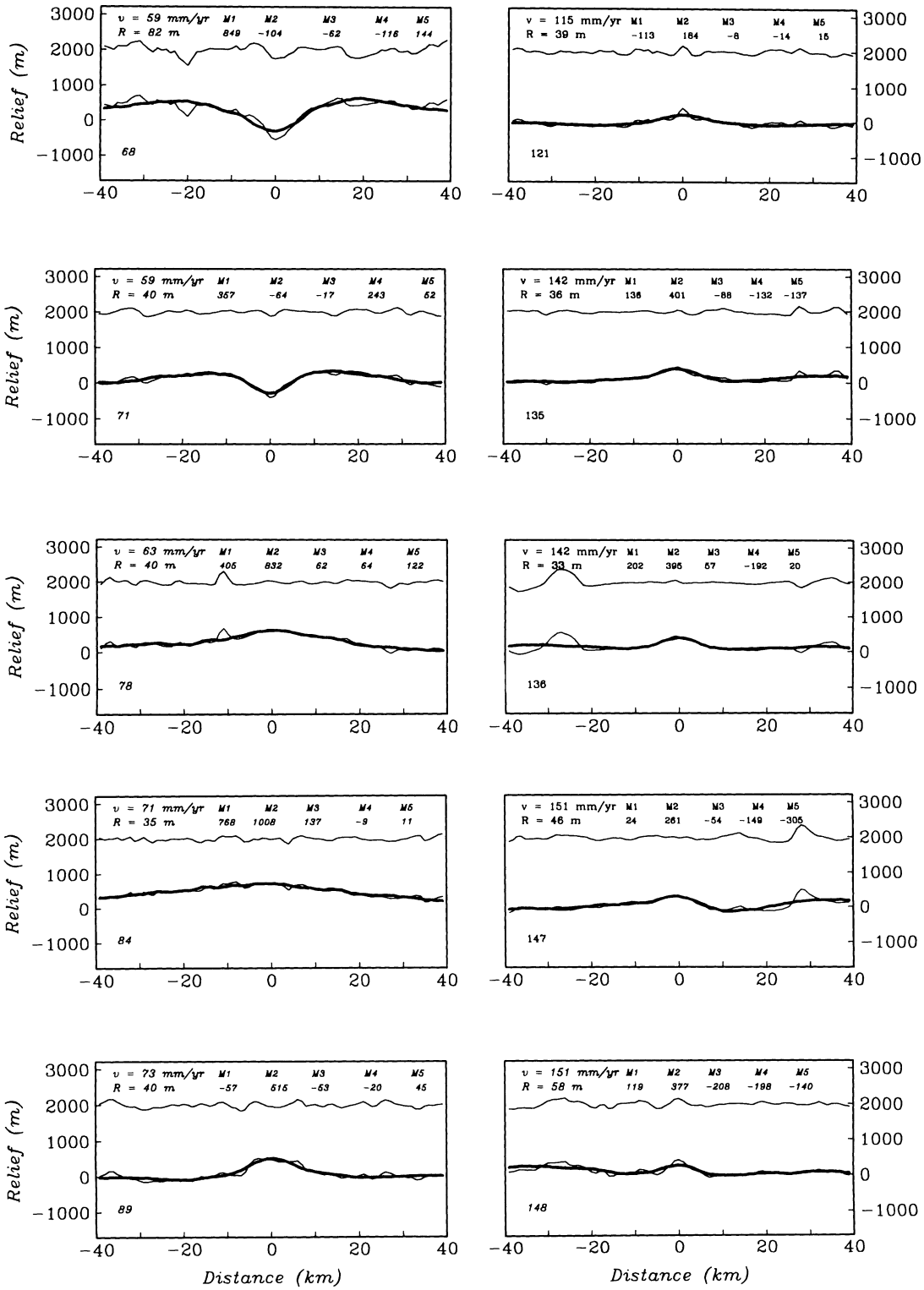

Figure A7. (*Continued.*)

length scale would not accommodate some of the wider axial valleys while a longer length scale would eliminate a significant number of shorter profiles from the data set. The global analysis described above was repeated with profile lengths 60 and 100 km. As shown in Fig. A5, the central 60 km of the three primary modes are nearly identical. The distribution of singular values is also almost indistinguishable. Using much longer profiles would undoubtedly change the results of the analysis. At longer wavelengths, sea-floor depth is dominated by thermal subsidence, and axial morphology becomes negligible. While the relationship of axial morphology to thermal subsidence has yet to be understood, such a study would require a larger data base of long, flowline oriented profiles than is presently available.

Sensitivity of the global analysis to variations in the input data set was also tested. The 156 profiles were divided into three distinct (non-intersecting) subsets, evenly distributed with respect to spreading rate, and three separate global analyses were performed. The results are shown in Fig. A6. As in the previous example, the primary modes and the spectrum of singular values are nearly identical to the global analysis. The only significant difference is in the axial region of the third mode. It is surprising that the results of three completely separate analyses on significantly smaller data sets are so similar given the amount of variability seen in the profile data. This result is encouraging because it implies that the addition of significant amounts of new data is unlikely to change the fundamental results of the global analysis.

Examples from the global data set

Since it is not practical to show decompositions for all 156 profiles used in this study, only the most instructive are included here (Fig. A7). Each profile is indexed by the number used in Table 1. For each profile, the raw data, interpolated to 1 km sample spacing are shown. Superimposed in bold on this profile is the corresponding linear combination of the first five modes. Plotted above is the residual profile. Also shown is the spreading rate, the MAD of the residual profile and the coefficients of the first five modes. The profiles are arranged in increasing spreading rate.

The first 15 profiles are taken from ridges with spreading rates less than 80 mm yr^{-1}, the remaining profiles are taken from faster spreading ridges. Examination of these profiles verifies three significant points: there is a marked difference in variability of fast and slow spreading ridge structures; the first five modes generally fit the salient features of the profiles very well; and the amplitudes of the residual profiles are generally consistent along the length of the profile and are usually not related to a significant misfit of the axial structure. Slow spreading ridges show considerably greater variability in both the large scale axial form (depth, asymmetry, etc.) and in amplitude of residual profiles. Profiles, 7, 9 and 12 are all taken from the northern Mid-Atlantic Ridge and are spreading at approximately the same rate but are not at all similar in character. On several of the slow spreading profiles the axial valley is obscured by shorter wavelength features. On more than half of the slow spreading profiles there is significant asymmetry as well. It would be very difficult to characterize most of these profiles using analytic functions. On two of the profiles shown (12 and 32) the axial morphology is poorly fit by the first five modes. These are the two worst examples from the data set. In general the first five modes provide an exceptional representation of the raw data. Examination of the residual profiles indicates that they maintain a relatively constant character along their length. It is also encouraging that off-axis seamounts are effectively included in the residual profiles.

Imaging mid-ocean ridge transitions with satellite gravity

Christopher Small
David T. Sandwell
Scripps Institution of Oceanography, La Jolla, California 92093

ABSTRACT

Gravity maps derived from satellite altimeter measurements provide unprecedented medium-resolution coverage of sparsely surveyed mid-ocean ridges in the southern oceans. A spectral analysis of 76 000 km of coincident shipboard and satellite gravity measurements shows that satellite altimeters can accurately resolve features with half-wavelengths as short as 13 km. The coverage and resolution of these gravity data allow us to determine accurately both the location of poorly charted ridge axes and the variation in axial anomaly character along the ridge axis, although their detailed morphology is not resolved. The results of this study support earlier studies that showed a transition from spreading-rate–dependent axial gravity lows to rate-independent axial highs with increasing spreading rate. Four such transitions are imaged on the Southeast Indian Ridge and Pacific Antarctic Ridge. We expect that these transitions are the result of a temperature-sensitive threshold phenomenon and may be influenced by nearby hot spots.

INTRODUCTION

The radically different morphology of fast- and slow-spreading mid-ocean ridges is one of the earliest observations of seafloor structure, but it has yet to be fully understood. Heezen (1960) and Menard (1960) observed that the slow-spreading Mid-Atlantic Ridge is marked by a 1–3-km-deep axial valley with flanking rift valley mountains and rough topography, whereas the faster spreading East Pacific Rise generally consists of a more continuous axial ridge with smoother flanking topography (Fig. 1). The fast- and slow-spreading end members of the continuous mid-ocean ridge system have been studied extensively (e.g., Macdonald, 1986; Lonsdale, 1989) but the more remote intermediate-rate ridges have been largely overlooked.

Satellite altimeters provide medium-resolution gravity data with nearly complete coverage of the global mid-ocean ridge system. Recently declassified Geosat Geodetic Mission altimeter data provide exceptionally dense spatial coverage (2–4 km track spacing) of the oceanic areas south of lat 30°S. These remote southern oceans contain a significant part of the global mid-ocean ridge system and have not been adequately surveyed since the introduction of multi–narrow-beam echosounders such as Seabeam, Hydrosweep, and Seabeam 2000. In this paper we discuss the nature of morphologic transitions on intermediate-spreading-rate ridges in the southern oceans and the constraints offered by satellite gravity data.

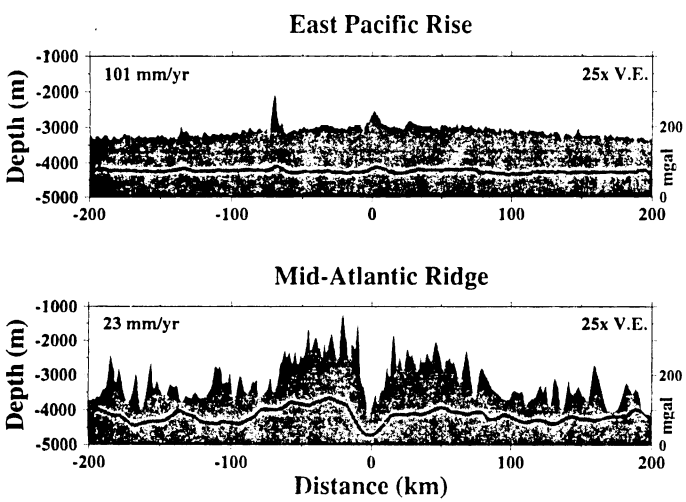

Figure 1. Typical ridge-axis bathymetry and gravity anomalies (heavy line) across fast- and slow-spreading mid-ocean ridges.

SATELLITE GRAVITY

Because the height of the ocean's surface above a reference corresponds to a gravitational equipotential, sea surface elevations measured by satellite altimeters may be used to produce geoid (Rapp, 1983) and gravity (Haxby et al., 1983) maps of the world's ocean basins. The method used to construct the gravity grids, described in detail by Sandwell (1992), allows data from the Seasat, Geosat, and ERS-1 satellite missions to be combined to give maximum spatial coverage. In addition, the very dense spatial coverage of recently declassified Geosat GM data allows much higher resolution of the gravity field in the areas south of 30°S.

Although satellite altimeters have lower spatial resolution than shipboard gravimeters, satellites provide superior areal coverage and are able to resolve large- and intermediate-scale features of the marine gravity field. Shipboard and satellite gravity profiles are shown for comparison in Figure 2A. The solid line shows the free-air anomaly as measured by a gravimeter on the USS *Eltanin* in the Indian Ocean in 1971. The dashed line represents the free-air anomalies interpolated from the satellite gravity grid along the same profile. It is apparent that the satellite data accurately resolve the salient features seen in the shipboard profile but do not resolve the shortest wavelength, low-amplitude features. Before using the satellite gravity data for detailed studies, it is necessary to quantify this agreement.

In order to quantitatively compare the resolution of the two types of gravity measurements, we performed a spectral analysis on 76 000 km of coincident shipboard and satellite measurements in the southern oceans. Although we used the highest quality data available, most of the data in the southern oceans were collected before Global Positioning Satellite navigation was available and may con-

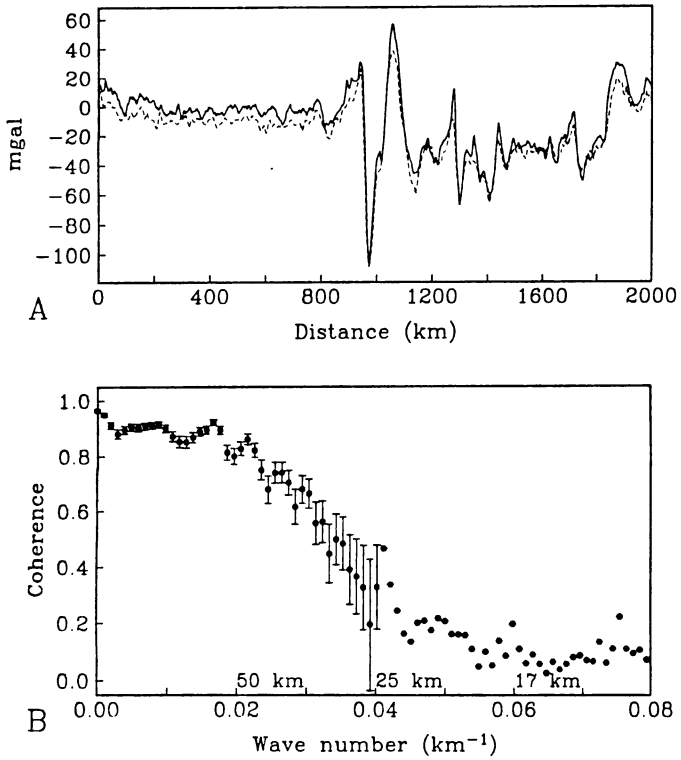

Figure 2. Comparison of coincident satellite and shipboard free-air gravity measurements. A: On profiles, satellite data (dashed line) resolve all but smallest features seen in ship data (solid line). Thickened line shows location of profile in Figure 3 (at ~90°E). B: Spectral coherence of 76 000 km of coincident ship and satellite gravity measurements shows very high agreement (>0.5) for anomalies with wavelengths longer than ~35 km.

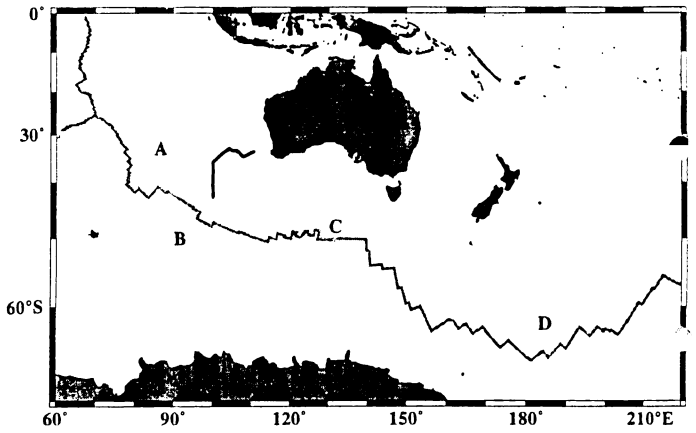

Figure 3. Index map for areas considered in this study. Thick gray line marks mid-ocean ridge system. Shaded boxes show locations of maps in Figure 5.

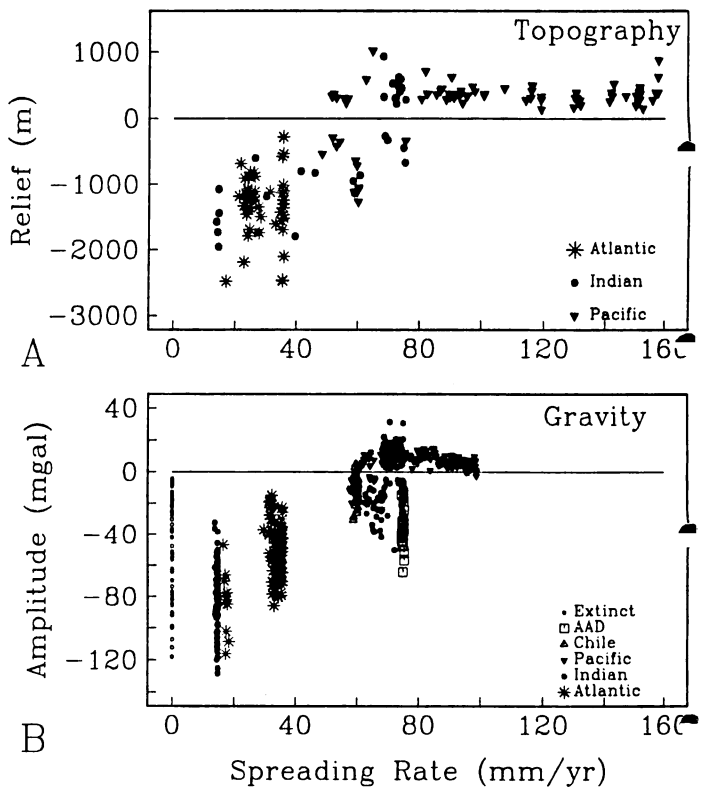

Figure 4. Variation of ridge-axis morphology and gravity anomaly with spreading rate. A: Axial topographic relief vs. spreading rate from Small (1993). B: Axial gravity-anomaly amplitude measured at 646 locations on ridges south of lat 30°S. Note coincident change in polarity and rate dependence between 60 and 80 mm/yr.

tain significant errors (~5 mgal) associated with poor navigation and unmodeled turns. It is known that high-quality shipboard gravity measurements generally have greater spatial resolution than satellite gravity measurements (Small and Sandwell, 1992; Neumann et al., 1993) so in this study we use the shipboard data as ground truth. The resolution of the satellite data for different wavelength anomalies is given by the spectral coherence (Bendat and Piersol, 1986); high coherence (>0.5) indicates good agreement between the two data sets. The satellite and shipboard data both accurately resolve anomalies with wavelengths longer than ~35 km but become increasingly incoherent at shorter wavelengths (<25 km) (Fig. 2B). If half-wavelengths as short as 13 km can be accurately resolved, then the gravity anomaly of a small axial rise should be recoverable, and the broader, larger amplitude axial-valley anomaly should be easily recognized in the satellite data (see Fig. 5).

SPREADING RATE DEPENDENCE

The remote locations of most intermediate-spreading-rate ridges on the primary ridge system (Fig. 3) have so far precluded a thorough understanding of the factors controlling axial morphology. In a survey of the morphology and tectonics of the Mid-Atlantic Ridge, Macdonald (1986) compiled estimates of axial-valley relief on several ridges and concluded that the axial valley disappears gradually, at spreading rates between 50 and 90 mm/yr.

More detailed analyses of available underway bathymetry data and satellite altimeter profile data have indicated that transitions from slow- to fast-spreading ridge axis morphology occur in a fairly narrow range of intermediate spreading rates. In a global study of ridge-axis gravity anomalies using Geosat Exact Repeat Mission profiles, we found that gravity anomaly amplitude decreases with increasing spreading rate on slow-spreading ridges, whereas anomaly amplitude remains relatively constant on fast-spreading ridges, Small and Sandwell (1989). The transition from rate dependence to rate independence coincides with a polarity transition from the gravity lows characteristic of slow-spreading ridges to gravity highs seen at fast-spreading ridges. The satellite coverage now available allows us to determine more accurately the location of the ridge axis,

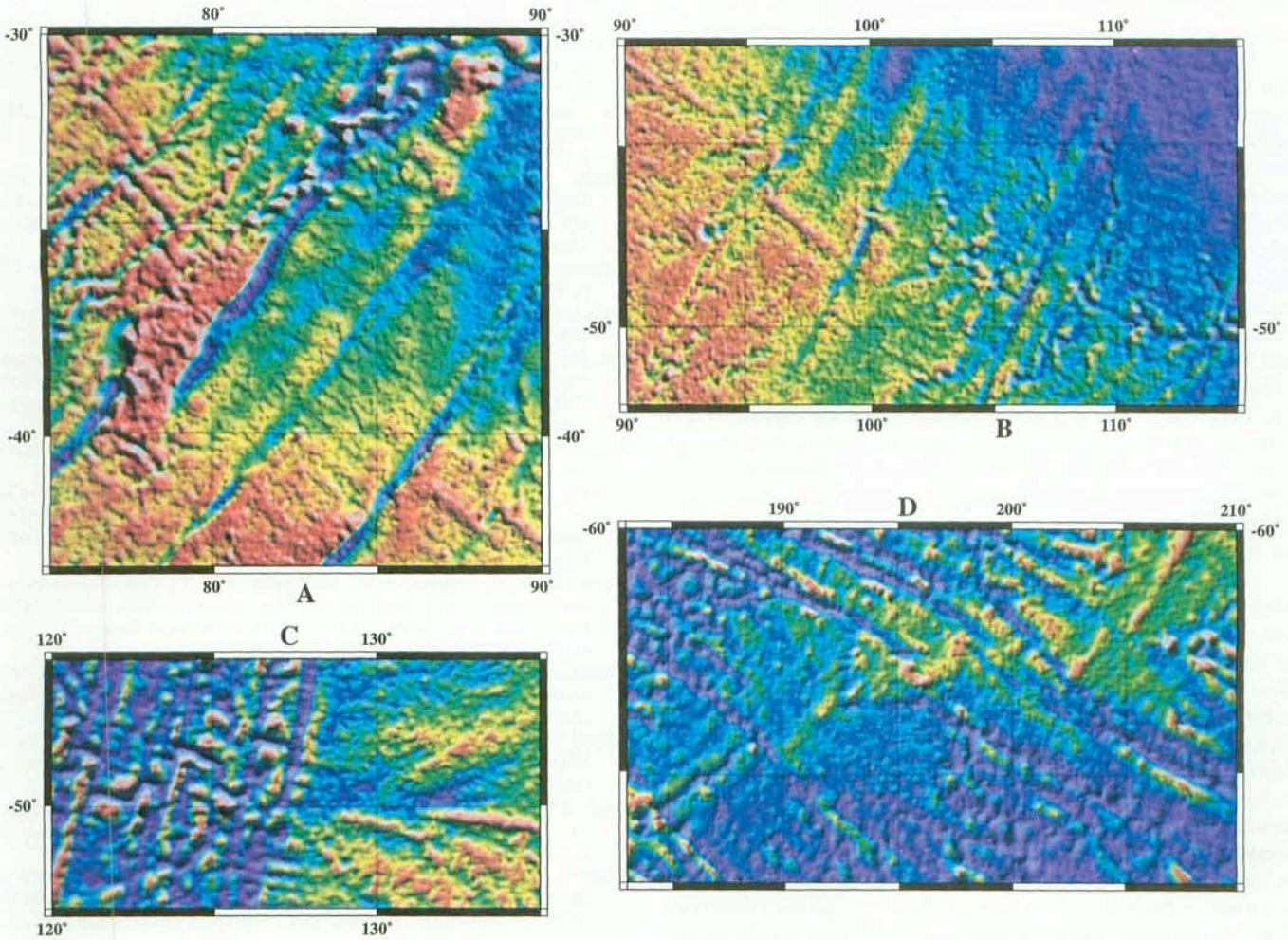

Figure 5. Examples of ridge-axis transitions on ridges in southern oceans. Each satellite gravity map shows anomaly amplitude ranging from −20 mgal (purple) to 20 mgal (red). In each region ridge axis changes from linear gravity high, characteristic of fast-spreading ridges, to linear low with flanking highs, typical of slow-spreading ridges. Spreading-rate ranges are (A) 62–72 mm/yr, (B) 72–75 mm/yr, (C) 73–75 mm/yr, and (D) 56–72 mm/yr.

thereby greatly reducing the chance of errors in estimates of the location and polarity of the axial anomaly.

Although the marine gravity field is affected by seafloor density variations and subseafloor structure, at short wavelengths ($\lambda < \sim 100$ km) it is controlled by seafloor morphology (Cochran, 1979). For this reason, changes in the nature of the ridge-axis gravity anomaly are assumed to correspond to changes in the morphology. Detailed global studies of available ridge-axis bathymetry profiles by Small (1993) and Malinverno (1993) support our previous findings (Small and Sandwell, 1989) (Fig. 4A).

The spatial coverage offered by the recently declassified satellite gravity data is a significant improvement over the previously available distribution of ship tracks and widely spaced satellite tracks. To give a more complete picture of the nature of the transition from slow- to fast-spreading structure, 646 ridge-perpendicular gravity profiles have been analyzed along the entire ridge system south of 30°S. The method described by Small (1993) was used to measure peak to trough amplitudes for axial gravity anomalies (Fig. 4B). As in previous studies we find a transition in the polarity and rate dependence of the ridge-axis anomalies at spreading rates between 60 and 80 mm/yr. The coverage offered by the satellite data gives us a significant advantage over previous studies and provides not only a continuous set of profiles for every ridge segment in the study area but also a more detailed knowledge of the location of the ridge axis than was previously available.

INTERMEDIATE-RATE TRANSITIONS

Satellite gravity maps provide the first detailed look at the nature of intermediate-spreading-rate transitions in the southern oceans (Fig. 5). Although the smaller ridge-axis anomalies are near the limit of the resolution for the satellite gravity data, it is apparent from Figure 5 that the anomalies are generally well resolved and that the characteristics of fast- and slow-spreading ridges can be distinguished. In these images the axial valleys, characteristic of slow-spreading ridges, are indicated by linear gravity lows flanked on either side by gravity highs. Axial ridges, characteristic of fast-spreading ridges, are shown by smaller amplitude, linear gravity highs. A SeaMARC II survey of the region shown in Figure 5C (Palmer et al., 1993) supports these interpretations.

Although these transitions from slow- to fast-spreading-rate structure occur within a narrow range of spreading rates, Figure 5 indicates that it may not always be spatially abrupt. In most cases there appears to be a small region, between the well-defined axial high and axial low, where a ridge-axis anomaly is not apparent. The

absence of abrupt spatial transitions in the gravity data may accurately reflect the nature of the seafloor morphology in these areas, or it may result from the limited resolution of the satellite altimeter.

It is apparent that the transition from slow- to fast-spreading structure is not controlled by spreading rate alone. Well-known exceptions to the patterns shown in Figure 4 exist on the slow-spreading Reykjanes Ridge and in the faster spreading Australian-Antarctic Discordance. The Southeast Indian Ridge contains several potential transition areas that all have essentially the same spreading rate (70–75 mm/yr). It seems likely that the thermal structure at the ridge axis, which is controlled primarily by spreading rate, would exert the ultimate control on the morphology. Phipps Morgan and Chen (1993) discussed in greater detail the importance of thermal structure and crustal thickness on ridge-axis morphology. At a single spreading rate, local temperature variations may be considered perturbations to the large-scale thermal structure, which is controlled by spreading rate. This would suggest that ridge-axis morphology is controlled by a threshold phenomenon that is sensitive to relatively small changes in temperature (Small and Sandwell, 1989). A possible candidate for such a threshold mechanism was proposed by Chen and Morgan (1990), but more detailed surveys of transitions will be necessary to test their model.

A factor influencing the nature of the transitions may be the proximity of hot spots and the availability of melt at the ridge axis. Asthenosphere produced at nearby hot spots may be channeled to the ridge, as proposed by Vogt and Johnson (1975), where it may affect the process of crustal accretion, indirectly controlling the axial morphology. Royer and Schlich (1988) discussed the influence of the Amsterdam–St. Paul hot spot on the ridge axis in the immediate vicinity of the hot spot. Lava dredged from the ridge axis in this area have been shown to be geochemically related to both the Amsterdam–St Paul and Kerguelen hot spots (Michard et al., 1986). If asthenosphere migrates to the axis of the Southeast Indian Ridge along the unnamed fracture zone that intersects the axis near long 86°E, then it may contribute to the robust axial gravity high seen to the east of the fracture zone. Similar arguments may be made for the shrinking and eventual disappearance of the axial high on the Pacific Antarctic Rise south of the Louisville hot spot (Fig. 5D). The axial gravity anomaly also changes near the Bouvet Triple Junction on the Mid-Atlantic Ridge, although a typical fast-spreading anomaly never develops. An understanding of the transitions will require detailed surveys of these areas, for which the satellite gravity data will be an important reconnaissance tool.

CONCLUSIONS

Gravity maps derived from satellite data provide the first detailed look at many mid-ocean ridges in the southern oceans. The satellite gravity measurements used in this study accurately resolve features with half-wavelengths longer than 13 km, thereby allowing the location of the ridge axis to be mapped in much greater detail than was previously possible. Amplitude and polarity measurements of ridge-axis gravity anomalies in the southern oceans agree with results of previous studies that showed a transition from spreading-rate-dependent structure to rate independence at intermediate spreading rates (60–80 mm/yr). Examples of these transitions are seen on the Southeast Indian Ridge and the Pacific Antarctic Ridge. Although geophysical and petrologic data are sparse in these transitional areas, we believe that the morphology is controlled by thermal structure, which may be strongly influenced by asthenosphere derived from nearby hot spots.

REFERENCES CITED

Bendat, J.S., and Piersol, A.G., 1986, Random data, analysis and measurement procedures (second edition): New York, John Wiley & Sons.

Chen, Y., and Morgan, W.J., 1990, Rift valley/no rift valley transition at mid-ocean ridges: Journal of Geophysical Research, v. 95, p. 17,571–17,583.

Cochran, J.R., 1979, An analysis of isostasy in the world's oceans: 2, Mid-ocean ridge crests: Journal of Geophysical Research, v. 84, p. 4713–4729.

Haxby, W.F., Karner, G.D., LaBrecque, J.L., and Weissel, J.K., 1983, Digital images of combined continental and oceanic data sets and their use in tectonic studies: Eos (Transactions, American Geophysical Union), v. 64, p. 995–1004.

Heezen, B.C., 1960, The rift in the ocean floor: Scientific American, v. 203, p. 99–110.

Lonsdale, P., 1989, Segmentation of the Pacific Nazca spreading center, 1°N–20°S: Journal of Geophysical Research, v. 94, p. 12,197–12,225.

Macdonald, K.C., 1986, The crest of the Mid Atlantic Ridge: Models for crustal generation and tectonics, *in* Vogt, P.R., ed., The western North Atlantic region: Boulder, Colorado, Geological Society of America, Geology of North America, v. M, p. 51–68.

Malinverno, A., 1993, Transition between a valley and a high at the axis of mid-ocean ridges: Geology, v. 21, p. 639–642.

Menard, H.W., 1960, The East Pacific Rise: Science, v. 132, p. 1737–1746.

Michard, A., Montigny, R., and Schlich, R., 1986, Geochemistry of the mantle beneath the Rodriguez triple junction and Southeast Indian Ridge: Earth and Planetary Science Letters, v. 78, p. 104–114.

Neumann, G.A., Forsyth, D.W., and Sandwell, D.T., 1993, Comparison of marine gravity from shipboard and high-density satellite altimetry along the Mid-Atlantic Ridge, 30.5°–35.5°S: Geophysical Research Letters, v. 20, p. 1639–1642.

Palmer, J., Sempère, J.C., Christie, D.M., Phipps Morgan, J., 1993, Morphology and tectonics of the Australian-Antarctic discordance between 123°E and 128°E: Marine Geophysical Researches, v. 15, p. 121–152.

Phipps Morgan, J., and Chen, Y.J., 1993, The genesis of oceanic crust: Magma injection, hydrothermal circulation, and crustal flow: Journal of Geophysical Research, v. 98.

Rapp, R.H., 1983, The determination of geoid undulations and gravity anomalies from Seasat altimeter data: Journal of Geophysical Research, v. 88, p. 1552–1562.

Royer, J.Y., and Schlich, R., 1988, Southeast Indian Ridge between the Rodriguez triple junction and the Amsterdam and St. Paul islands: Detailed kinematics for the past 20 m.y.: Journal of Geophysical Research, v. 93, p. 13,524–13,550.

Sandwell, D.T., 1992, Antarctic marine gravity from high density satellite altimetry: Geophysical Journal International, v. 109, p. 437–448.

Small, C., 1993, A quantitative analysis of mid-ocean ridge axial topography: Geophysical Journal International.

Small, C., and Sandwell, D.T., 1989, An abrupt change in ridge axis gravity with spreading rate: Journal of Geophysical Research, v. 94, p. 17,383–17,392.

Small, C., and Sandwell, D.T., 1992, A comparison of satellite and shipboard gravity measurements in the Gulf of Mexico: Geophysics, v. 57, p. 885–893.

Vogt, P.R., and Johnson, G.L., 1975, Transform faults and longitudinal flow below the midoceanic ridge: Journal of Geophysical Research, v. 80, p. 1399–1428.

Manuscript received August 4, 1993
Revised manuscript received November 9, 1993
Manuscript accepted November 22, 1993

This chapter, in full is a reprint of the material as it appears in *Geology*, V22, 1994. The dissertation author is the primary investigator and author of this paper.

Chapter 5

A Comparison of Satellite and Shipboard Gravity Measurements in the Gulf of Mexico

Christopher Small and David T. Sandwell

Scripps Institution of Oceanography
University of California San Diego
La Jolla, CA 92093

Submitted to *Geophysics*
July 31, 1991
Accepted December 23, 1991
Published July 1992

GEOPHYSICS, VOL. 57, NO. 7 (JULY 1992); P. 885–893, 7 FIGS.

A comparison of satellite and shipboard gravity measurements in the Gulf of Mexico

Christopher Small* and David T. Sandwell*

ABSTRACT

Satellite altimeters have mapped the marine geoid over virtually all of the world's oceans. These geoid height measurements may be used to compute free air gravity anomalies in areas where shipboard measurements are scarce. Two-dimensional (2-D) transformations of geoid height to gravity are limited by currently available satellite track spacing and usually sacrifice short wavelength resolution. Full resolution may be retained along widely spaced satellite tracks if a one dimensional (1-D) transformation is used. Although the 1-D transform retains full resolution, it assumes that the gravity field is lineated perpendicular to the profile and is therefore limited by the orientation of the profile relative to the field. We investigate the resolution and accuracy of the 1-D transform method in the Northern Gulf of Mexico by comparing satellite gravity profiles with high quality shipboard data provided by Edcon Inc. The long wavelength components of the gravity field are constrained by a low degree reference field while the short wavelength components are computed from altimeter profiles. We find that rms misfit decreases with increasing spherical harmonic degree of the reference field up to 180 degrees ($\lambda > 220$ km) with negligible improvement for higher degrees. The average rms misfit for the 17 profiles used in this study was 6.5 mGal with a 180 degree reference field. Spectral coherence estimates indicate that the satellite data resolve features with wavelengths as short as 25 km.

INTRODUCTION

In recent years, satellite altimeters have mapped the marine gravity field in remarkable detail (Haxby, 1987). Satellites such as Geos-3, Seasat, and Geosat use microwave radar to make high precision (±2 cm vertical) measurements of the sea surface height relative to a reference ellipsoid. In the absence of disturbing forces such as tides, currents, and waves, the sea surface conforms to the geoid or gravitational equipotential surface. The short wavelength components of these geoid height profiles have been used to map fracture zones, seamounts, hotspot chains, midocean ridges and a multitude of previously undiscovered features in the worlds oceans. [See Sandwell (1991) for a review of applications.] Satellite altimeter data have also been used to map continental margin structure, particularly in remote areas where little shipboard data are available (Bostrom, 1989).

For many of these applications it is desirable to compute gravity anomalies from geoid heights so the satellite data can be compared and combined with shipboard gravity measurements. The two-dimensional (2-D) Stokes' integration formula (e.g., Heiskanen and Moritz, 1967) is commonly used to compute geoid height from the gravity anomaly, and it is straightforward to invert the Stokes formula to compute the gravity anomaly directly from geoid height. An alternate approach is to expand the geoid height in spherical harmonics, multiply each of the coefficients by a known factor, and sum the new series to construct gravity anomaly (Rapp and Pavlis, 1990; Haxby et al., 1983). From this theory it is clear that geoid height and gravity anomaly are equivalent measurements of the earth's external gravity field.

In practice, there are several problems that must be addressed when converting satellite altimeter profiles of geoid height to marine gravity anomalies. The first problem is to measure geoid height with sufficient precision to resolve short wavelength ($<\sim 100$ km) gravity anomalies. As shown below and in a previous study (Sandwell and McAdoo, 1990), such high-resolution profiles are now available from the Geosat Exact Repeat Mission (Geosat/ERM). The more severe problems are related to data coverage and sampling of the geoid height since the 2-D inverse Stokes function must be integrated over the entire surface of the earth to construct

Manuscript received by the Editor July 31, 1991; revised manuscript received December 23, 1991.
*Scripps Institute of Oceanography, University of California at San Diego, LaJolla, CA 92093.

gravity anomalies. An edge effect problem occurs because satellite altimeter measurements of geoid height are only available over ocean areas. Since the inverse Stokes kernel falls off rapidly with distance, the integration is quite accurate in the open ocean areas but becomes less accurate when gravity is computed near land. This edge effect problem can only be solved by including land gravity or geoid height measurements in the integration.

A related problem is that satellite altimeter profiles are only available along widely spaced ground tracks (Figure 1). Even when one attempts to compute the gravity anomaly along one of the satellite tracks, the recovery will be inaccurate because the 2-D integration will include points where there are no actual geoid height measurements. It is possible to interpolate the geoid height in the gaps but this reduces the accuracy and resolution of the resulting gravity values.

In the past, there have been two approaches to the recovery of gravity anomalies from local geoid height measurements. The first approach is to construct gridded gravity anomaly maps (Haxby et al., 1983; Sandwell, 1991) from an interpolated geoid height grid. Over a limited area (e.g., 4000 km × 4000 km) conversion from geoid height to gravity is most easily accomplished by first removing long wavelength components from the geoid height using a low degree spherical harmonic model, then transforming the short wavelength geoid height to gravity anomaly using a 2-D Fourier transform. This assumes that the earth is flat for length scales less than the wavelength of the highest spherical harmonic, typically 1000 km. After computing the short wavelength gravity anomaly, the long wavelength gravity anomaly from the spherical harmonic model is replaced. As noted above, the major problem with this method is that the shortest wavelength anomalies are smoothed during the interpolation and Fourier transformation. To retain full resolution along track with the 2-D method, it is necessary to produce a grid with a cell size comparable to the along-track sampling spacing. This results in an enormous increase in computational labor to compute anomalies in the regions between tracks where there is no information. The along-track resolution may be retained more easily if a one-dimensional (1-D) transformation is applied to the profile data, thereby avoiding the smoothing inherent in the gridding process (Roest, 1987). The disadvantage is that the 1-D transformation from geoid height to gravity assumes that the gravity field is lineated perpendicular to the trackline. If, for example, a profile crosses perpendicular to the strike of a straight continental margin then the method gives the correct answer. However, if the profile crosses at some other angle, the amplitude of the calculated anomaly will be less than the true amplitude.

While the accuracy and resolution of geoid height measurements has been established for Geosat (Sandwell and McAdoo, 1990), the ability of 1-D transform techniques to compute free air gravity anomalies has not. In this study, we investigate the accuracy and resolution of the 1-D approach. This is done by comparing 17 satellite gravity profiles with conventional shipboard gravity data from the northern Gulf of Mexico. The Gulf is a particularly good area to test the 1-D method because an extremely high quality shipboard data set has been compiled by Edcon, Inc. Although the satellite data cannot equal the short wavelength resolution of

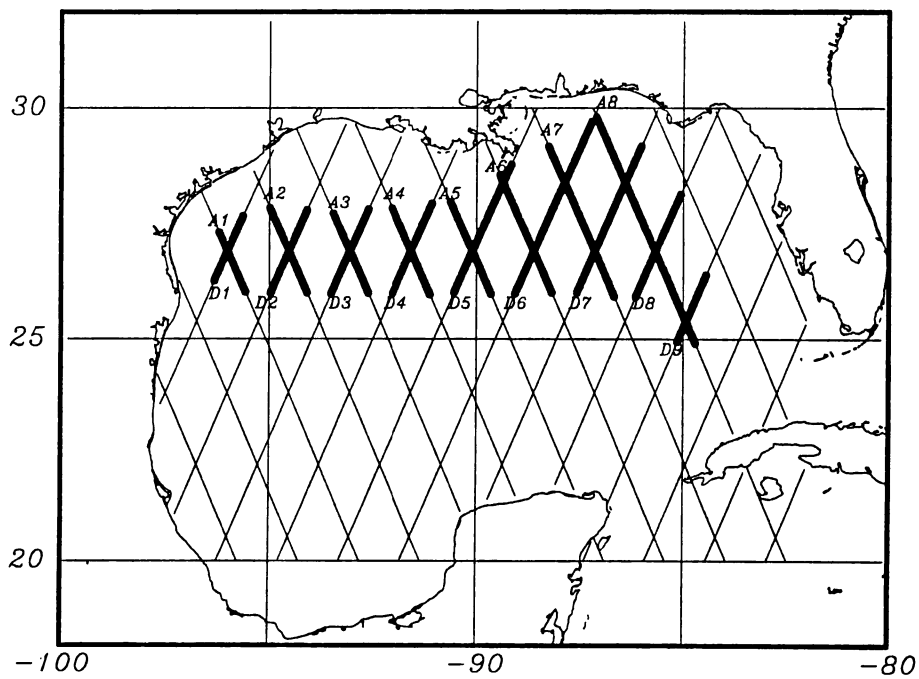

FIG. 1. Index map showing location of profiles used in this study. Long thin lines are satellite tracks with 3.4 km sampling interval. Short thick lines indicate regions of available shipboard coverage. Shipboard data are interpolated from a 6000′ grid along satellite tracks with an 0.5 km sample spacing. Ascending profiles are labeled A1-A8 and descending profiles are labeled D1-D9.

the shipboard data, we obtain excellent agreements between the satellite gravity and the shipboard gravity at intermediate wavelengths ($25 < \lambda < 500$ km) if a spherical harmonic model is used as a reference field.

GEOSAT AND SHIPBOARD GRAVITY DATA

The satellite altimeter data used in this study consist of 17 profiles in the Gulf of Mexico, 8 ascending profiles (running southeast to northwest) and 9 descending profiles (running northeast to southwest). These satellite tracks are shown in Figure 1 as long, thin lines. The satellite data were collected by the Geosat spacecraft during its Exact Repeat Mission (Geosat/ERM) where every 17 days it repeated its ground track to a tolerance of ±1 km. The first 44 repeat cycles (2-years of data) were averaged to improve the accuracy and resolution of the data. This averaging procedure is described in Sandwell and McAdoo (1990), so only a brief summary is given here.

Satellite altimeter measurements of geoid height contain long wavelength orbit errors (~1 m) which greatly exceed the short wavelength precision of the measurements (~2 cm). Because of this long wavelength error, it is not possible to simply average the repeat profiles without first applying some sort of correction or high-pass filter. We adopted the high-pass filter approach where the first step in the data processing was to differentiate each profile. This effectively suppresses the long wavelength orbit error and results in sea surface slope profiles (also called vertical deflections). After differentiation, individual profiles were averaged (Figure 2, upper plot) to increase the signal-to-noise ratio and also minimize the time varying components of sea surface topography caused by unmodeled tides and ocean currents.

After averaging, the accuracy and resolution of the data were estimated by comparing repeat profiles (Sandwell and McAdoo, 1990). The uncertainty in the averaged profile was calculated as the standard deviation of the individual profiles about the mean (Figure 2, lower plot). In open ocean areas and at low latitudes, the uncertainty is generally less than 1 μrad. In enclosed bodies of water, such as the Gulf of Mexico, the uncertainty is slightly higher (~1.5 μrad) because not all of the 44 profiles are available for averaging; in this case only about 25 out of 44 are available.

The second method of estimating the accuracy of the profiles was to average one year of profiles (up to 22) and compare this average with the average for the second year. In general, these independent averages have a mean difference of less than 0.05 μrad and an rms difference of less than 1.5 μrad (Sandwell and McAdoo, 1990). The resolution of the profiles was estimated through a coherence analysis where the first year average is crosscorrelated with the second year average. Results show that over most ocean areas, these altimeter data can resolve wavelengths as short as 20 km.

The shipboard gravity data were provided by Edcon Inc. for the region shown in Figure 1 (short thick lines). The shipboard profiles were interpolated from a densely gridded gravity map having a 6000 ft (1829 m) point spacing. The grid was produced from a series of shipboard profiles collected with a LaCoste Romberg S type gravimeter. The original shipboard gravity profiles were adjusted at crossover points; the mean crossover error for the entire grid was 1.55 mGal before correction and 0.4 mGal after correction. Based on our experience with deep ocean shipboard gravity data, these Gulf of Mexico data represent perhaps the best ocean gravity survey available. We treat these data as "ground truth" since it is expected that their accuracy and resolution are superior to the satellite altimeter profiles.

THEORY AND DATA PROCESSING

A modified version of the Fourier transform method described briefly in Haxby et al., (1983), Roest (1987), and McAdoo et al. (1990) was used to compute along-track gravity anomalies from along-track vertical deflections. To retain the along-track resolution and simplify the computations, a flat-earth approximation was used for the short wavelength part of the transformation. To retain the long wavelength accuracy of the gravity profile, a spherical

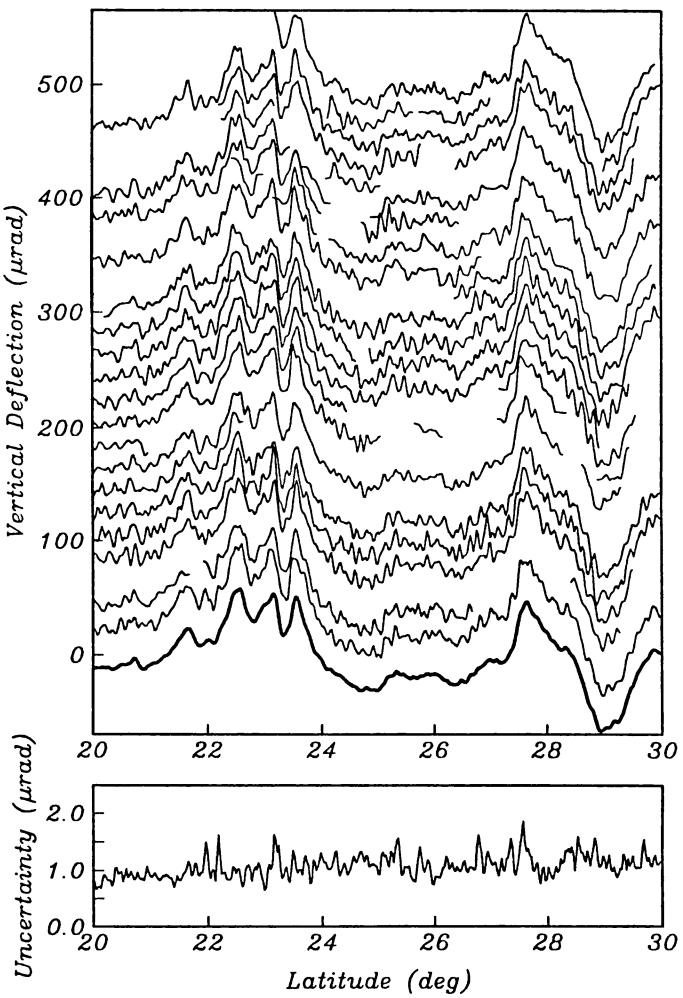

FIG. 2. Example of stacking procedure. Individual vertical deflection profiles (upper curves) are stacked to produce an average profile (heavy curve). The standard deviation at each point provides a measure of the uncertainty in the profile (bottom curve). Oceanographic effects and data gaps result in a higher than average uncertainty (~1 μRAD) FOR THIS PROFILE.

harmonic model is subtracted from the vertical deflection profiles before the along-track gravity is computed. Finally, the gravity anomaly computed from the same spherical harmonic model is added back to the along-track gravity profiles. Here we describe the 1-D transformation method in detail.

To begin, one must relate the geoid height $N(\mathbf{x})$ and other measurable quantities such as gravity anomaly $\Delta g(\mathbf{x})$ to the gravitational potential $\phi(\mathbf{x}, z)$. In the following equations, the bold $\mathbf{x}$ denotes the coordinate (x, y); similarly $\mathbf{k}$ denotes (k_x, k_y) where $k_x = 1/\lambda_x$ where λ_x is wavelength.

Using Brun's formula, we define the following quantities

— Geoid Height,

$$N(\mathbf{x}) = \frac{1}{g}\,\phi(\mathbf{x}, 0) \tag{1}$$

— Gravity Anomaly,

$$\Delta g(\mathbf{x}) = -\frac{\partial \phi}{\partial z}\,(\mathbf{x}, 0) \tag{2}$$

— Vertical Deflection, East Component,

$$\eta(\mathbf{x}) \equiv -\frac{\partial N}{\partial x} = \frac{-1}{g}\frac{\partial \phi}{\partial x} \tag{3}$$

— Vertical Deflection, North Component,

$$\xi(\mathbf{x}) \equiv -\frac{\partial N}{\partial y} = \frac{-1}{g}\frac{\partial \phi}{\partial y}. \tag{4}$$

These quantities are related to one another through Laplace's equation:

$$\frac{\partial^2 \phi}{\partial x^2} + \frac{\partial^2 \phi}{\partial y^2} + \frac{\partial^2 \phi}{\partial z^2} = 0. \tag{5}$$

Substitution of equations (2), (3), and (4) into Laplace's equation (5) yields

$$-g\left|\frac{\partial \eta}{\partial x} + \frac{\partial \xi}{\partial y}\right| - \frac{\partial \Delta g}{\partial z} = 0. \tag{6}$$

The derivative property of Fourier transforms along with the upward continuation property of the gravitational potential is used to reduce the differential equation (6) into an algebraic equation. The forward and inverse Fourier transforms are defined as

$$F(\mathbf{k}) = \int_{-\infty}^{\infty}\int_{-\infty}^{\infty} f(\mathbf{x})\,\exp\,[-i2\pi(\mathbf{k}\cdot\mathbf{x})]d^2x, \tag{7}$$

$$f(\mathbf{x}) = \int_{-\infty}^{\infty}\int_{-\infty}^{\infty} F(\mathbf{k})\,\exp\,[i2\pi(\mathbf{k}\cdot\mathbf{x})]d^2\mathbf{k}. \tag{8}$$

The Fourier transform of equation (7) is

$$-i2\pi g[k_x\eta(\mathbf{k}) + k_y\xi(\mathbf{k})] - \frac{\partial \Delta g(\mathbf{k}, z)}{\partial z} = 0, \tag{9}$$

where g is the gravitational acceleration and i is $\sqrt{-1}$. From the solution to Laplace's equation in the wavenumber domain, the upward continuation formula relates the gravity anomaly at the surface of the earth to the gravity anomaly at some elevation z.

$$\Delta g(\mathbf{k}, z) = \Delta g(\mathbf{k}, 0)\,\exp\,[-2\pi|\mathbf{k}|z], \tag{10}$$

where

$$|\mathbf{k}| = (k_x^2 + k_y^2)^{1/2}.$$

Taking the derivative of equation (10) with respect to z and evaluating the result at $z = 0$, we arrive at an algebraic formula relating the Fourier transform of the gravity anomaly to the sum of the Fourier transform of the two components of vertical deflection:

$$\Delta g(\mathbf{k}, 0) = \frac{ig}{|\mathbf{k}|}\,[k_x\,\eta(\mathbf{k}) + k_y\xi(\mathbf{k})]. \tag{11}$$

To compute gravity anomalies from a dense network of satellite altimeter profiles of geoid height, we construct a uniform grid of geoid height and calculate the east η and north ξ components of vertical deflection. However, as mentioned above, the characteristic spacing of the Geosat profiles is much greater than the resolution along individual profiles; this limits the resolution of the resulting grid to wavelengths on the order of the track spacing. To overcome this problem, we use a 1-D approximation. First we align the x-axis of the local coordinate system in the direction of the satellite ground track. Then we assume that the curvature of the geoid in the crosstrack direction is zero; this assumption eliminates the y-derivatives in equations (5) and (6) and the k_y terms in equations (9) and (11). After simplification, the Fourier transform of the along-track gravity anomaly is related to the Fourier transform of the along-track vertical deflection by

$$\Delta g(k_x) = ig\,\frac{k_x}{|k_x|}\,\eta(\mathbf{k}). \tag{12}$$

This procedure of Fourier transformation of the along-track vertical deflection, multiplication by $ig\ \mathrm{sgn}\ (k_x)$, and inverse Fourier transformation corresponds to the Hilbert transform of the vertical deflection profile scaled by the average acceleration of gravity. This formula provides the gravity anomaly on a reference surface and requires an additional correction to account for the deviation of the sea surface or geoid height from the reference surface. From equation (12) we see that 1 microradian (μrad) of vertical deflection corresponds to 0.98 mGal of horizontal gravity anomaly.

The conversion of vertical deflections to free air gravity anomalies involves low-pass filtering of the data, removing the long wavelength components of the potential, Hilbert transforming the deflections to compute gravity anomaly, and then replacing the long wavelength components of the gravity field; the various steps are shown in Figure 3. This process is applied to each profile independently and makes use of the fast Fourier transform (FFT) algorithm to implement the Hilbert transform.

During the averaging of the repeat vertical deflection profiles a low-pass filter was applied (Sandwell and McAdoo, 1990). The low-pass filter operation consisted of convolution with a Gaussian function where the 0.5 attenuation occurs at

a wavelength of 18 km. This prefiltering was performed prior to averaging so that the cutoff wavelength could not be changed.

To minimize error resulting from the flat-earth approximation and any components of the field with wavelengths longer than the individual profile, a low degree geoid model is removed from the vertical deflection profiles (Figure 3, top profile). The long wavelength field was obtained from the OSU89B1 geopotential model (Rapp and Pavlis, 1990). Although this model is complete to a spherical harmonic 360 degrees, we have investigated the effect of removing lower degree fields as well. Once the vertical deflections are appropriately band limited, the Hilbert transform is applied [equation (12)]. To minimize the edge effects associated with the Fourier transformation of a finite length profile, the ends of the vertical deflection profiles are extended and the cosine tapered to zero. After the data are transformed and rescaled, the long wavelength components of the gravity field obtained from the model are replaced. The final gravity profile is shown as the lowest profile in Figure 3 along with the shipboard gravity profile for comparison. For all of these comparisons, no shifts or linear trends have been applied to either the satellite gravity profiles or the shipboard gravity profiles.

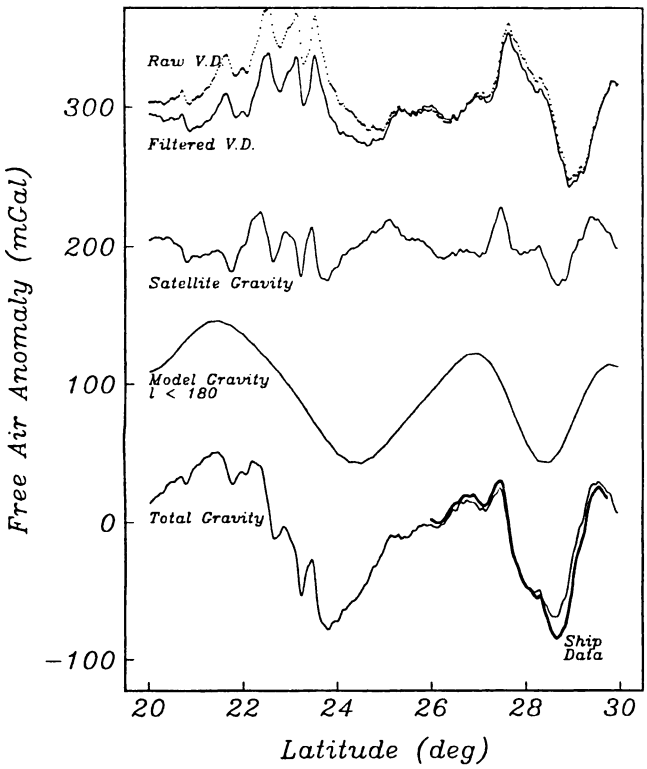

FIG. 3. Example of the processing sequence used to compute gravity profiles. Raw vertical deflections (upper dotted curve) are smoothed, and the long wavelength components of the gravity field are removed. The resulting filtered vertical deflection profile (upper solid curve) is Hilbert transformed to compute the short wavelength components of the satellite gravity profile. The long wavelength components of the gravity field are then replaced to produce the final gravity profile. Available shipboard data are shown as the darker curve for comparison.

RESULTS

The comparisons between all of the available satellite gravity profiles and shipboard gravity profiles are shown in Figure 4. In all cases the shipboard gravity profile is the solid curve and the satellite gravity is the long dashed curve. For this comparison, the OSU89B1 spherical harmonic model to 180 degrees was used as a reference field (Rapp and Pavlis, 1990). The average rms difference between the 17 satellite gravity profiles and the corresponding shipboard gravity profiles is 6.5 mGal. Also shown in Figure 4 (short dashed curve) is the 1-D satellite gravity anomaly that was constructed using no spherical harmonic reference model; in this case, the rms difference is somewhat higher (15.5 mGal). It can be seen that, in most cases, the primary effect of using the long wavelength reference model is to adjust the dc component of the profile and in some cases to correct a long wavelength trend. In general, the agreements are quite good especially at intermediate and long wavelengths ($\lambda > 25$ km). However, as expected, the short wavelength anomalies are not resolved by the satellite data.

To quantify the short wavelength resolution of the satellite data, we have estimated the spectral coherence between the satellite and shipboard gravity profiles. Spectral coherence is defined as

$$\gamma^2_{xy}(k) = \frac{|G_{xy}(k)|^2}{G_{xx}(k)G_{yy}(k)},$$

where $G_{xy}(k)$ is the cross spectrum and $G_{xx}(k)$ and $G_{yy}(k)$ are the auto spectra of data series (Bendat and Piersol, 1986). Spectral coherence estimates range from 0 to 1 for wavenumbers between 0 and the Nyquist frequency (1 km in this case) and provide a measure of the degree to which the satellite and shipboard gravity data are linearly related at a given wavenumber. Because the available shipboard profiles are relatively short and dominated by long wavelength anomalies, spectral coherence was not estimated for individual profiles. The individual profiles were tapered and concatenated to produce a single profile for the shipboard data and a single profile for the satellite data. These longer profiles are much better suited to a spectral analysis and allow for ensemble averaging, thereby reducing the variance of the spectral estimates. The spectral estimates were made using Welch's method of averaging over modified periodigrams (Welch, 1967).

The coherence estimates, with 95 percent confidence intervals are shown in Figure 5. Because the confidence intervals for coherence estimates are inversely proportional to the value of the estimate itself, the confidence intervals for the low coherences are very large and therefore not plotted. At wavelengths greater than 50 km (wavenumber <0.02 km^{-1}) the coherence between the satellite gravity and the shipboard gravity is quite high (>0.9), but it falls off sharply at shorter wavelengths; by a 25 km wavelength, the coherence is 0.5, and it is essentially zero for wavelengths less than 16 km. These resolution estimates are only slightly worse than the estimates derived from repeating Geosat/ERM profiles in deep ocean areas (Sandwell and McAdoo, 1990) suggesting that the hybrid method of computing satellite gravity anom-

alies does not significantly degrade the along-track resolution of the Geosat/ERM profiles.

Although the coherence provides a measure of the short wavelength resolution of the satellite gravity profiles, it does not provide a measure of the accuracy of the satellite data. To estimate the absolute accuracy, we calculated the rms difference between the satellite gravity profiles and the shipboard profiles. In addition, we varied the cutoff wavelength of the spherical harmonic model to establish the optimum cutoff. Six reference models were used corresponding to spherical harmonic cutoffs of 40, 90, 130, 180, 270, and 360 degrees. In each case, the spherical harmonic coefficients were tapered using a cosine function to reduce ringing in the reference gravity field. For example, the 180 degree cutoff model was tapered between harmonics of 140 and 220 degrees. As seen in Figure 6 (filled circles), the rms difference between the 17 satellite gravity profiles and the shipboard profiles decreases with increasing spherical harmonic degree of the reference model.

DISCUSSION

In the introduction, we identified three practical reasons why it is difficult to construct gravity anomalies from satellite altimeter profiles. The first was poor altimeter resolution and accuracy, the second was an edge effect due to the lack of satellite altimeter measurements over land, and the third was the unresolved anomalies due to the wide track spacing of the Geosat/ERM profiles.

We first consider whether or not the disagreement between the shipboard and satellite measurements are a result of inaccurate satellite data. As shown in Figure 2, the uncertainty of the averaged vertical deflection profile was computed during the averaging process, and it provides a

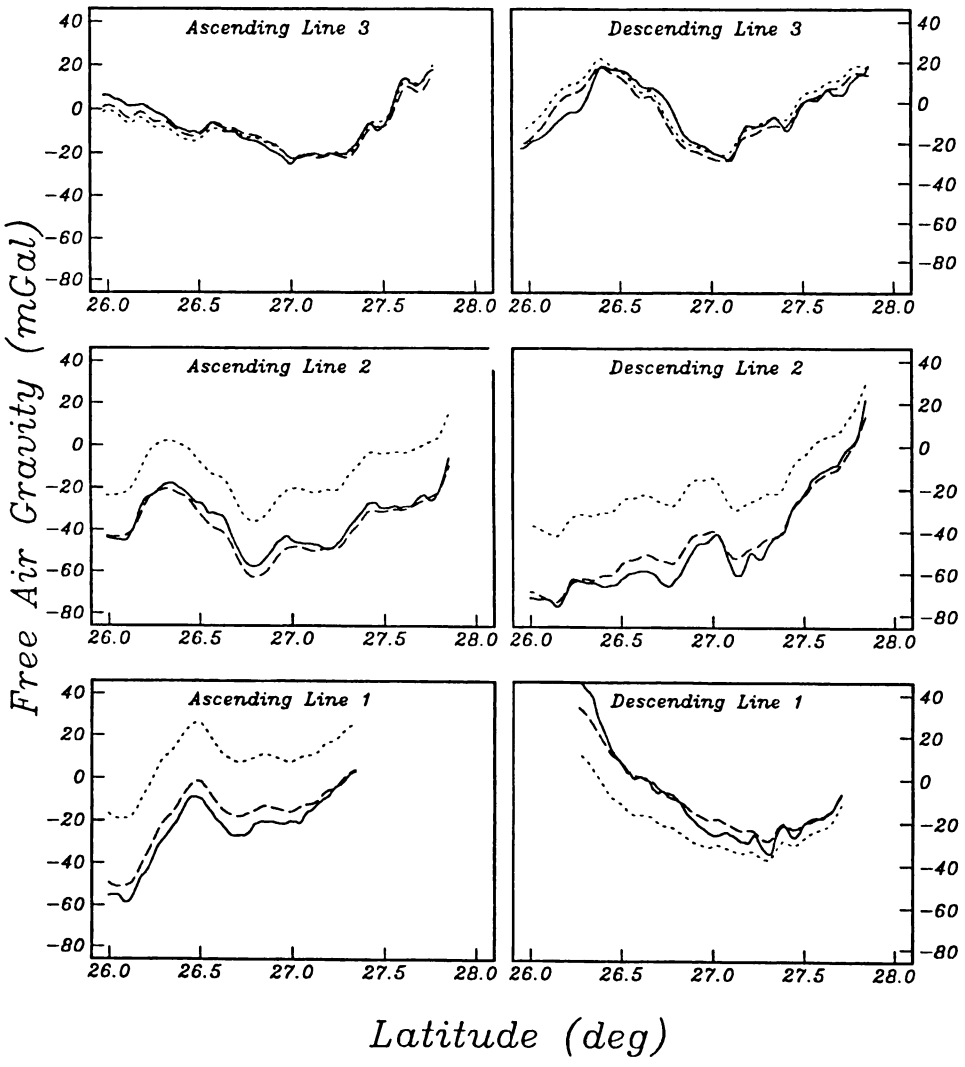

FIG. 4. Comparison of 17 shipboard and satellite gravity profiles in the northern Gulf of Mexico. Locations are shown in Figure 1. In each case, the shipboard data are plotted as the solid curve, the satellite gravity computed with a 180 degree reference field is shown as the long dashed curve, and the satellite gravity computed without a reference field is shown as the short dashed curve. The shipboard data have been decimated to 3.4 km for display purposes.

measure of the precision of the 1-D satellite gravity profiles. We have compared this estimated uncertainty with the difference between the satellite gravity and the shipboard gravity on a point-by-point basis and found no apparent correlation. We have also compared the rms misfit to the mean uncertainty for each profile and found no correlation. Since the estimated uncertainty is also four times smaller than the rms disagreement of the satellite gravity profile, we do not believe that the accuracy of the satellite measurements is the limitation.

The spectral coherence estimates in this study indicate that the satellite can resolve features with wavelengths as short as 25 km. The power spectrum of the shipboard data indicates that there is significant power at shorter wavelengths, as would be expected. Figure 7 shows an example of the difference in resolution from the northern end of descending line 3. The solid curve is the shipboard data and the dashed curve is the satellite data computed with a 180 degree reference field. The agreement with the ~20 km resolution limit for deep ocean profiles (Sandwell and McAdoo, 1990) would seem to indicate that this is a fundamental limitation of the Geosat altimeter data. Although future satellite missions will provide tighter track spacing, altimeter precision is not expected to increase dramatically (McConathy and Kilgus, 1987). Altimeter resolution is limited by the sea state, atmospheric effects, and the noise level in the return signal which require that the data be edited and smoothed before processing. This smoothing is probably the primary limitation on the along-track resolution of the satellite data.

The fundamental assumption of the 1-D Hilbert transform is that the 2-D spectrum of the geoid slope in the across-track direction is zero [i.e., $\xi(k)$ in equation (11)]. This implies that the gravity field is corrugated in the direction perpendicular to the profile and is obviously a poor assumption in the Gulf of Mexico. Profiles A8 and D7 (Figure 1) illustrate this limitation. Profile D7 is nearly perpendicular to the strong gravity trough associated with the Florida Escarpment at 28° latitude (Figure 4). In this case, the 1-D approximation is nearly valid, and the satellite gravity (both with and without the reference model) match the shipboard gravity remark-

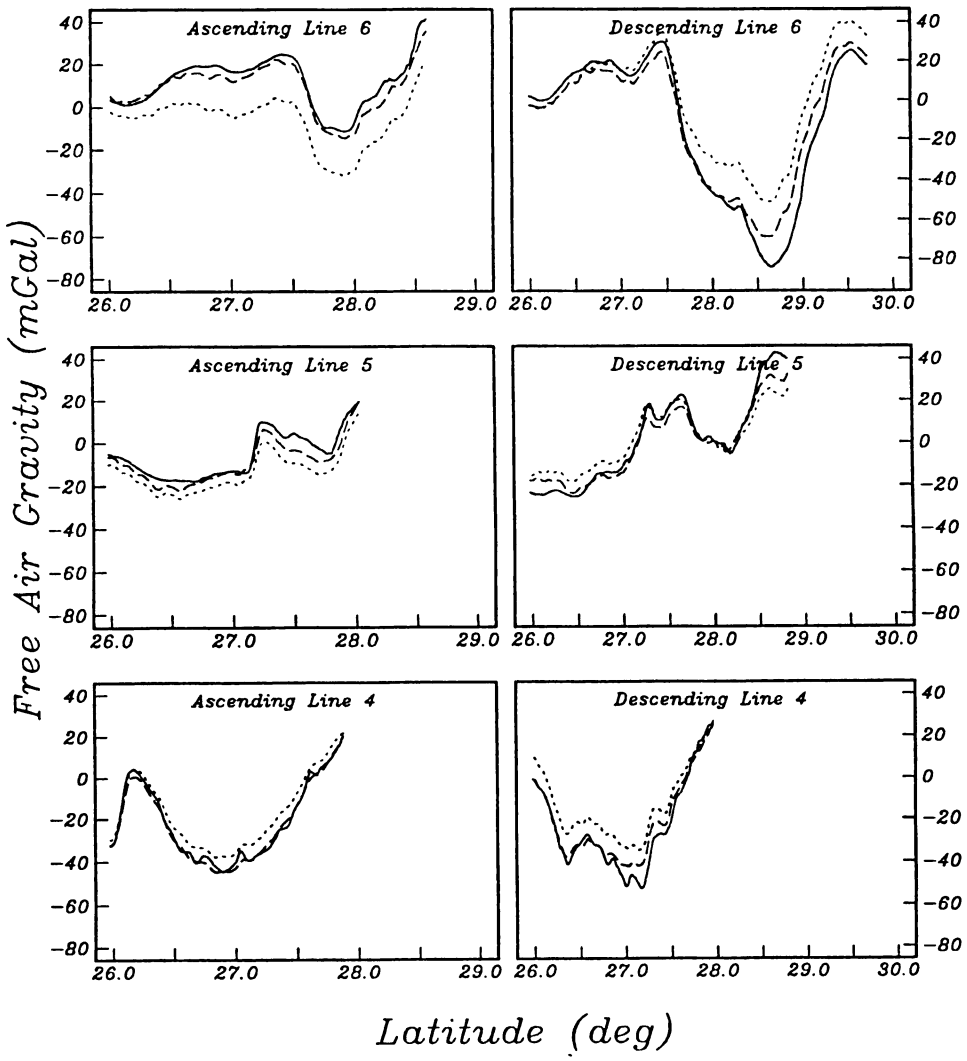

(Fig. 4. continued)

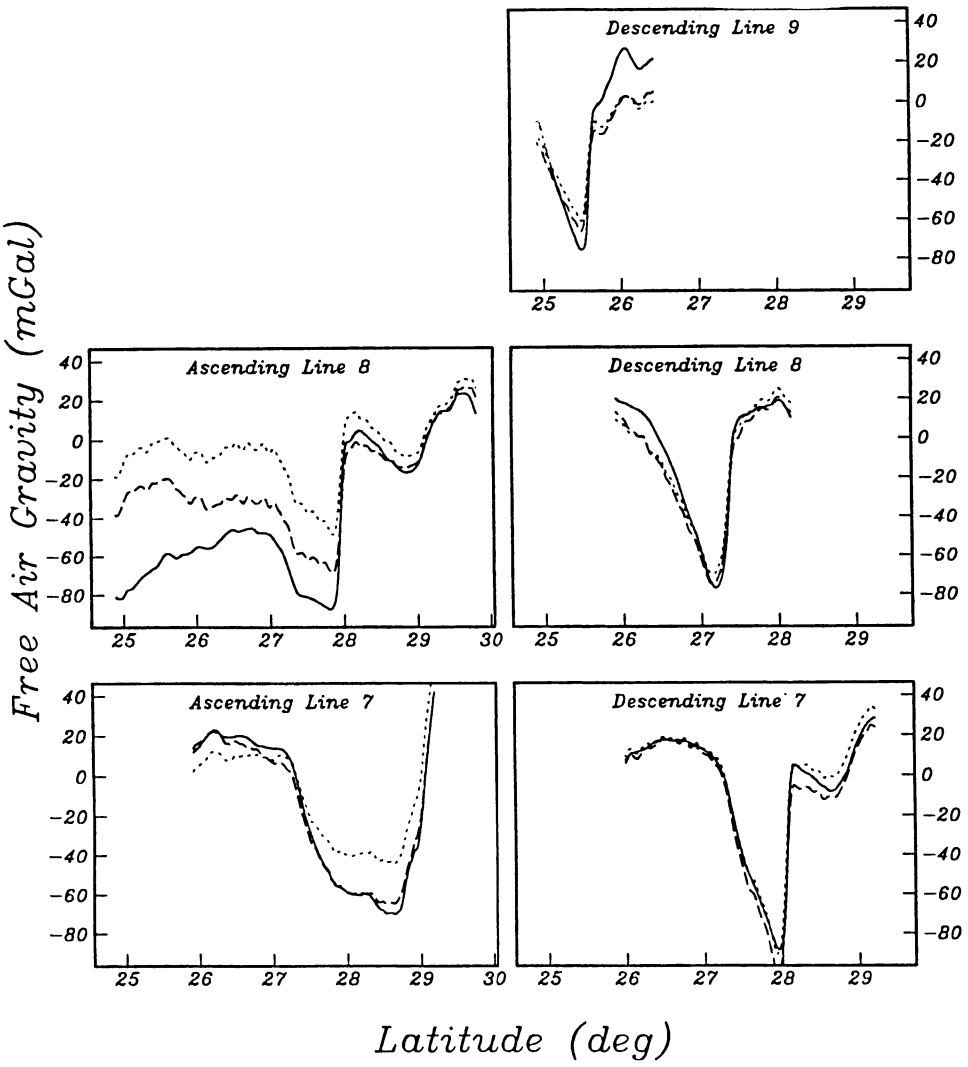

(FIG. 4. continued)

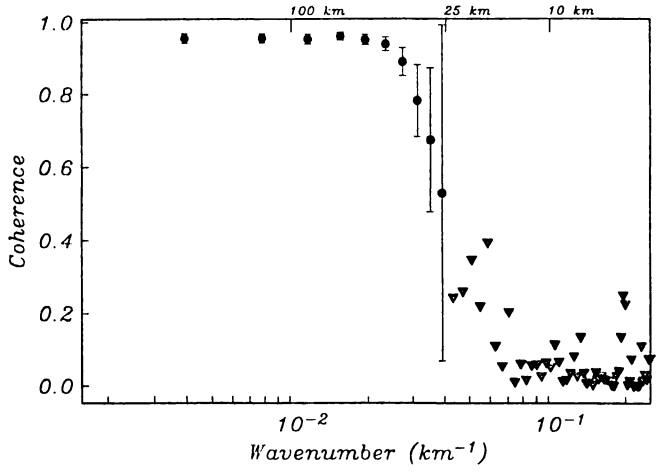

FIG. 5. Spectral coherence estimates for shipboard and satellite gravity profiles. Satellite data were interpolated to the 0.5 km sample spacing used for the shipboard data. Coherence rolls off to 0.5 at a wavenumber of 0.4 km^{-1} giving an effective resolution limit of 25 km for the satellite data. Error bars indicate 95 percent confidence intervals.

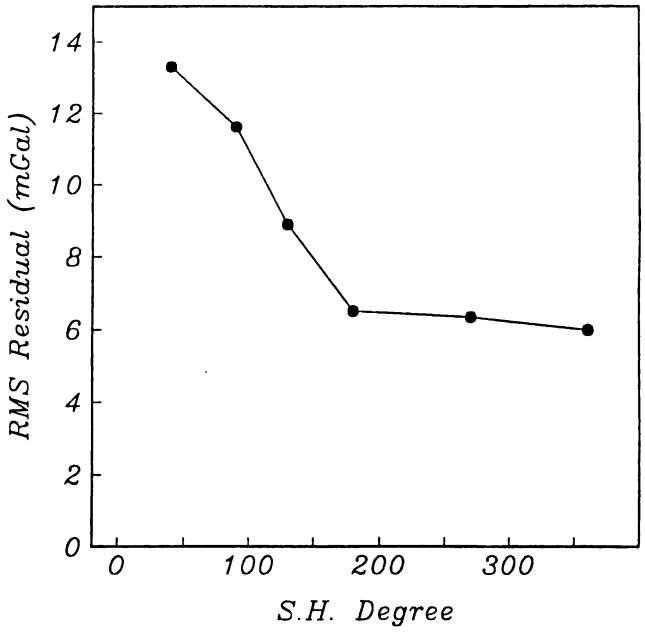

FIG. 6. RMS misfit versus spherical harmonic degree of reference field. Residual decreases linearly with the increasing degree of reference field up to 180 degrees ($\lambda > 220$ km). Improvement is negligible for 180 to 360 degrees ($\lambda > 110$ km).

ably well. In contrast, profile A8 crosses the same area of the Florida Escarpment but at an angle of ~20°. In this case, the satellite gravity profile with no reference model shows a poor fit to the shipboard profile; the amplitude of the satellite gravity step is only 2/3 the actual amplitude. The fit is improved by using the 180 degree reference, but even in this case, the satellite gravity step is too small.

Since the spherical harmonic expansion of the long wavelength gravity field is fully 2-D and correctly models the long wavelength components of the field, we assume that the 1-D assumption is the primary cause of the long wavelength disagreement seen in the uncorrected profiles. Given the rather complex nature of the gravity field in the Gulf at intermediate to long wavelengths it is not surprising that the 1-D assumption would break down at these wavelengths. Although we do not expect the short wavelength resolution to vary appreciably for other basins, the long wavelength agreement *should* be strongly dependent on large scale regional structure. For example, profiles crossing nearly perpendicular to a rather linear continental margin should be able to accurately reproduce wavelengths longer than 220 km without a reference field. Although an analogous 1-D transform that assumes an isotropic gravity field may be applied, we feel that this is even less justified than a lineated field in a continental margin environment.

CONCLUSIONS

In conclusion, shipboard gravity data in the Gulf of Mexico provide a "ground truth" measure of the accuracy and resolution of satellite gravity profiles. Moreover, they enable us to choose the optimum method for constructing these profiles. To retain the short wavelengths available in the Geosat/ERM data and still construct accurate gravity profiles, we have developed a procedure where a spherical harmonic gravity model is used to constrain the long wavelengths, while the original satellite profile provides the short wavelength gravity signal. Spectral coherence estimates indicate that the satellite-derived gravity profiles resolve wavelengths as short as 25 km in the Gulf of Mexico. By varying the spherical harmonic degree of this reference model, we found that the accuracy in the satellite gravity profiles increases linearly as a function of the spherical harmonic up to 180 degrees; for higher degrees the improvement is negligible. When a 180 degree spherical harmonic reference model is used, the satellite gravity profiles are accurate to 6.51 mGal for wavelengths >25 km. The shipboard data show significant anomalies at shorter wavelengths that are unresolved by the satellite.

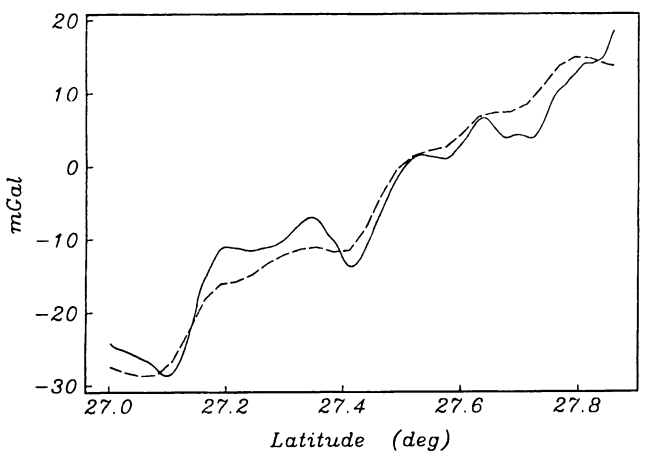

FIG. 7. The northern end of descending profile line 3 shown on an enlarged scale. The shipboard data indicated by the solid curve, and the satellite data, computed with 180 degree reference field, is shown as the dashed curve. Although the satellite resolves features with wavelengths as short as ~25 km, the amplitude is substantially reduced.

ACKNOWLEDGMENTS

We are grateful to Alan Herring *and Edcon Inc.* for providing the shipboard data used in this study. This study was initiated while C. Small was employed by the Exxon Production Research Company and was supervised by R. K. Warren and R. S. Lu. M. Alexander, M. T. Angelich, and M. Jones at Exxon USA also provided valuable assistance in the initial stages of this study. R. Rapp graciously provided us with the OSU89B1 geopotential model.

REFERENCES

Bostrom, R. C., 1989, Subsurface exploration via satellite-Structure visible in Seasat images of North Sea, Atlantic Continental Margin, and Australia: AAPG Bull., **73**, 1053–1064.
Bendat, J. S., and Piersol A. G., 1986, Random data analysis and measurement procedures, Second Ed.: John Wiley & Sons, Inc.
Haxby, W. F., 1987, Gravity field of the world's oceans: Nat. Geophys. Data Center, NOAA, Boulder, CO.
Haxby, W. F., Karner, G. D., LaBrecque, J. L., and Weissel, J. K., 1983, Digital images of combined oceanic and continental data sets and their use in tectonic studies: EOS Trans. Am. Geophys. Union, **64**, 995–1004.
Heiskanen, W. A., and Moritz, H., 1967: Physical geodesy, San Francisco, Calif.: W. H. Freeman & Co.
McAdoo, D. C., Agreen, R. W., Cheney, R. E., Douglas, B. C., Doyle, N. S., Miller, L., and Timmerman, E. L., 1990, Geosat/Geodetic mission geophysical data records: Format and contents: NOAA Tech. Memo..
McConathy, D. R., and Kilgus, C. C., 1987, The Navy Geosat Mission: An Overview: Johns Hopkins APL Technical Digest, **8**, no. 2, 170–175.
Rapp, R. H., and Pavlis, N. K., 1990, The development and analysis of geopotential coefficient models to spherical degree 360.: J. Geophys. Res., **95**, 21 885–21 991.
Roest, W. R., 1987, Seafloor spreading pattern of the North Atlantic between 10° and 40° N: Geologica Ultraiectina, **48**, 1–121.
Sandwell, D. T., 1991, Geophysical applications of satellite altimetry: Reviews of Geophysics, 132–137.
Sandwell, D. T., and D. C. McAdoo, 1990, High-accuracy, high-resolution gravity profiles from two years of the Geosat exact repeat mission: J. Geophys. Res., **95**, 3049–3060.
Welch, P. D., 1967, The use of the fast Fourier transform for estimation of power spectra: A method based on time averaging over short modified periodograms: IEEE Trans. Audio Electroacoust., **AU15**, 70–73.

This chapter, in full is a reprint of the material as it appears in *Geophysics*, V.7, 1992. The dissertation author is the primary investigator and author of this paper.

Chapter 6

Application of Large Scale Terrain Corrections to Satellite Gravity Data in the Gulf of Mexico

Christopher Small and Robert L. Parker

Institute for Geophysics and Planetary Physics
Scripps Institution of Oceanography
University of California San Diego
La Jolla, CA 92093

Introduction

The Gulf of Mexico is one of the most heavily probed pieces of real estate on the planet. Nonetheless, it is one of the most poorly understood in light of the attention it has received. The reason for this is twofold; it was not formed by a simple rift geometry and it's deeper structure is obscured by very thick sediments. These complications are compounded by an extremely uneven distribution of data. Most of the information presently available on the gulf is the result of extensive petroleum exploration and is largely limited to the northern regions. Even the bathymetry of the southern Gulf of Mexico is not well mapped. In addition, the vast amount of information that is available is primarily limited to detailed measurements of shallow sedimentary sections on the continental shelves. In order to better understand the large scale structure and evolution of the gulf it is necessary to consider the basin as a whole.

A single, self consistent geophysical study of the entire gulf has yet to be done with terrain corrected gravity data. Satellite gravity data provide an opportunity to conduct such a study. Satellite data provide uniform coverage of both the heavily explored northern gulf and the less explored southern gulf which is not available with other types of data. A terrain corrected gravity map for the Gulf of Mexico may help to constrain the distribution of oceanic crust, the thickness and distribution of attenuated continental crust, the presence of transform offsets in the initial rift structure and the spatial extent of the initial rift.

Constraints on the Crustal Structure of the Gulf of Mexico

At present, the large scale crustal structure of the Gulf of Mexico has been determined from relatively localized geophysical surveys. While there is an abundance of data available in the northern gulf , the central and southern regions have not been thoroughly explored. Constraints on large scale crustal strucure are derived from seismic refraction, gravity and magnetic studies. The limit of unstretched continental crust in the northern gulf is based primarily on gravity and magnetic data (Klitgord et al, 1988; Klitgord & Schouten, 1986). Gravity data have also been used in the northern gulf to constrain the amount of stretched crust (Kruger & Keller, 1986). Crustal thicknesses and velocities are constrained in the northern and southeastern gulf by isolated seismic refraction surveys (Nakamura et al, 1988; Ebeniro et al 1988; Ibrahim et al, 1981; Ibrahim & Uchipi, 1982; Ebeniro & O'Brien, 1984). Refraction surveys have also indicated the presence of oceanic crust in the central gulf (Ewing et al, 1962; Buffler et al, 1980,1981; Ibrahim et al 1981; Buffler & Sawyer, 1985; Rosenthal, 1987; Ebeniro et al, 1988). Although extensive

seismic reflection work has been done, the thick sedimentary section and widespread, highly reflective evaporites have prevented imaging of the lower crust and moho on reflection lines.

A study of the entire Gulf of Mexico was done by Hall et al (1982) using regional gravity data. The gravity data used in their study were obtained from a published map of simple Bouguer gravity values (Krivoy et al, 1976) and supplemented with industry data in the northern gulf. The gravity grid used in their study had adequate coverage in the northern gulf but was poorly constrained in the central and southern gulf where satellite coverage is now available. The gravity data now available will allow for a considerable improvement over those used to construct the map described above. Furthermore, the simple Bouguer correction used in their study would not be accurate near the shelf edges where the largest anomalies occur; in these areas a detailed terrain correction is necessary. The report accompanying their map concludes with the statement "...it would be important to update, correct, review, and revise this map whenever additional data become available." (Krivoy et al, 1976).

A Bouguer gravity map of the continental United States (SEG, 1982) was used recently by Jachens et al (1989) to construct an isostatic residual gravity map. The Bouguer map incorporates free air gravity data in offshore areas and provides constraints in the northern gulf but it does not extend into the southern regions. Jachens et al (1989) state that the isostatic residual map contains artifacts in the offshore areas resulting from the application of a simple Bouguer correction in areas of rapidly changing depth. This is precisely the effect which this study is designed to eliminate.

The Method

The calculation, described in detail by Parker (1993), proceeds as follows. At each point in the grid the total gravitational attraction of the seafloor topography is divided into a near field component and a far field component. For the near field component, the attraction of all the mass within a disc of a given radius is calculated by direct integration. For the far field component, the attraction of all the mass outside the disc is calculated using the transform method described by Parker (1993). The near and far field components are then combined at each point to give the total gravitational attraction.

The calculation of the near field component is accomplished by direct numerical quadrature of the integral for gravitational attraction of a single mass layer. By limiting the radius of the disc over which this integration is performed the attraction is limited to the near field mass distribution. In theory this method could be used by itself if the domain of the integral (radius of the disc) were extended to the limits of the grid at each point. This would be extremely inefficient as the integral

must be re-evalulated at every point in the grid. The major advantage of this method is that the domain of the near field calculation may be limited so as to minimize computational expense.

The calculation of the far field component is accomplished using a Fourier transform method similar to that described by Parker (1973). The kernel for the gravitational attraction, $\Delta g_{>}$, of mass outside a disc of a given radius, a, may be written as a sum of filtered Fourier transforms of the topography.

$$\widehat{\Delta g_{>}} = G\rho \sum_{n=1}^{\infty} c_n F[\Delta^{2n} - z_0^{2n}] \; F[L_n]$$

Where $\Delta = h - z_0$,

h is the depth (or elevation),
z_0 is the base level,
ρ is density,
F[ ] indicates a Fourier transform,

$$c_n = \frac{\Gamma(1/2)}{\Gamma(n+1)\Gamma(1/2 - n)}$$

and

$$F[L_n] = 2\pi \int_a^{\infty} J_0(2\pi k s) s^{-2n} ds$$

$J_0()$ is a Bessel function, $\Gamma[\ ]$ is a Gamma function, k is the wavenumber, and a is the radius of the disc.

The sum over n may be made to converge very rapidly thereby allowing the far field component to be obtained with only a few terms and a negligible residual error. The advantage of the transform approach is that it allows the far field component at every point in the grid to be calculated simultaneously.

The primary advantage of the new method over the Fourier transform method proposed by Parker (1973) lies in the rate of convergence of the terms in the far field component. The original Fourier method converges slowly when the amplitude of the topography is comparable to the observers distance from the topography. This becomes a problem in areas with very rough topography and on continental margins with steep slopes. A related complication arises from the requirement of the original Fourier method that the sample spacing of the grid points be less than the observers distance from the topography. This creates problems in areas of shallow water because it requires extremely dense data coverage. The new method avoids these complications because the calculation of the near field component is not limited by the sample spacing or the

amplitude of the topography and the radius of the disc may always be chosen so as to assure rapid convergence of the far field terms. The new method is also able to include the contribution from subareal topography which could not be done with the old method. The primary limitation of the new method is the accuracy of the topographic model (Parker, 1993); this however is a limitation in any terrain correction method.

Data

Figure 1 shows the distribution of available underway bathymetry measurements in the Gulf of Mexico. In areas where measurements are sparse, these data can be supplemented with gridded data from the ETOPO5 bathymetry model (Van Wyckhouse, 1973). Existing bathymetry data are adequate even in the southern gulf to apply the required terrain correction at intermediate and long wavelengths. Although the non uniform coverage in the southern gulf results in a smoothed bathymetry model in this area, this does not present a serious problem since we are also working with a smoothed gravity field. When the underway data are gridded they agree well with the data from the ETOPO5 grid although ETOPO5 seems to be constrained in areas of the southern gulf where no underway data are available to us. For this reason we use ETOPO5 for this study. ETOPO5 lacks resolution at the short wavelengths but the resolution of the gravity data used in this regional study does not warrant a high resolution bathymetry model. For local studies it would be desirable to have higher resolution in both gravity and bathymetry data but for the purpose of looking at the larger structure the presently available grids should suffice.

The free air gravity data used here are taken from the 0.05° grid produced by Sandwell and Smith (1992). This gridded dataset is based on Geosat, Seasat and ERS-1 satellite missions and although it is of only medium resolution it does provide uniform coverage in many areas where no other data are available. As with the bathymetry data, a high resolution gravity dataset is not required for a regional study. In Figure 3 the gridded satellite data are plotted with some of the coincident shipboard gravity profiles discussed in the previous chapter. It can be seen that the major components of the field are accurately resolved although, as shown in figure 4, the amplitudes of the short wavelength anomalies are sometimes too low.

Because the terrain correction algorithm requires equally spaced data, the bathymetry and free air gravity grids were transformed and interpolated at a 5 km grid spacing. The area was extended to cover the region 15°-35°N, 260°-280°E. The limits were extended beyond the gulf in order to properly account for subareal topography in the surrounding areas, particularly the Trans-Mexican Neovolcanic Belt on the western edge near 19°N. Once equally spaced grids were produced the terrain correction was applied.

Results

The terrain corrected grid is shown in Figure 5. A disc radius of 15 km was used although the final result did not differ appreciably for other radii. The far field calculation converged quite rapidly at greater than an order of magnitude per term. A singe density contrast of 1000 km/m^3 was used for the entire grid. A series of different density contrasts ranging from 200 to 3000 km/m^3 was also tried. The actual density contrast made little difference in the appearance of the map but larger density contrasts emphasized the large scale basin structure at the expense of the smaller scale features. Since sediment density increases exponentially with depth as a result of compaction and dewatering, the density contrast at the seafloor would be expected to be significantly smaller than that between water (1000 km/m^3) and mean crustal density (~2670 km/m^3). Based on the density-depth functions of both terrigenous and carbonate sediments a contrast of 1000 km/m^{3}is reasonable.

In order to compare the new and old approaches, the terrain correction for the gulf was also computed using the FFT method (Parker, 1973). The difference is shown in Figure 6 . As expected, the largest differences are on the steep edges of the continental margins and on land. Surprisingly, the differences are rather small (< 10 mGal). This is probably the result of the rather smooth representation of the topography used in this study. A more detailed topographic model would probably produce larger differences, particularly on the continental shelves where the mean water depth (~100 m) is much less than the grid spacing (5000 m). It appears that the FFT method could have been used for this study but the results would not have been strictly correct.

It is immediately apparent that the terrain corrected gravity map resembles the mirrored topograpy. This is expected for an area this size as the large scale features are certainly compensated isostatically. The gravity lows over the continents are caused by the mass deficiency of a thicker, low density crustal "root". The large gravity high in the central gulf is the expression of an analogous "anti-root" beneath the thinner oceanic and attenuated continental crust in this area. While some similarity to the topographic model is expected, the differences are the features of interest. The most notable feature is the shape of the arcuate gravity high in the center of the gulf. This will be discussed in greater detail below.

In order to emphasize gravity anomalies resulting from differences in crustal structure and density we must remove the long wavelength, isostasy related features which dominate the corrected gravity map. Although there exist a number of filtering methods for doing this, the most desirable method is to apply an isostatic correction for the compensating mass at depth. We apply a simple Airy-Heiskanen model for local compensation (Heiskanen and Moritz, 1967). In this model, the gravitational attraction of a compensating density contrast at depth is calculated and

subtracted from the terrain corrected gravity. The topology of the density contrast interface is determined by the surface topography since the lower boundary is designed to represent the compensating mass distribution. The surface is related to the topography by $z = h_m + h\,(\rho_t / \Delta\rho)$ where h is the surface topography, h_m is the mean moho depth at the continental margin, ρ_t is the mean crustal density (or the rock/water density contrast for submarine areas), and $\Delta\rho$ is the density contrast across the lower interface. These parameters were chosen so that the resulting surface would agree roughly with published moho depths in the region (Dunbar and Sawyer, 1987); the parameters used were $h_m = 30$ km, $\rho_t = 2670$ km/m^3 (or 1670 for $h < 0$) and $\Delta\rho = 350$ km/m^3 . Once the surface has been generated its gravitational attraction is calculated and subtracted from the terrain corrected map. The density contrast used when calculating the attraction is chosen so as to remove the large scale features in the terrain corrected map thereby reducing the total range of gravity values obtained and accentuating the lower amplitude features (Figure 8). A density contrast of 170 km/m^3 was found to minimize the total range of gravity values on the residual map. This value has no particular physical significance but is chosen only to make the resulting map easier to interpret. The isostatic residual map is shown in Figure 7 . This map bears a rough resemblance to the free air anomaly map in Figure 3. This is to be expected because the large scale features are compensated isostatically.

Discussion

One interesting feature shown in the terrain corrected map (Figure 5) is the arcuate gravity high in the central gulf. This high presumably shows the areas where the crust is thinnest, or the density highest, probably representing oceanic crust. The broader, almost isolated high in the northeast gulf is oriented almost perpendicular to the arcuate high to the west and would certainly complicate any rigid plate model for the opening of the gulf if it represents oceanic crust. The gravity low corresponding to the toe of the Sigsbee Escarpment (26°N, 268°E) is also moved slightly north on the terrain corrected map indicating that the outermost part of the toe is not isostatically compensated. The expression of the Mississippi and DeSoto Canyons is also almost completely absent on the terrain corrected map indicating that these features are also not locally compensated.

The primary effect of the isostatic correction (Figure 8) is to sharpen many of the features seen on the free air gravity map (Figure 3). Particularly noticeable are the adjacent high and low immediately north of the Sigsbee Escarpment (26°N, 268°E). These correspond to a structural offset between the Perdido and Mississippi Fan Foldbelts and may represent a difference in the extent of stretching during the initial rifting episode. This is discussed in more detail below. The

arcuate gravity high in the western gulf is also sharpened somewhat as it extends fully into the Bay of Campeche.

Some of the more prominent features on the isostatic residual map are artifacts resulting from the method used to generate the map. Because the gravitational signature of the compensating density contrast at depth is smoothed by upward continuation, the combination of short wavelength features in the terrain corrected map with spatially coincident long wavelength features in the isostatic correction results in large amplitude, short wavelength anomalies in the residual map. These are most evident near the Florida and Campeche Escarpments. Also, the free air gravity values used over land are much smoother than those over water because they are derived from low degree spherical harmonic models rather than altimetry data. This again results in the subtraction of a smooth field from a rougher field, thereby accentuating the short wavelength components as is seen for the continental drainages along the northern edge of the grid.

The usefulness of these maps may be seen by comparing them with existing models for the crustal structure of the gulf which are not based on gravity data (Figure 9). The most recent synthesis of the crustal structure of the gulf is given by Sawyer et al (1991). They delimit the bounds of oceanic and stretched continental crust based on seismic data and geologic evidence such as the downslope extent of salt in the northern gulf. The crustal boundaries proposed by Sawyer et al (Figure 8) may be superimposed on the terrain corrected and isostatic residual maps in Figures 5 and 8. The most notable difference between the terrain corrected gravity map and the crustal bounds is in the southwestern gulf. The crustal bounds of Sawyer et al (1991) extend oceanic crust far into the western edge of the gulf significantly beneath the East Mexico Slope. This does not agree with the extremely narrow gravity high seen in the terrain corrected gravity map. The dataset upon which Sawyer et al (1991) base their crustal boundaries privides no coverage in this area, indicating that the extent of oceanic crust in the southwestern gulf may be considerably less than they predict. This would be expected to have a significant effect on plate reconstructions for this area.

Another interesting feature is seen in the isostatic residual map. The proposed offset between the Perdido and Mississippi Fan Foldbelts near the Sigsbee Escarpment coincides exactly with the pair of gravity anomalies discussed above. Since the gravity high adjacent to the offset does not extend south into the region assumed by Sawyer et al (1991) to be oceanic crust it may be a localized rift arm similar to the aulocogens commonly seen on rifted continental margins. A detailed discussion of the geologic correlations is beyond the scope of this paper and is best addressed in an independent study but it is encouraging that the maps shown here have some correspondence (and lack thereof...) to existing studies based on geologic data.

Conclusions

We have applied a new method of terrain correction (Parker, 1993) to gridded satellite gravity data in the Gulf of Mexico. While the difference between the new and old methods was relatively small, higher resolution datasets may show more significant differences. Regardless, the correction applied is exact (neglecting extreme far field effects) and now the greatest limitation is with the available data rather than the method. The resulting terrain corrected gravity anomaly map shows a narrow gravity high, possibly corresponding to oceanic crust in the western gulf and is considerably narrower than the previously assumed limit of oceanic crust. Because of the size of the area considered, the corrected gravity anomaly map is dominated by the effects of isostatic compensation. To remove the long wavelength anomalies which result from compensating masses at depth we use the Airy-Heiskanen local model to estimate the gravity effect of the variations in crustal thickness and remove them from the terrain corrected field. The resulting isostatic residual map is similar to the original free air anomaly map but shows some of the smaller anomalies in greater detail. Some artifacts are also introduced by the model but these are mostly limited to areas with abrupt changes in water depth and regions over land. An isolated pair of anomalies near the Sigsbee Escarpment may indicate the presence of a failed rift arm beneath a thick terrigenous sediment pile. These maps provide new constraints on crustal structure in areas which are otherwise unconstrained by geologic data.

Figure 6.1 Distribution of available underway bathymetry data in the Gulf of Mexico. Data shown are those currently available in digital format. Note difference in coverage between northern and southern gulf.

Shipboard Bathymetry Data

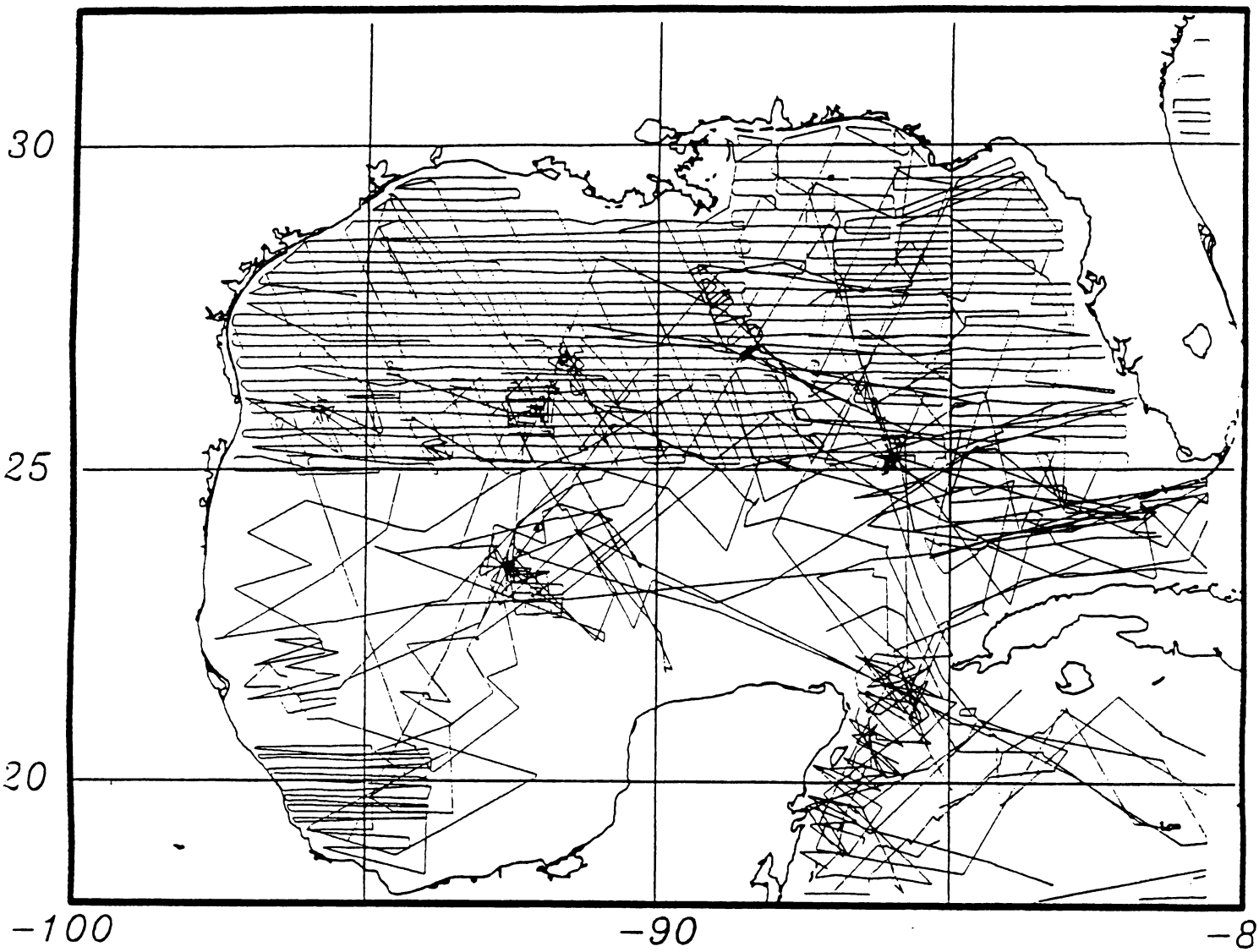

Figure 6.2 Gridded bathymetry used in this study. Because of the uneven coverage of underway data and good agreement with available underway data, ETOPO5 bathymetry measurements are used here. Data are transformed and regridded on a uniform 5 km grid.

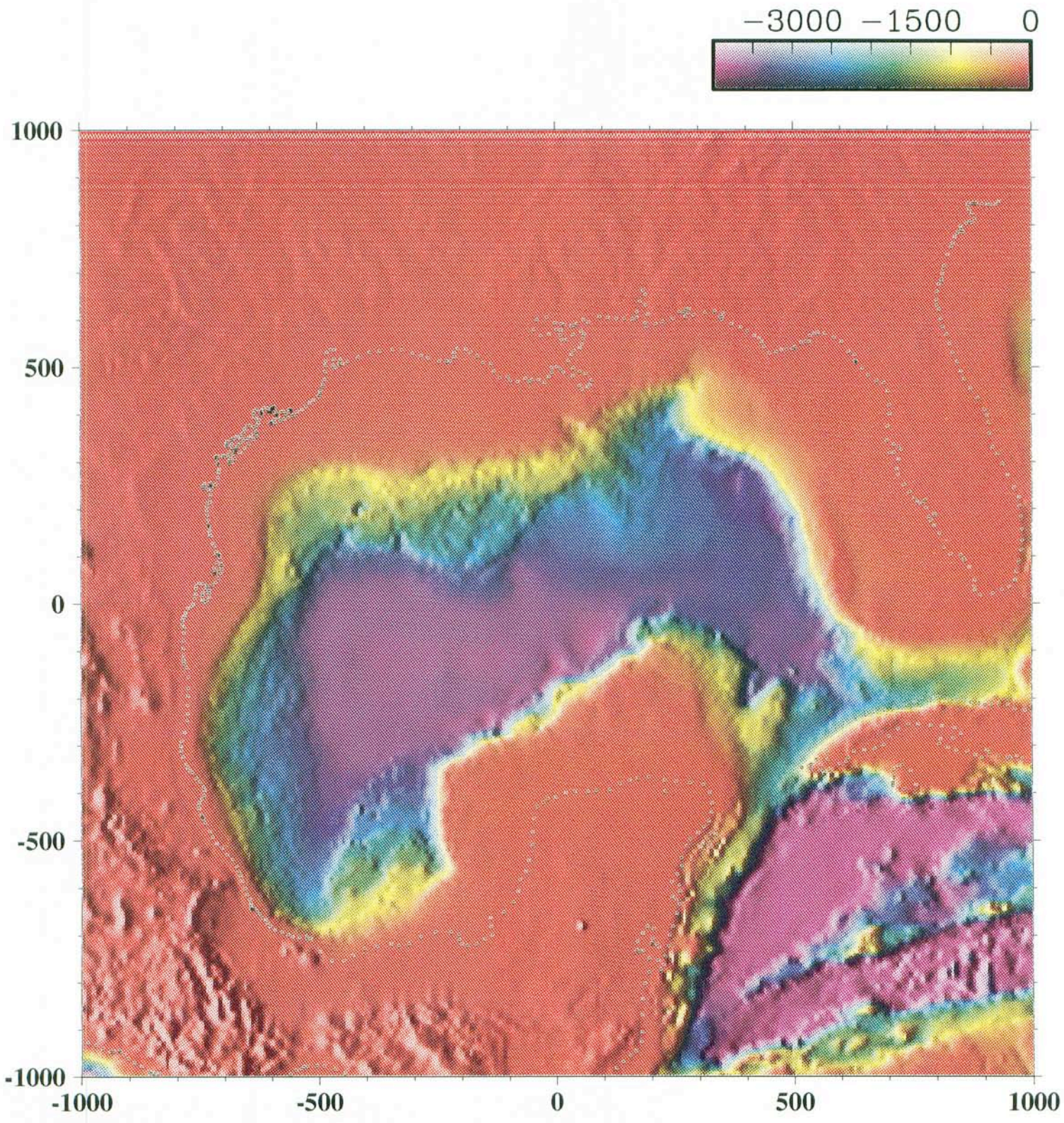
−3000 −1500 0
1000
500
0
-500
-1000
-1000
-500
0
500
1000

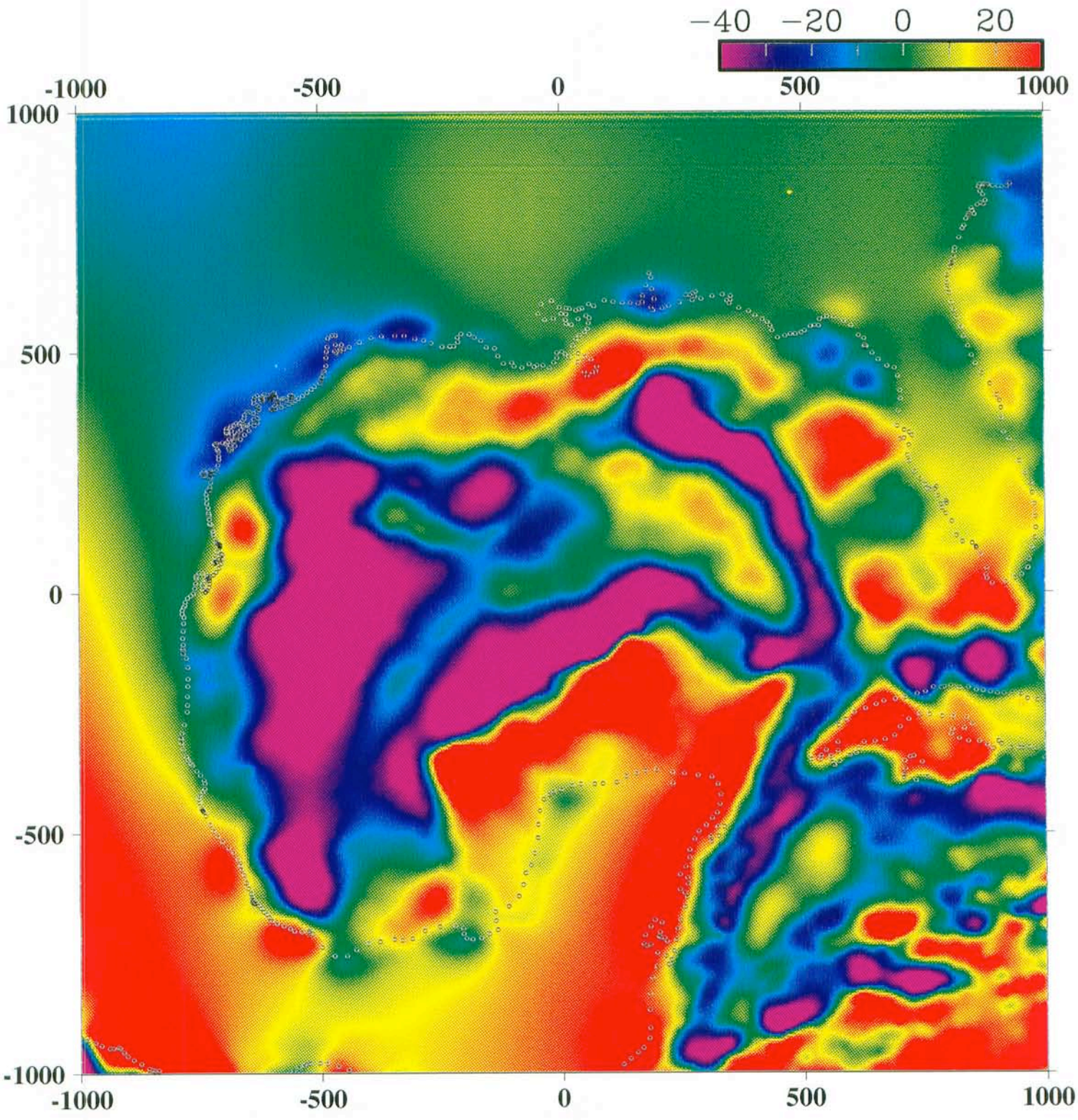
−40 −20 0 20
500
1000
-1000
-500
0
1000
500
0
-500
-1000
-1000
-500
0
500
1000

Figure 6.4 Comparison of gridded satellite and shipboard gravity in the northern Gulf of Mexico. The solid curves are the shipboard data and the dashed curves are interpolated from the satellite grid. Tracklines correspond to those shown in the previous chapter. Although the satellite data do not resolve the short wavelength features, the larger features are accurately represented.

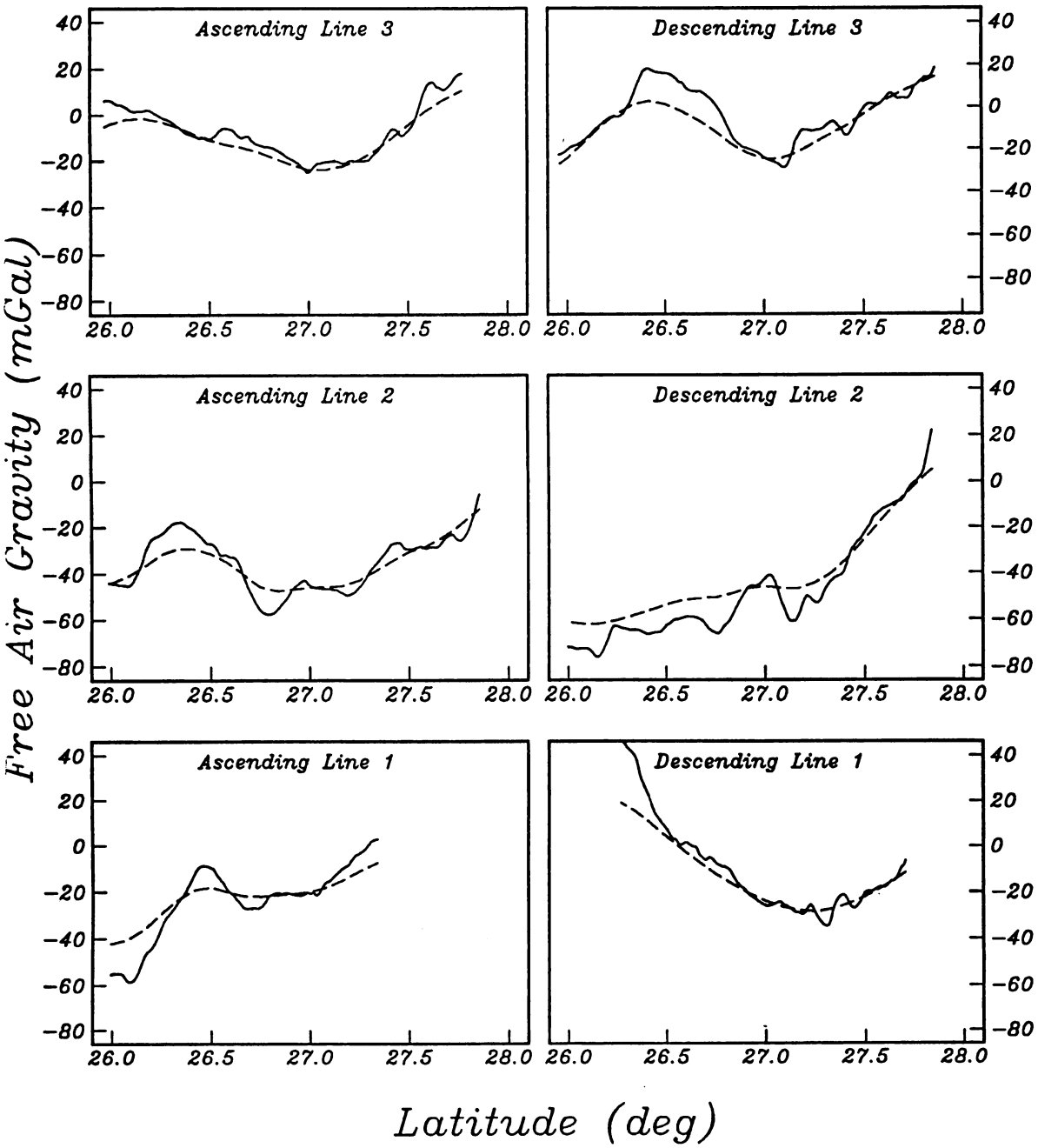
Ascending Line 3
Descending Line 3
Ascending Line 2
Descending Line 2
Ascending Line 1
Descending Line 1
40
20
0
-20
-40
-60
-80
26.0
26.5
27.0
27.5
28.0
Free Air Gravity (mGal)
Latitude (deg)

Figure 6.5 Terrain corrected satellite gravity data. Correction is applied using a density contrast of 1000 kg/m at the seafloor. As expected, the long wavelength field mirrors the bathymetry indicating that the largest features are isostatically compensated. Note the narrow arcuate gravity high extending into the southwestern gulf. This high probably indicates the presence of oceanic crust.

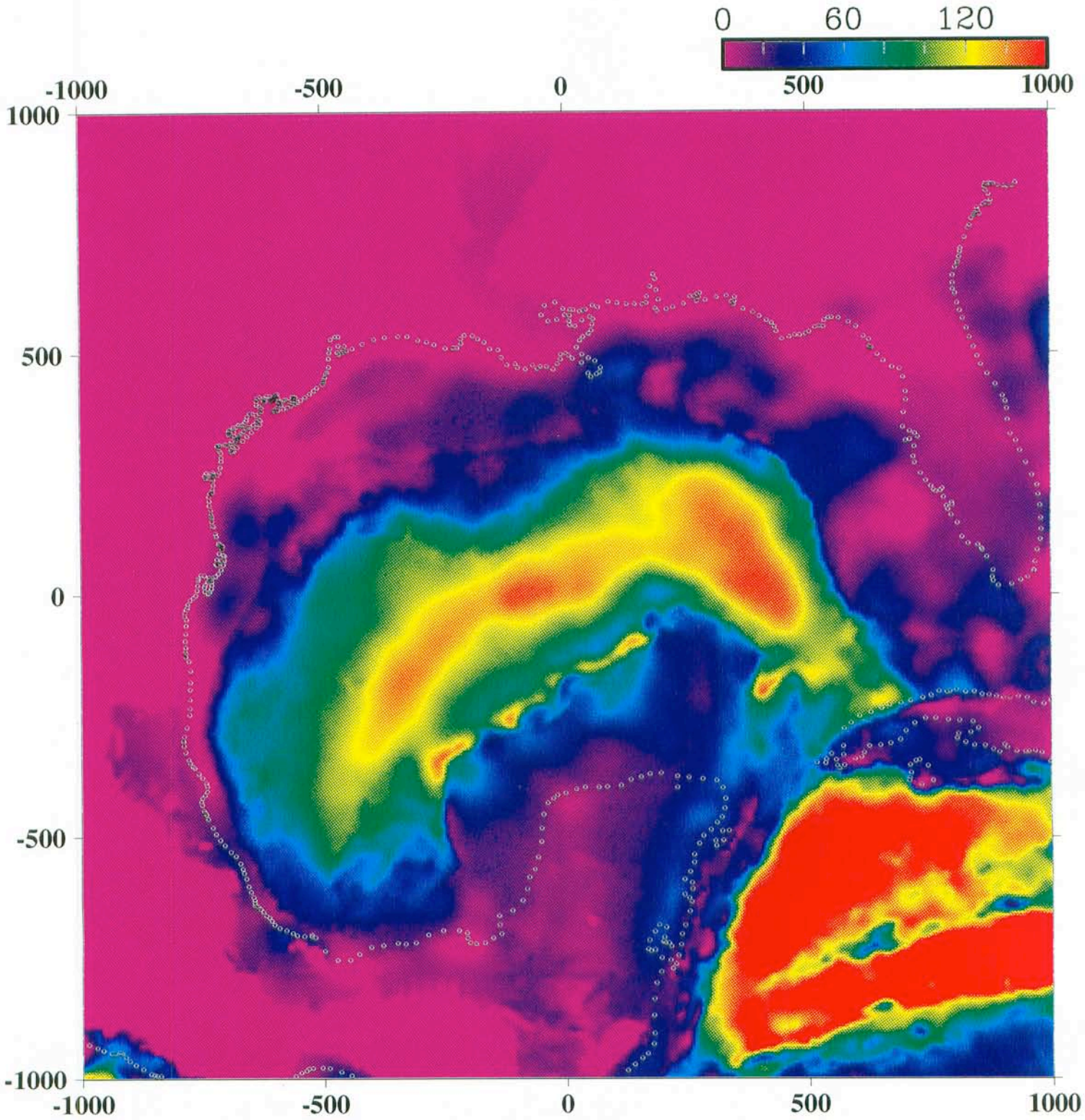
0
60
120
500
1000
-1000
-500
0
1000
500
0
-500
-1000
-1000
-500
0
500
1000

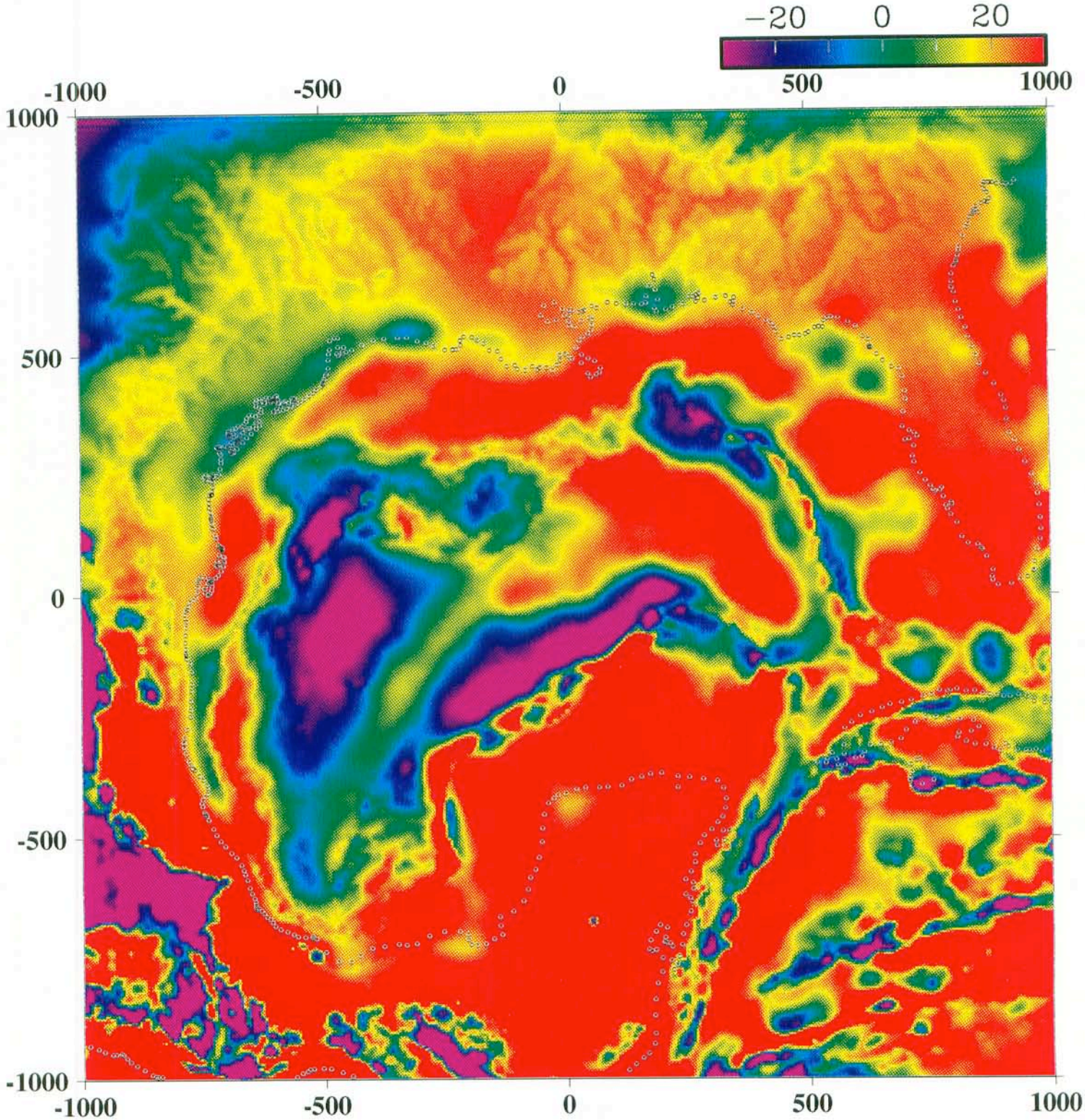
−20
0
20
500
1000
-1000
-500
0
1000
500
0
-500
-1000
-1000
-500
0
500
1000

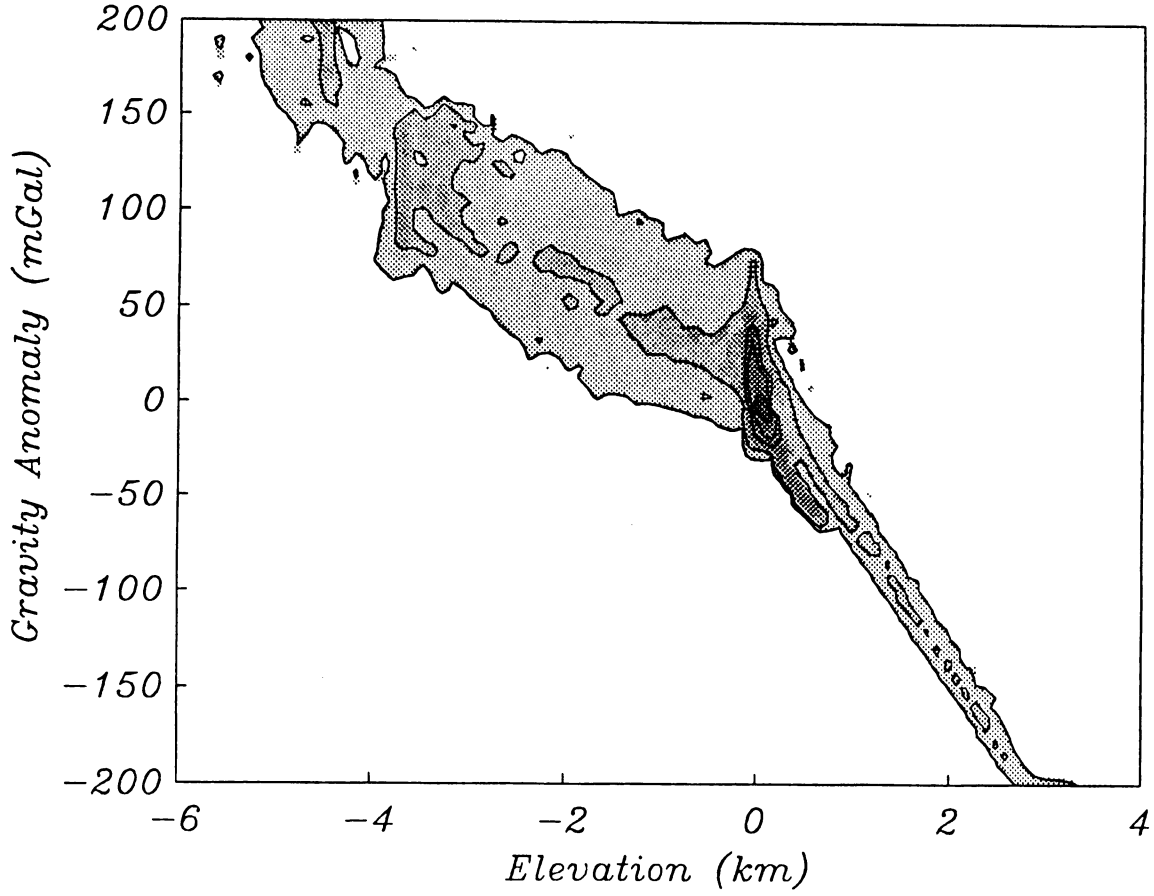
200
150
100
50
0
−50
−100
−150
−200
Gravity Anomaly (mGal)
−6
−4
−2
0
2
4
Elevation (km)

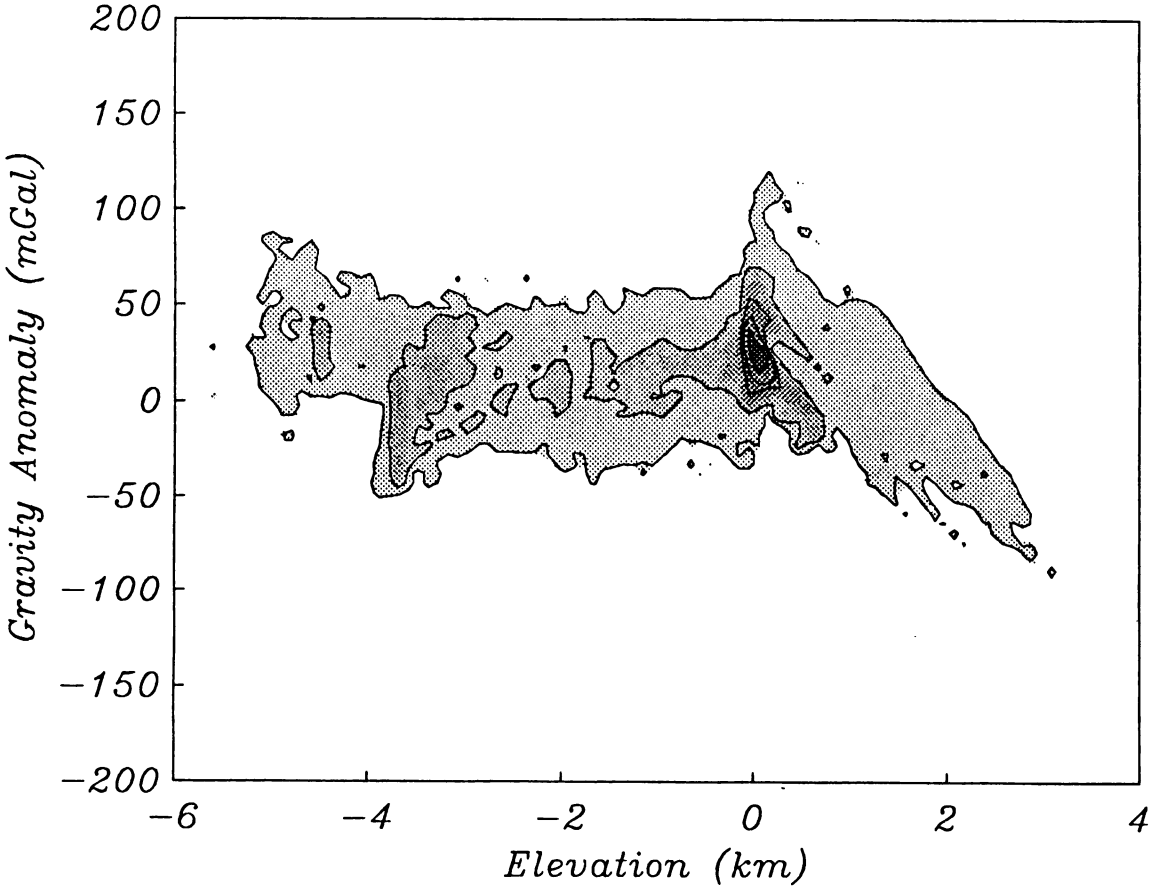
200
150
100
50
0
−50
−100
−150
−200
Gravity Anomaly (mGal)
−6
−4
−2
0
2
4
Elevation (km)

Figure 6.8 Isostatic residual anomaly map. This map is produced by subtracting the gravitational effect of a compensating mass distribution at depth from the terrain corrected gravity data. Note the similarity to the free air anomaly map. Many short wavelength anomalies are sharpened although some artifacts are introduced (see text).

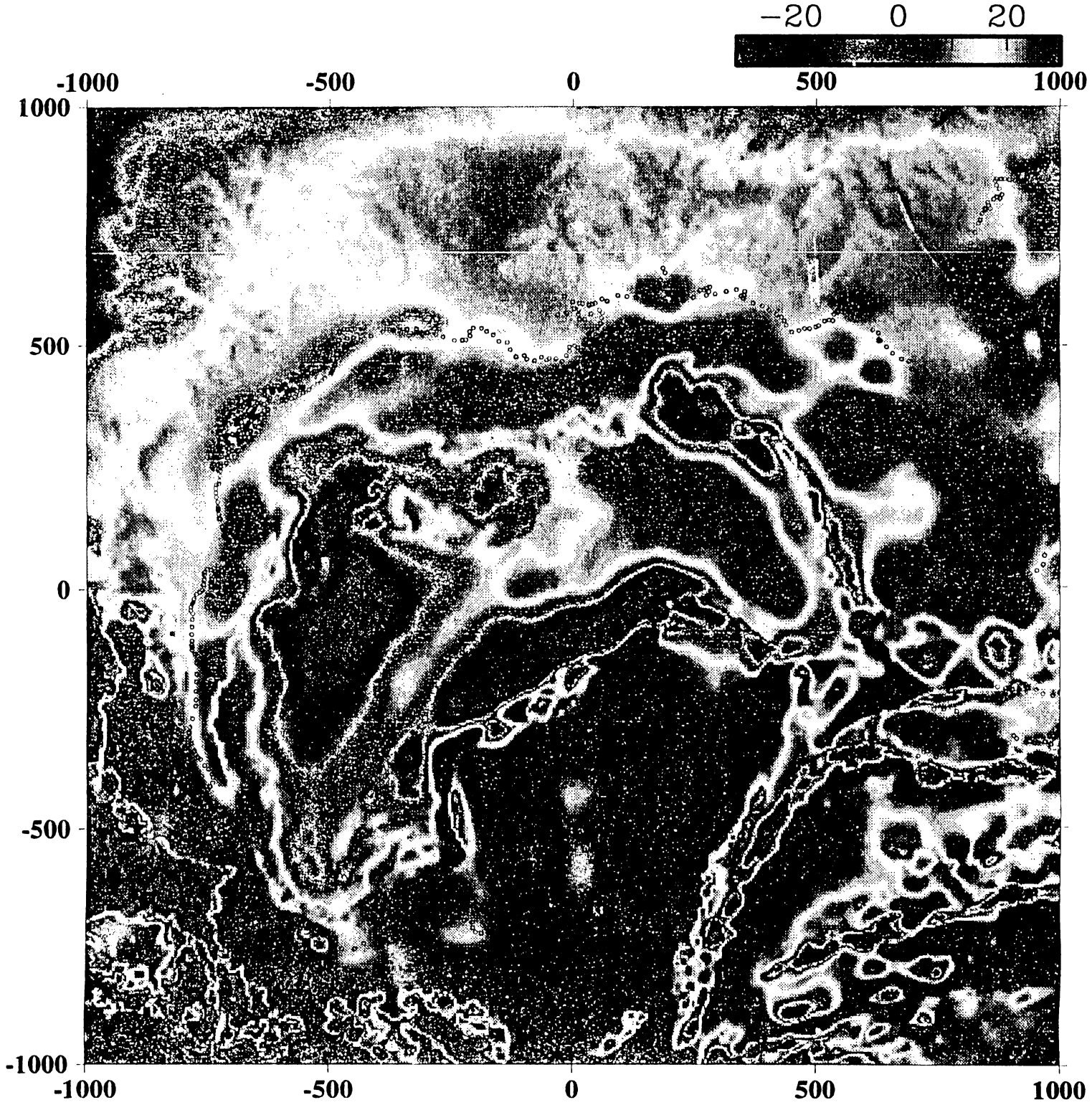
−20
0
20
-1000
-500
0
500
1000
1000
500
0
-500
-1000
-1000
-500
0
500
1000

Figure 6.9 Large scale crustal boundaries proposed by Sawyer et al, (1991) on the basis of geologic and geophysical constraints. The southern boundary of the region labelled Oceanic crust coincides with the arcuate high in the terrain corrected gravity (Figure 6.5) but the northern boundary extends far beyond the extent of the gravity high. The offset between the Mississippi Fan and Perdido Foldbelts near the center of the image coincides nearly exactly with a steep gradient in the isostatic residual gravity.

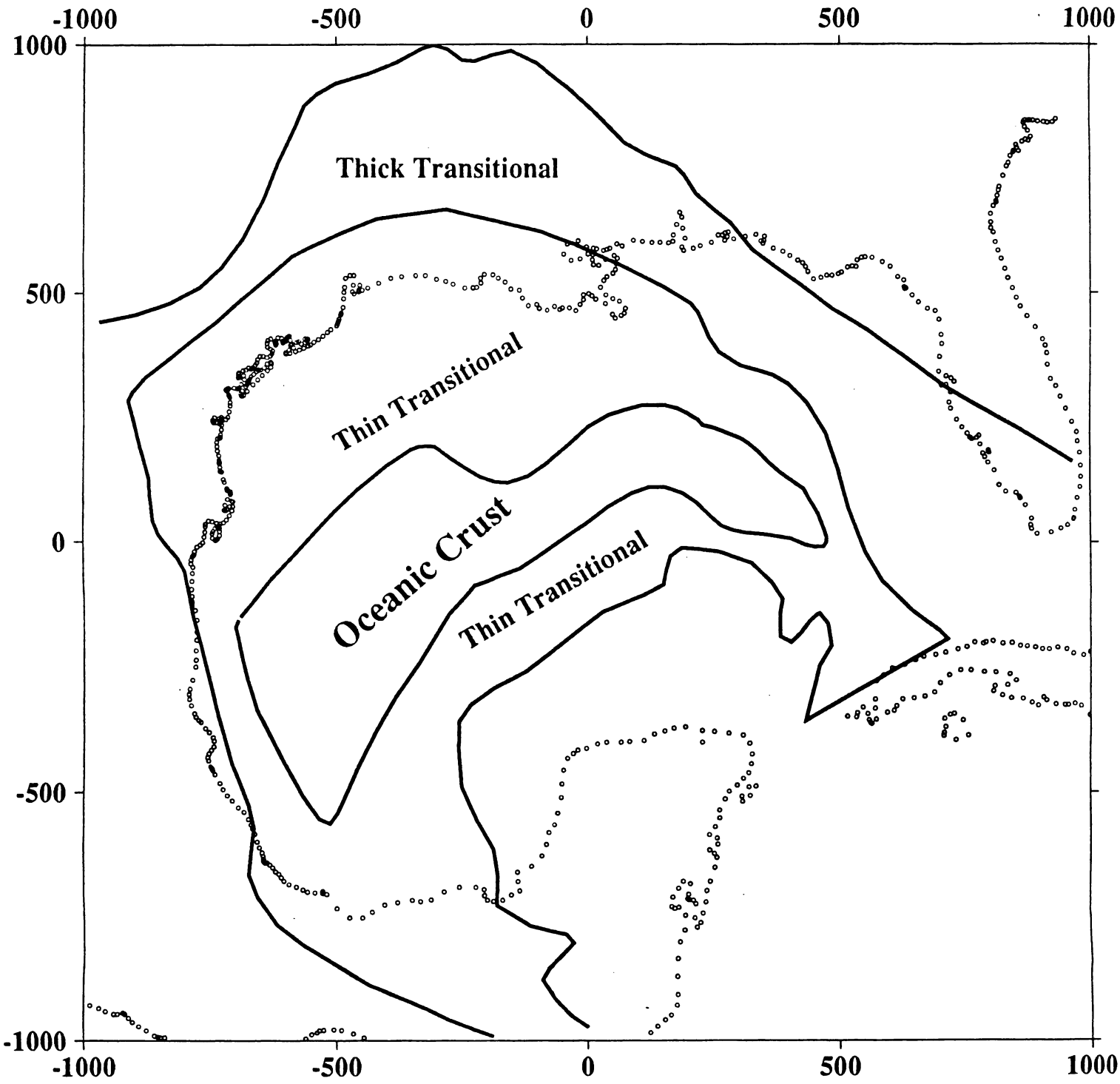
-1000
-500
0
500
1000
1000
500
0
-500
-1000
Thick Transitional
Thin Transitional
Oceanic Crust
Thin Transitional

References

Buffler, R. T., and D. S. Sawyer, Distribution of crust and early history, Gulf of Mexico basin, *Trans. Gulf Coast Assoc. Geol. Soc.*, 35, 333 - 344, 1985.

Buffler, R. T., F. J. Schaub, R. Huerta, A. K. Ibrahim, and J. S. Watkins, A model for the early evolution of the Gulf of Mexico basin, *Oceanol. Acta*, 4 (sp), 129 -136, 1981.

Buffler, R. T., J. S. Watkins, J. L. Worzel, and F. J. Shaub, Structure and early geologic history of the deep central Gulf of Mexico basin. in *Proceedings of a Symposium on the Origin of the Gulf of Mexico and the Early Opening of the Central North Atlantic*, edited by P. R., 3 - 16, L.S.U., Baton Rouge LA, 1980.

Dunbar, J., and D. S. Sawyer, Implications of continental crust extension for plate reconstruction: An example from the Gulf of Mexico, *Tectonics*, 6, 739 - 755, 1987.

Dym, H.P. and H. McKean, Fourier Series and Integrals, Academic Press, New York, 1972.

Ebeniro, J. O., Y. Nakamura, D. S. Sawyer, and W. P. J. O'Brien, Sedimentary and crustal structure of the northwestern Gulf of Mexico, *J. Geophys. Res.*, 93, 9075 - 9092, 1988.

Ebeniro, J. O., and W. P. O'Brien, Crustal structure of the South Florida bandk derived from Ocean Bottom Seismometer refraction profiles. *University of Texas Institute for Geophysics*, 32, 1984.

Ewing, J. I., J. L. Worzel, and M. Ewing, Sediments and oceanic structural history of the Gulf of Mexico, *J. Geophys. Res.*, 67, 2509 - 2527, 1962.

Hall, D. J., T. D. Cavanaugh, J. S. Watkins, and K. D. McMillen, The rotational origin of the Gulf of Mexico based on regional gravity data. in *Studies in Continental Margin Geology,* edited by J.S. Watkins and C.S. Drake, 115 - 126, A.A.P.G. Memoir, 1982.

Haxby, W. F., Gravity Field of the World's Oceans, National Geophysical Data Center, NOAA, Boulder, CO, 1987.

Haxby, W. F., G. D. Karner, J. L. Labrecque, and J. K. Weissel, Digital images of combined continental and oceanic datasets and their use in tectonic studies, *Eos - Trans. Amer. Geophys. Un.*, 64, 995 - 1004, 1983.

Ibrahim, A. K., J. Carye, G. Latham, and R. T. Buffler, Crustal structure in Gulf of Mexico from OBS refraction and multichannel reflection data, *Am. Assoc. Pet. Geol. Bull.*, 65, 1207 - 1229, 1981.

Ibrahim, A. K., and E. Uchipi, Continental oceanic crustal transition in the Gulf coast geosyncline. in *Studies in Continental Margin Geology*, edited by J.S. Watkins and C. Drake, A.A.P.G. Memoir, 1982.

Jachens, R.C., R.W. Simpson, R.J. Blakely and R.W. Saltus, Isostatic residual gravity and crustal geology of the United States, *Geological Society of America,* Memoir 172, 1989

Klitgord, K. D., Popenoe P. and Schouten H., Florida, A jurassic transform plate boundary, *J. Geophys. Res.*, 89, 7753 - 7772, 1984.

Klitgord, K. D., Hutchinson D. R., Schouten H., U.S. Atlantic continental margin; structural and tectonic framework. in *The Atlantic Continental Margin, U.S.: The Geology of North America,* edited by S.R.E.G. J.A., 19 - 55, Geological Society of America, 1988.

Krivoy, H. L., H. C. J. Eppert, and T. E. Pyle, Simple Bouguer map of the Gulf of Mexico and adjacent land areas, U.S. Geological Survey Geophysical Investigations Map GP-912, 1976.

Kruger, J. M., and G. R. Keller, Interpretation of crustal structure from regional gravity anomalies, Ouachita Mountains area and adjacent Gulf coastal plain, *Am. Assoc. Pet. Geol. Bull.*, 70, 667 - 689, 1986.

Parker, R.L., The rapid calculation of potential anomalies, *Geophys. J. R. Astron. Soc. 31*, 447-455, 1973.

Parker, R.L. A new method for terrain correction of large amplitude topography, Submitted to *Geophysics*, 1993

Rosenthal, D. B., Distribution of crust in the deep eastern Gulf of Mexico. M.A., The University of Texas at Austin, 1987.

Sawyer, D.S., R. T. Buffler and R. Pilger, The crust under the Gulf of Mexico basin, The Geology of North America, Vol J, A. Salvador Ed. 1991.

Small, C., and D. T. Sandwell, Comparison of Satellite and Shipboard Gravity Measurements in the Gulf of Mexico, *Geophysics*, In Press.

Smith, W. H. F., and P. Wessel, Gridding with continuous curvature splines in tension, *Geophysics*, 55, 293 - 305, 1990.

Society of Exploration Geophysicists, Gravity anomaly map of the United Satates (exdclusive of Alaska and Hawaii), *Society of Explotation Geophysicists*, Scale 1:2,500,000, 1982.

Van Wyckhouse, R. J., Synthetic Bathymetric Profiling System (SYNBAPS). Naval Oceanographic Office, TR-233, 1973.